

January 2013

# Analytical and Numerical Modeling of Assembly Procedures of Steel Fulcra of Bascule Bridges

Sriharsha Garapati

University of South Florida, sgarapat@mail.usf.edu

Follow this and additional works at: <http://scholarcommons.usf.edu/etd>

 Part of the [Materials Science and Engineering Commons](#), and the [Other Mechanical Engineering Commons](#)

## Scholar Commons Citation

Garapati, Sriharsha, "Analytical and Numerical Modeling of Assembly Procedures of Steel Fulcra of Bascule Bridges" (2013). *Graduate Theses and Dissertations*.

<http://scholarcommons.usf.edu/etd/4490>

This Dissertation is brought to you for free and open access by the Graduate School at Scholar Commons. It has been accepted for inclusion in Graduate Theses and Dissertations by an authorized administrator of Scholar Commons. For more information, please contact [scholarcommons@usf.edu](mailto:scholarcommons@usf.edu).

Analytical and Numerical Modeling of Assembly Procedures of Steel Fulcra of  
Bascule Bridges

by

Sri Harsha Garapati

A dissertation submitted in partial fulfillment  
of the requirements for the degree of  
Doctor of Philosophy  
Department of Mechanical Engineering  
College of Engineering  
University of South Florida

Co-Major Professor: Autar Kaw, Ph.D.  
Co-Major Professor: Rajiv Dubey, Ph.D.  
Kyle Reed, Ph.D.  
Ali Yalcin, Ph.D.  
Ramachandran Kandethody, Ph.D.

Date of Approval:  
January 24, 2013

Keywords: Draw Bridge, FEA, Design of Experiments, Thermal Stresses, Interference,  
Convection

Copyright © 2013, Sri Harsha Garapati

## **DEDICATION**

This thesis dedicated to my parents, who took care of me with all their love, and supported and believed in me. To my professor Dr. Autar Kaw, who guided, instructed and inspired me in the graduate school.

## ACKNOWLEDGMENTS

I wish to acknowledge the gracious support of many people for their contributions towards this work both directly and indirectly. First, I thank my co-major professor and advisor, Dr. Autar Kaw who patiently guided me through all phases of this work. He is a true role model, and the best professor I have ever seen. I am deeply indebted to him for financial support, and for the academic resources he provided. I would like to thank my co-major professor, Dr. Rajiv Dubey for the support he provided during my initial semesters into Ph.D. program. Without his support, I would have not made this far. The time and effort of Dr. Ali Yalcin, Dr. Kyle Reed and Dr. Ramachandran Kandethody as committee members is greatly appreciated.

I would like to thank my parents, Nagabhushanam and Padmavathi for their support, suggestions and invaluable encouragement that have always made me a better man and have indirectly prepared me to tackle challenges that I came across. Without my parents support and encouragement, I never would have made it this far.

Additionally, I would like to thank all my friends, especially from the research group, Luke Snyder (Structures Analyst-Lockheed Martin: Missiles and Fire Arms) and Dan Miller (Hatch Corporation), for having always motivated and accompanied me throughout the challenges of research. Without their help, this dissertation would have been much more difficult. I would also like to thank the services provided by Research Computing Department at USF, especially Brian Smith. I would like to thank Jeevan Gogineni (Verizon), Kalyan Tummala (Intel Corporation), Aravind Chowdary Meka

(Madhucon), Prabhu Kiran Kilaru (Advantage Metal Works), Swetha Pendyala (Gilbane Building Company), and Shilpa Pendyala (USF) for their friendship and support throughout my entire life.

## TABLE OF CONTENTS

LIST OF TABLES .....	iv
LIST OF FIGURES .....	vi
LIST OF EQUATIONS .....	ix
ABSTRACT.....	xiii
CHAPTER 1 INTRODUCTION .....	1
1.1 Introduction.....	1
1.2 Types of Bascule Bridge Designs .....	1
1.3 Fixed-Trunnion Bascule Bridge.....	2
1.4 Components: THG .....	3
1.4.1 Trunnion.....	4
1.4.2 Hub.....	4
1.4.3 Girder .....	6
1.5 Shrink-fitting.....	6
1.6 Assembly Procedure -1 (AP1) .....	8
1.7 Problems Encountered While Implementing AP1 .....	10
1.8 Literature Review on Failures While Shrink-Fitting .....	11
1.9 Literature THG Assembly.....	13
1.9.1 Assembly Procedure-2 (AP2) .....	14
1.9.2 Assembly Procedure-3 (AP3) .....	16
1.9.3 OMCCCL .....	19
1.9.4 OMSR .....	20
1.10 Present Study .....	22
CHAPTER 2 ANALYTICAL MODELING OF THE PROBLEM.....	26
2.1 Analytical Modeling .....	26
2.2 Thermal Problem .....	27
2.2.1 Steady State Solution .....	32
2.2.2 Transient Solution.....	33
2.2.2.1 Temporal Solution.....	34
2.2.2.2 Spatial Solution .....	35
2.3 Thermal Stresses .....	40
2.4 Interference Stress.....	50
2.4.1 Interference Stresses in Trunnion .....	51
2.4.2 Interference Stresses in Hub .....	52
2.4.3 Interference Stresses in the Assembly .....	53

2.5	Net or Total Stress State in the Assembly .....	53
2.6	Effect of Nonlinearity of the Material Properties on OMCCCL .....	54
2.7	Finite Element Method .....	56
2.7.1	Finite Element Verification Model .....	57
2.7.1.1	Geometry .....	57
2.7.1.2	Material Modeling .....	58
2.7.1.3	Meshing .....	59
2.7.1.4	Loading, Boundary Conditions and Solution .....	60
2.8	Comparison of Analytical Model and Finite Element Model .....	61
CHAPTER 3	ASSEMBLY PROCEDURE AP1 .....	66
3.1	Factors for DOE Study .....	66
3.1.1	Hub Radial Thickness to Hub Inner Diameter Ratio .....	66
3.1.2	Shrink-Fitting Method .....	67
3.1.3	TH Radial Interference .....	68
3.2	Finite Element Modeling of AP1 .....	69
3.2.1	Building Geometry .....	69
3.2.2	Material Properties .....	70
3.2.3	Meshing .....	71
3.2.4	Loading and Boundary Conditions .....	72
3.2.5	Solving .....	72
3.3	AP1 Results: OMSR .....	73
3.4	AP1 Results: OMCCCL .....	73
3.4.1	Percentage Contribution of the Factors .....	74
3.4.2	Sensitivity Analyses .....	74
3.4.2.1	Shrink-Fitting Method .....	74
3.4.2.2	Hub Radial Thickness to Hub Inner Diameter Ratio .....	78
3.4.2.3	Radial Interference .....	81
3.5	Conclusions of AP1 .....	82
CHAPTER 4	ASSEMBLY PROCEDURE AP2 .....	84
4.1	Factors for DOE Study .....	84
4.2	Finite Element Modeling of AP2 .....	84
4.2.1	Building Geometry .....	85
4.2.2	Material Properties .....	85
4.2.3	Meshing .....	85
4.2.4	Loading and Boundary Conditions .....	86
4.2.5	Solving .....	86
4.3	AP2 Results: OMSR .....	87
4.4	AP2 Results: OMCCCL .....	87
4.4.1	Percentage Contribution of the Factors .....	88
4.4.2	Sensitivity Analyses .....	88
4.4.2.1	Shrink-Fitting Method .....	89
4.4.2.2	Hub Radial Thickness to Hub Inner Diameter Ratio .....	91

4.5	Conclusions of AP2 .....	93
4.6	Comparison of AP1 and AP2.....	94
4.6.1	Percentage Contribution of Factors .....	95
4.6.2	Single-Step Shrink-Fitting Methods .....	95
4.6.3	Multi-Staged Shrink-Fitting Methods.....	100
4.7	Conclusions from Comparison of AP2 and AP1 .....	103
<b>CHAPTER 5 ASSEMBLY PROCEDURE AP3 .....</b>		
5.1	Assembly Procedure: AP3-A.....	107
5.2	Assembly Procedure: AP3-B .....	108
5.3	Finite Element Modeling .....	110
5.3.1	TH Assembly Modeling.....	110
5.3.2	Girder Heating Modeling.....	111
5.3.2.1	Temperature and Gravity Dependent Natural Convection Coefficients.....	113
5.4	Girder Hole Expansion Analysis .....	115
5.5	Results.....	118
5.5.1	AP3-A .....	118
5.5.2	AP3-B .....	119
5.5.3	Sensitivity Analysis for AP3-B.....	120
5.6	Comparison of AP3-B with AP1 .....	125
5.7	Conclusions from Comparing AP3-B and AP1 .....	128
<b>CHAPTER 6 RECOMMENDATIONS AND SUGGESTIONS.....</b>		
6.1	Conclusions and Recommendations to Assemblers and Bridge Designers.....	130
6.2	Broader Impact.....	132
6.3	Suggestions for Future Research .....	132
<b>REFERENCES .....</b>		
<b>APPENDICES .....</b>		
Appendix A: Hypothesis Testing for Thermal Diffusivity of Steel.....		143
Appendix B: Convergence Study.....		145
B.1	Convergence Study on Analytical Solution .....	146
B.2	Convergence Study on Finite Element Model .....	149
Appendix C: Radial Interference Calculations .....		153
C.1	Interference Calculations for TH.....	153
C.2	Interference Calculations for HG .....	153

## LIST OF TABLES

Table 1 Geometric parameters for the trunnion and hub for three Florida bridges .....	5
Table 2 Thermal material properties of cast steel .....	29
Table 3 Structural material properties of the steel for this study .....	41
Table 4 OMCCCL comparison for different material models .....	55
Table 5 FN3 fit radial interference values for three bridges used in this study .....	68
Table 6 All factors and levels for general factorial design .....	68
Table 7 Contribution of factor to OMCCCL in AP1 .....	74
Table 8 OMCCCL values for different shrink-fitting methods for three bridges for low interference value and $\alpha=0.1$ .....	78
Table 9 OMCCCL values for different alpha values for all the bridges for both high and low interference case for shrink-fitting method 1 .....	78
Table 10 OMCCCL values for different alpha values for all the bridges for both high and low interference case for shrink-fitting method 5 .....	80
Table 11 Contribution of factors to OMCCCL in AP2 .....	88
Table 12 OMCCCL values in AP2 for different shrink-fitting methods for three bridges for $\alpha=0.1$ .....	91
Table 13 OMCCCL values for different alpha values for all the bridges in AP2 with shrink-fitting method 1 .....	92
Table 14 OMCCCL values for different alpha values for all the bridges in AP2 for shrink-fitting method 5 .....	93
Table 15 Contribution of factors to OMCCCL in AP1 and AP2 .....	95
Table 16 OMCCCL values for different shrink-fitting methods in AP1 and AP2 for low interference case for $\alpha=0.1$ .....	101
Table 17 OMCCCL values for different shrink-fitting methods in AP1 and AP2 for high interference case for $\alpha=0.1$ .....	101

Table 18 OMCCCL values for different shrink-fitting methods in AP1 and AP2 for low interference case for $\alpha=0.4$ .....	102
Table 19 OMCCCL values for different shrink-fitting methods in AP1 and AP2 for high interference case for $\alpha=0.4$ .....	103
Table 20 Material properties of fiber glass and ceramic shell. ....	113
Table 21 Natural convection coefficients used in heating of the girder .....	115
Table 22 All factors and levels for general factorial design of AP3-B.....	120
Table 23 Contribution of factors to OMCCCL in AP3-B .....	121
Table 24 Percentage contribution of factors to OMCCCL in AP1 and AP3-B.....	125
Table 25 Percentage increase in OMCCCL values in AP3-B compared to single-stage and multi-stage shrink-fitting methods of AP1 (for low interference case) .....	128
Table A.1 Thermal diffusivity as a function of temperature .....	143
Table A.2 Regression statistics .....	144
Table A.3 ANOVA Table .....	144
Table A.4 Intercept and slope value .....	144
Table B.1 Convergence data at node-1 for analytical solution.....	146
Table B.2 Convergence data at node-2 for analytical solution.....	146
Table B.3 Convergence data at node-3 for analytical solution.....	147
Table B.4 Temperature and hoop stress data for finite element model .....	150
Table C.1 TH coefficient value C for FN3 fit.....	153
Table C.2 TH interference calculations for all the three bridges in this study .....	153
Table C.3 HG coefficient value C for FN3 fit .....	153
Table C.4 Table HG interference calculations for all the three bridges in this study .....	154

## LIST OF FIGURES

Figure 1 Double leaf bridge .....	3
Figure 2 THG assembly .....	3
Figure 3 Geometry of the trunnion .....	4
Figure 4 Geometry of the hub.....	5
Figure 5 Geometry of the 17th Street Causeway bascule bridge girder .....	6
Figure 6 AP1 steps of bascule bridge fulcrum.....	10
Figure 7 AP2 steps of bascule bridge fulcrum.....	15
Figure 8 AP3 steps of bascule bridge fulcrum.....	17
Figure 9 Yield strength and fracture toughness of cast steel as a function of temperature. ....	21
Figure 10 Geometry of trunnion-hub modeled as simple hollow cylinders .....	27
Figure 11 Radial mesh for analytical temperature distribution .....	39
Figure 12 Trunnion modeled as thick cylinder with external pressure.....	51
Figure 13 Hub modeled as thick cylinder with internal pressure .....	52
Figure 14 Critical crack lengths along the radial location of compound cylinder model.....	56
Figure 15 Geometry of the finite element verification model .....	57
Figure 16 Finite element mesh of two concentric cylinders .....	60
Figure 17 Comparison of ANSYS and analytical solution for temperature .....	62
Figure 18 Comparison of ANSYS and analytical solution for hoop stresses.....	63
Figure 19 Comparison of ANSYS and analytical solution for radial stresses .....	64
Figure 20 Trunnion-hub assembly .....	69

Figure 21 1/6 <sup>th</sup> geometry of TH assembly .....	70
Figure 22 1/6 <sup>th</sup> TH assembly meshed in ANSYS .....	71
Figure 23 Variation of OMCCL with shrink-fitting method for three bridges for low interference value and alpha=0.1 .....	77
Figure 24 OMCCL as a function of alpha for low interference and shrink-fitting method 1.....	79
Figure 25 OMCCL as a function of alpha for high interference and shrink-fitting method 1.....	79
Figure 26 OMCCL as a function of alpha for low interference and shrink-fitting method 5.....	80
Figure 27 OMCCL as a function of alpha for high interference and shrink-fitting method 5.....	81
Figure 28 OMCCL as a function of interference for shrink-fitting method 2 .....	82
Figure 29 AP2: Hub and trunnion geometry.....	85
Figure 30 AP2: Meshed models of hub and trunnion .....	86
Figure 31 Variation of OMCCL in AP2 with shrink-fitting method for three bridges for alpha=0.1 .....	90
Figure 32 OMCCL as a function of alpha in AP2 for shrink-fitting method 1 .....	92
Figure 33 OMCCL values for different alpha values for all the bridges in AP2 with shrink-fitting method 5 .....	93
Figure 34 Variation of OMCCL with alpha in AP1 and AP2 for low interference case.....	97
Figure 35 Variation of OMCCL with alpha in AP1 and AP2 for high interference case.....	99
Figure 36 Assembly procedure AP3-A.....	107
Figure 37 Assembly procedure AP3-B.....	109
Figure 38 Yield strength and fracture toughness of ASTM A36 as a function of temperature .....	109
Figure 39 Finite element model of the TH assembly.....	110
Figure 40 Finite element model of the girder .....	111

Figure 41 a) Heating coils and, b) Fiber glass insulation on the girder .....	112
Figure 42 Breaking the girder hole edge into two curves to find the centroid of the expanded hole .....	117
Figure 43 OMCCL as a function of alpha in AP3-B .....	123
Figure 44 OMCCL as a function of TH interference in AP3-B .....	124
Figure 45 Comparison of OMCCL for three assembly procedures as a function of alpha for three bridges and for low TH radial interference .....	127
Figure B.1 Convergence of temperature for analytical solution (data from Table B.2).....	149
Figure B.2 Hoop stress convergence for analytical solution (data from Table B.2) .....	149
Figure B.3 Convergence of temperature for finite element solution (data from Table B.4) .....	150
Figure B.4 Hoop stress convergence for finite element solution (data from Table B.4) .....	151

## LIST OF EQUATIONS

Equation 1 Stress intensity factor of a radial edge crack .....	19
Equation 2 Fracture toughness.....	19
Equation 3 Critical crack length .....	20
Equation 4 Overall Minimum Critical Crack Length (OMCCL) .....	20
Equation 5 Overall Minimum Stress Ratio (OMSR).....	20
Equation 6 Fourier's heat conduction equation in cylindrical coordinates.. ..	27
Equation 7 Infinitely long cylinder condition.....	27
Equation 8 Axisymmetric loading condition .....	28
Equation 9 Fourier's heat conduction equation for a infinitely long cylinder with axisymmetric loading.....	28
Equation 10 Constant temperature boundary condition at the inner surface of the trunnion .....	28
Equation 11 Constant temperature boundary condition at the outer surface of the hub.....	28
Equation 12 Initial temperature of the whole assembly.....	28
Equation 13 Regression model for thermal conductivity of steel.....	29
Equation 14 Transformation variable, theta.....	29
Equation 15 Differentiation of transformation variable with respect to temperature, T .....	30
Equation 16 Differentiation of temperature in terms of transformation variable theta.....	30
Equation 17 Transformed conduction equation in terms of transformation variable theta.....	31
Equation 18 Simplified form of transformed conduction equation .....	31

Equation 19 Transformed conduction equation solution is the sum of steady state and transient solutions.....	32
Equation 20 Transformed steady state equation .....	32
Equation 21 Steady state solution of the transformed conduction equation.....	33
Equation 22 Transformed transient conduction equation .....	33
Equation 23 Transient solution as product of temporal and spatial solutions .....	34
Equation 24 Transformed transient conduction equation in terms of spatial and temporal functions .....	34
Equation 25 Rearranged transformed transient conduction equation .....	34
Equation 26 Rearranged transformed conduction equal to a constant.....	34
Equation 27 Temporal differential equation .....	35
Equation 28 Solution to the temporal differential equation.....	35
Equation 29 Spatial differential equation .....	35
Equation 30 Solution to the spatial differential equation.....	35
Equation 31 Transient boundary condition at inner radius of the trunnion .....	36
Equation 32 Transient boundary condition at outer radius of the hub.....	36
Equation 33 Transient boundary conditions in matrix form.....	36
Equation 34 Equation to obtain eigenvalues of the problem .....	36
Equation 35 Transient solution .....	37
Equation 36 Simplified transient solution.....	37
Equation 37 Equation obtained by applying initial condition .....	37
Equation 38 Final solution of the transformed conduction equation.....	38
Equation 39 Radial stress in cylindrical coordinate system.....	40
Equation 40 Tangential or hoop stress in cylindrical coordinate system.....	40
Equation 41 Axial stress in cylindrical coordinate system .....	40
Equation 42 Radial strain in cylindrical coordinate system.....	41

Equation 43 Tangential strain in cylindrical coordinate system.....	41
Equation 44 Axial strain in cylindrical coordinate system .....	41
Equation 45 Radial stress as a function of radial displacement.....	42
Equation 46 Hoop stress as a function of radial displacement .....	42
Equation 47 Axial stress as a function of radial displacement .....	42
Equation 48 Elementary force balance equation .....	42
Equation 49 Radial displacement solution in cylindrical coordinates .....	43
Equation 50 Simplified displacement solution .....	44
Equation 51 Radial displacement in vector form.....	44
Equation 52 Simplified radial displacement in vector form .....	46
Equation 53 Final radial displacement equation.....	46
Equation 54 Differential of radial displacement in vector form .....	47
Equation 55 Radial displacement over radial location in vector form.....	48
Equation 56 Radial stress as a function of radial displacement in vector form.....	48
Equation 57 Hoop stress as a function of radial displacement in vector form .....	48
Equation 58 Axial stress as a function of radial displacement in vector form .....	48
Equation 59 Free surface boundary condition at the inner radius .....	49
Equation 60 Free surface boundary condition at the outer radius .....	49
Equation 61 Overall axial force is zero.....	49
Equation 62 Interface pressure developed between the two shrink-fit components.....	50
Equation 63 Radial interference stress in the assembly.....	53
Equation 64 Tangential interference stress in the assembly .....	53
Equation 65 Axial interference stress in the assembly .....	53
Equation 66 Net radial stress in the assembly .....	54
Equation 67 Net hoop stress in the assembly.....	54

Equation 68 Net axial stress in the assembly.....	54
Equation 69 Regression equation of thermal conductivity.....	58
Equation 70 Specific heat model formula in finite element model .....	58
Equation 71 Regression equation for thermal expansion coefficient .....	59
Equation 72 Hub radial thickness to hub inner diameter ratio.....	67
Equation 73 Rayleigh number formula.....	113
Equation 74 Nusselt number for surface facing upwards .....	114
Equation 75 Nusselt number for surface facing downwards .....	114
Equation 76 Nusselt number for surface facing sideways.....	115
Equation 77 Convection coefficient.....	115
Equation 78 Cartesian coordinates of the expanded hole .....	116
Equation 79 Cartesian coordinates of the centroid of an irregular area.....	116
Equation B.1 Convergence equation.....	145
Equation C.1 Interference limit formula.....	153

## ABSTRACT

To model shrink-fitting in metal components, an analytical model for two long compound cylinders with temperature dependent material properties and interference between them is developed for calculating transient temperatures and stresses. A finite element model is developed for the same geometry which incorporated the temperature dependent material properties. A convergence study is performed on the finite element and analytical model. The finite element model is validated by comparing the approximations of finite element model with the analytical solution.

In an assembly procedure of fulcrums for bascule bridges, called AP1, the trunnion is shrink-fitted into a hub, followed by shrink fitting the trunnion-hub assembly into the girder of the bridge. In another assembly procedure called AP2, the hub is shrink-fitted into the girder, followed by shrink-fitting the trunnion in the hub-girder assembly. A formal design of experiments (DOE) study is conducted on both AP1 and AP2 using the finite element model to find the influence of geometrical parameters such as radial thickness of the hub, radial interference, and various shrink-fitting methods on the design parameter of overall minimum critical crack length (OMCCL) - a measure of likelihood of failure by cracking. Using the results of DOE study conducted on both the assembly procedures, AP1 and AP2 are quantitatively compared for the likelihood of fracture during assembly.

For single-staged shrink-fitting methods, for high and low hub radial thickness to hub inner diameter ratio, assembly procedure AP1 and AP2 are recommended, respectively. For fulcras with low hub radial thickness to hub inner diameter ratio and where staged shrink-fitting methods are used, for AP2, cooling the trunnion in dry-ice/alcohol and heating the girder, and for AP1, cooling the trunnion-hub assembly in dry-ice/alcohol followed by immersion in liquid nitrogen is recommended. For fulcras with high hub radial thickness to hub inner diameter ratio and where staged shrink-fitting methods are used, cooling the components in dry-ice/alcohol and heating the girder is recommended for both AP1 and AP2.

Due to the limitations of AP2, assembly procedures by heating the girder with heating coils instead of dipping an already stressed trunnion-hub assembly in liquid nitrogen are studied for decreasing the likelihood of failure by cracking and yielding. In an assembly procedure called AP3-A, only the girder is heated to shrink-fit the trunnion-hub assembly in the girder. This assembly procedure AP3-A is found to be infeasible because the girder fails by yielding if heating is expected to be completed in a reasonable amount of time. An alternative assembly procedure called AP3-B is suggested for shrink-fitting where the heating of the girder is combined with cooling the trunnion-hub assembly in dry-ice/alcohol mixture. This assembly procedure AP3-B is found to be feasible. A complete DOE study is conducted on AP3-B to find the influence of parameters like hub radial thickness and radial interference at trunnion-hub interface on the design parameter of overall minimum critical crack length. The design parameter, OMCCCL values during the assembly procedure AP3-B are quantitatively compared with the widely used assembly procedures (AP1 single-stage shrink-fitting and AP1 multi-

staged shrink fitting). The results of this work suggest that increasing the hub radial thickness decreases the likelihood of fracture significantly. For hubs with large radial thickness, heating the girder combined with cooling the trunnion-hub in dry-ice/alcohol mixture (AP3-B) is recommended but for hubs with low radial thickness, multistage cooling of the trunnion-hub assembly in dry-ice/alcohol mixture followed by dipping in liquid nitrogen (AP1- multistage cooling) is recommended.

## CHAPTER 1 INTRODUCTION

### 1.1 Introduction

The bascule bridges (Figure 1), sometimes also called draw-bridges, have been widely used in many waterways around the world. By lifting one section (leaf) or both sections of its span, bascule bridges facilitate road transportation and also marine transportation for ships that could not otherwise clear the bridge height. The leaf of the bascule bridge pivots on large bearings. These bearings are fit onto a large axle. This axle assembly is commonly referred as Trunnion-Hub-Girder (THG) assembly (Figure 2). The THG assembly serves as a fulcrum as the leaf is lifted.

The most common and widely implemented method of performing THG assembly is by shrink-fitting [1-9]. Most of us do not realize the mechanical failures that might occur while shrink-fitting large steel structures. The focus of this dissertation is to explain the types of mechanical failures that occurred in the THG components during assembly, reasons for these failures, and to find alternative assembly procedures which would be less prone to failure.

### 1.2 Types of Bascule Bridge Designs

The two most commonly used designs of the bascule bridge are Scherzer rolling lift and the fixed-trunnion [10]. Fixed-trunnion bascule bridge design is the most commonly used design because they can open and close quickly, and require relatively

small amount of energy to activate when compared to Scherzer rolling bridge design [9]. Fixed-basculer bridge design is also often less expensive when compared to the Scherzer rolling bridge design [9]. This study involves assembly analysis of fixed-trunnion basculer bridge design only.

### **1.3 Fixed-Trunnion Basculer Bridge**

There are two types of fixed trunnion basculer bridge designs: 1) Double-leaf basculer bridge, and 2) Single-leaf basculer bridge. Double leaf basculer bridges are fairly common, the most prominent example being the Tower Bridge (Figure 1 (a)) built in 1886. Inside the USA, prominent double-leaf basculer bridges are found in downtown Chicago (Figure 1 (b)) built in the early 20<sup>th</sup> century. Single leaf basculer bridges are also fairly common. Examples in Florida include the 17<sup>th</sup> street Causeway basculer bridge, the Hallandale basculer bridge, and the Christa McAuliffe basculer bridge.

In the fixed-trunnion basculer bridge design, THG assembly serves as critical component as it not only supports the weight of the leaf of the bridge but also the counterweight of the assembly that helps in lifting its span [9]. If the THG assembly is not performed properly, the safety of the bridge is compromised. The THG assembly is performed by shrink-fitting to create interference between the components [1-4, 6-9]. The interference gives additional strength between the components due to the interference stress which is developed due to the expansion of the inner component on to the outer component. This is the main reason for incorporating interference during the design stage of the fulcrum components.



a



b

Figure 1 Double leaf bridge



Figure 2 THG assembly

#### 1.4 Components: THG

The THG consists of three main components (Figure 2).

1. Trunnion (innermost component).
2. Hub (middle component)

### 3. Girder of the bridge (outermost component).

#### 1.4.1 Trunnion

The geometry of the trunnion is a hollow cylinder, and it acts like a pin (Figure 3).

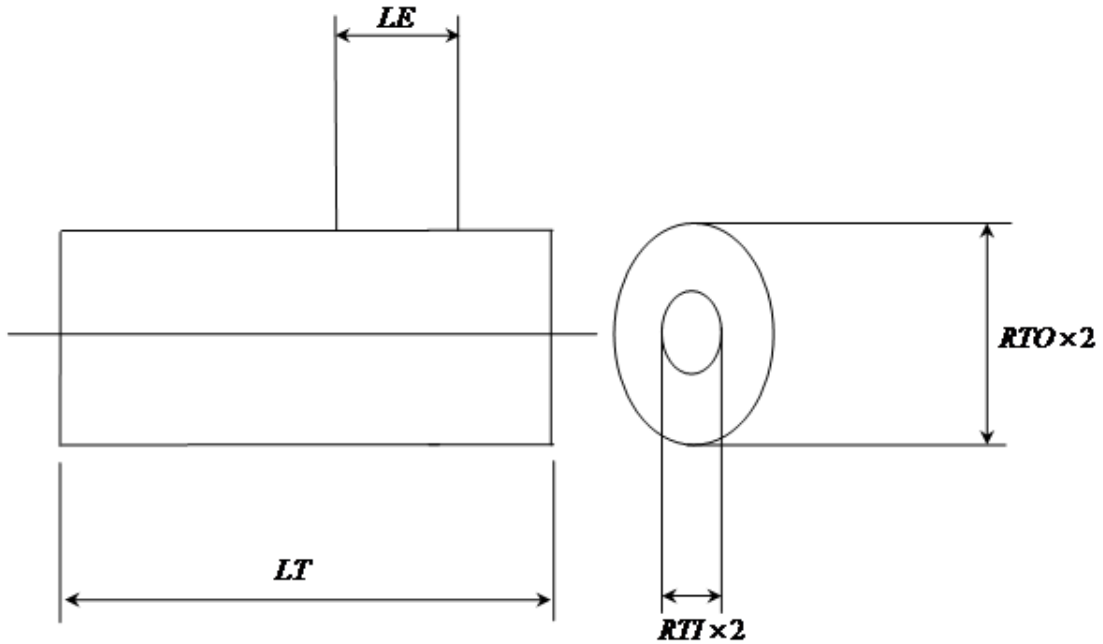


Figure 3 Geometry of the trunnion

#### 1.4.2 Hub

The hub is the component in the THG assembly into which the trunnion is shrink-fitted. The geometry of the hub plays a very pivotal role while performing the assembly. For hubs that contain larger flanges, the distribution of the thermal gradients and stress can be quite different compared to hubs with smaller flanges. The length of the flange, and the gussets, and the thickness of the hub can very well affect the value of the critical stress and the location of the critical stress in the geometry. The geometry of the hub of a typical bascule bridge fulcrum is shown in (Figure 4).

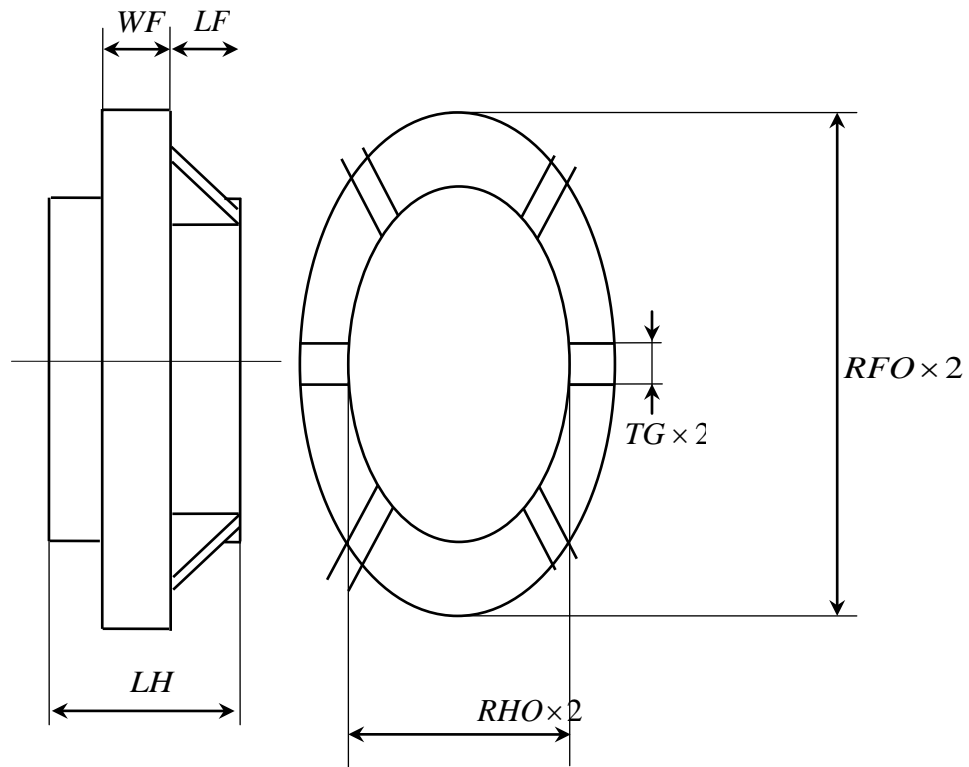


Figure 4 Geometry of the hub

Table 1 gives the dimensions of the trunnion and hub for three Florida bridges that are used in this study.

Table 1 Geometric parameters for the trunnion and hub for three Florida bridges

Parameter	Value (in) for the following		
	17th Street Causeway Bascule Bridge	Christa McAuliffe Bascule Bridge	Hallandale Bascule Bridge
Extension of the trunnion on the gusset side, LE	6.00	18.5	26.0
Distance to the hub flange, LF	4.25	4.25	7.00
Total length of the hub, LH	11.0	16.0	28.0
Total length of the trunnion, LT	23.0	53.5	80.0
Hub outer radius, RHO	8.88	16.0	17.50

**Table 1 (Continued)**

Hub flange outer radius, RFO	13.2	27.0	30.0
Trunnion inner radius, RTI	1.19	1.00	1.50
Trunnion outer radius, RTO	6.47	9.00	13.0
Gusset thickness, TG	1.25	1.50	2.00
Width of the flange, WF	1.25	1.75	3.00

### 1.4.3 Girder

The girder of the bridge is the largest component of the THG assembly. It is the largest structural component of the bridge. Figure 5 shows the girder of the 17<sup>th</sup> street Causeway bascule bridge.

Girder serves as the main body (structural strength) of the bascule bridge.

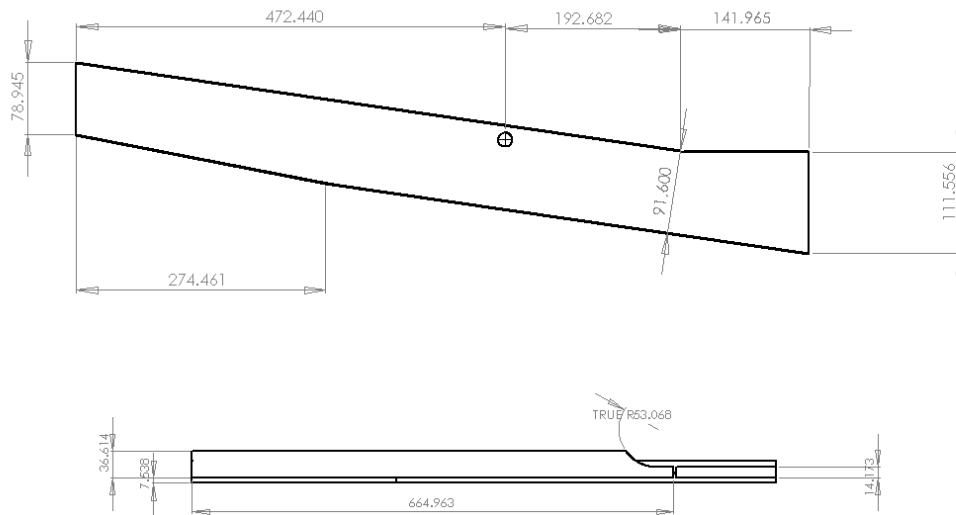


**Figure 5 Geometry of the 17th Street Causeway bascule bridge girder**

### 1.5 Shrink-fitting

Shrink-fitting is a technique in which parts of an assembly are heated or cooled to take advantage of thermal expansion to make a joint [11]. One of the oldest known

examples of shrink-fitting is heating the iron strip to fit around the cart wheel. An iron strip of which the diameter is less than the diameter of the wheel would be heated, and due to thermal expansion of the iron, the diameter of the strip increased and reached a value slightly greater than the diameter of the wheel. The strip would then be fitted around the wheel and allowed to cool down. After cooling, the iron strip would contract and bind tightly to the cart wheel.

In the 21st century, a common shrink-fitting method used in the industry is based on induction heating [12]. In this method, the metal components are pre-heated between 150°C and 300°C, thereby facilitating insertion of the mating component. Usually in induction heating, larger components are heated so that the smaller mating components can be inserted into them. But, cooling the smaller component is found to be very fast, economical and energy efficient. Smaller components are usually cooled by dipping in a cold medium. The most commonly used cold medium on metal components is liquid nitrogen as it has no permanent effect on ferrous or non-ferrous metals except for certain austenitic irons.

In many modern day applications, shrink-fitting procedure is performed when a gear or bush or similar component is to be mounted on to a shaft or pin like component. The same assembly could also be performed by the application of 'keys'. But assembling the component by the use of keys requires providing 'key ways' in both the mating components. The key ways are the stress concentrators and decrease the overall load/torque the assembly could withstand. In shrink-fitting, the joint or mate in the assembly is seamless and the shrink-fit process itself adds additional strength to the assembly. This is the main reason that makes shrink-fitting a favorable assembly

procedure for many mechanical designers. Shrink-fitting has many applications in the fields of automotive, medical device, construction, and manufacturing. Few of the examples are listed below [13].

Shrink-fitting auto turbo charger impeller blades onto an aluminum shaft

Shrink-fitting aluminum pulley to insert inner bearing

Shrink-fitting an assembled wrist pin into a connecting rod

Shrink-fitting a cast iron rocker arm assemblies

Shrink-fit a motor shaft and roller

Shrink-fitting a camshaft gear

Shrink-fitting a fuel pump housing and inserts

Shrink-fitting a gear securely on a shaft (automotive)

Heating a stainless steel sleeve for industrial washers

Shrink-fitting a steel mud pump liner

Shrink-fit a steel gear onto a steel gear motor shaft

Shrink-fitting a carbide ring into a valve seat

Shrink-Fitting a graphite ring insert (medical device)

Manufacturing large caliber guns of battle ships and cruisers

## 1.6 Assembly Procedure -1 (AP1)

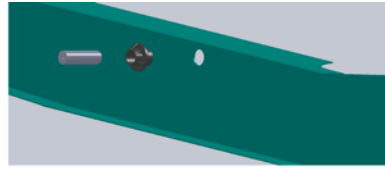
Assembly procedure, hereby, called AP1 is the most common and widely implemented assembly procedure for fulcrums of bascule bridges. It is characterized by the following four steps [2-4, 7, 9] (Figure 6).

1. Step 1: The steel (ASTM A668) trunnion is shrunk by immersing in a cold bath like liquid nitrogen ( $-321^{\circ}F$ ). The trunnion is left in the cold bath

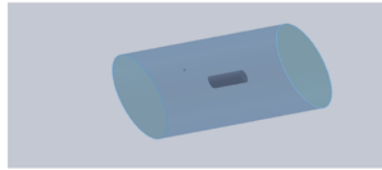
till it reaches a steady state temperature; typically the steady temperature would be the temperature of the cooling medium in the bath.

2. Step 2: The shrunk trunnion is inserted into the steel (ASTM A148) hub. The cold trunnion ( $-321^{\circ}F$ ) and the warm (room temperature) hub are left in the ambient air till both the trunnion and the hub reach the room temperature. This creates an interference fit assembly (TH assembly) between the trunnion and the hub (trunnion-hub interface) due to the expansion of the trunnion in the hub.
3. Step 3: The entire TH assembly is then immersed in a cold bath, such as liquid nitrogen ( $-321^{\circ}F$ ) for shrinking. The TH assembly is left in the bath till it reaches steady state temperature.
4. Step 4: The cold (shrunk) TH assembly is inserted into the hole of the girder of the bridge which is at room temperature. The entire assembly (THG) is left in ambient air till it reaches the room temperature. This now creates an interference fit between the TH assembly and the girder (hub-girder interface).

The manufacturer of the trunnion and the hub components performs the first two steps of AP1 in the factory and ships the TH assembly to the contractor. The contractor performs steps 3 and 4 at the bridge construction site. This assembly procedure (AP1) implemented in Florida resulted in a few failures such as cracking of the hub while performing the assembly (step 3) at the construction site [3]. The following sections details about the previous failures observed on the field, reasons for these failures, and previous studies conducted on the THG assembly procedures.



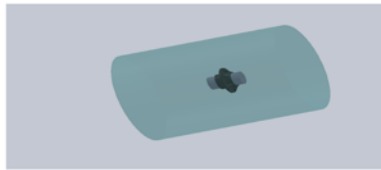
**THG Components**



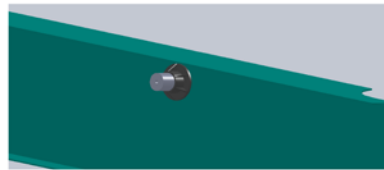
**Step 1: Cooling Trunnion in cold bath**



**Step 2: Shrunk trunnion in the hub**



**Step 3: Cooling TH assembly in cold bath**



**Step 4: Shrunk TH into the girder**

**Figure 6 AP1 steps of bascule bridge fulcrum**

## **1.7 Problems Encountered While Implementing AP1**

The Florida Department of Transportation (FDOT) witnessed failure of THG assembly by adopting AP1 on more than one occasion. In 1995, the construction of Christa McAuliffe bridge was halted because the main hub component cracked while cooling the TH assembly in a liquid nitrogen bath (step 3 of AP1) [4]. On another

occasion, during the construction of the Venetian Causeway bascule bridge, the trunnion got stuck in the hub before it could be completely go inside the hub (step 2 of AP1) [4].

These two incidents cost FDOT hundreds of thousands of dollars in new capital, labor and delay costs. To avoid these failures in future projects, FDOT started a research study in collaboration with University of South Florida (USF) [3]. To completely understand the reasons for these failures, a literature search was performed on failure of materials subjected to thermal shock, cooling and shrink-fitting.

### **1.8 Literature Review on Failures While Shrink-Fitting**

To study the effect of cryogenic temperatures on metals such as steel, Greenberg and Clark [14] studied the fracture and failure mechanisms in ASTM A-216-66 grade steel plate cooled in liquid nitrogen while subjected to different loading conditions. This is the first study to characterize failure mechanisms of thick steel castings subjected to cryogenic temperatures. This study [14] also gave the calculation of the maximum allowable crack length (critical crack length) that can be observed in the material without failure. Also, this study [14] made important observations on variation of fracture toughness and yield strength of steel with temperature. Later in 1983, Nied and Erdogan [15] used the superposition method to analyze the transient stresses in a circumferentially cracked hollow cylinder. In 1985, Delale and Kolluri [16] conducted a study on fracture of thick walled cylinders subjected to transient thermal stresses. Their study included the calculation of stress intensity factor in cylinders and edge plates. Noda and Sumi [17] in 1985 used finite difference method to obtain a transient solution for the stress intensity factor in cylinders and plates. Noda's studies [17-24] are relevant to shrink-fitting failures as stress intensity factor relates to fracture of materials subjected to transient thermal

loading conditions. Olivera and Wu [25] studied the stress intensity factor and fracture toughness of hollow cylinders subjected to thermal stress gradient with both internal and external cracks.

It is found from the above studies that the properties of the material (fracture toughness, yield strength, thermal conductivity, density, specific heat, etc) and the convection coefficients change when a metal component is immersed (dipped) in a subzero temperature liquid. Many research studies have been conducted to model the thermal stress problem for a hollow cylinder numerically and analytically by taking into account either variation of material properties with temperature [26-36], or variation of boundary conditions (with time or temperature) [35, 37, 38], or thermal load (with time) [39-44]. Analytical solution studies conducted on thermal stress of anisotropic or functionally graded hollow cylinders [28, 31, 32, 39, 45-52] could also be applied to this problem because the temperature gradient causes the spatial variation of material properties and hence could be modeled as a functionally graded material. We found no analytical study conducted, that incorporated all the complexities (variation of material properties with temperature and presence of interference stress or pre-stressed component) involved when a metal component dipped in liquids at subzero temperatures. All the studies mentioned till now in this section studied either the failure mechanisms or the thermal stresses state in a component (not an assembly) when subjected to transient thermal loading conditions.

Chen and Kuo [53] using finite element method studied the problem of cooling of an inserted component (assembly) by immersion in a subzero cooling medium. They found tensile hoop stress at the inner diameter of the outer cylinder leading to opening of

the cracks (crack propagation). Other researchers have studied this problem [2-5, 8, 9, 32, 44, 54-56] including a numerical study [5] conducted in University of South Florida (USF) using finite difference method which incorporated all the complexities of the problem, that is, variation of material properties with temperature, variation of boundary conditions (temperature dependent), and radial interference. All these studies gave valuable knowledge that during the shrink-fitting process, thermal stresses are developed due to the thermal shock of the cooling process. Interference stresses are developed due to the shrink-fitting as the assembly warms up to steady-state room temperature. The combined effect of these thermal and interference stresses and the lowering of fracture toughness of the steel with decrease in temperature contribute to failure of the steel by cracking.

### **1.9 Literature THG Assembly**

In 2000, Denninger [6] developed a code which calculated torque on the THG components and also analyzed the stress state of the THG assembly for various fits and bolt patterns used in construction. However, this work could not analyze the transient stresses developed in the assembly during cooling. Later, Besterfield et al. [2] developed a finite element model in ANSYS [57] to study the transient and steady state stresses occurring during the assembly. Their work [2] concluded that in AP1, when the hoop stresses were high and temperature was low, the smallest critical length was observed. In that work [2], Besterfield et al. made useful observations that the failure in AP1 is due to the low value of the critical crack length observed in the hub component during step 3 of AP1, that is, cooling of the TH assembly in liquid nitrogen. Their explanation of this failure is due to the combination of thermal stresses induced during cooling, the tensile

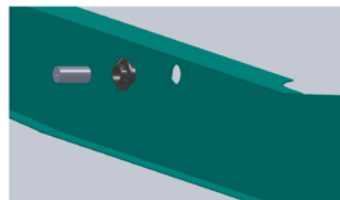
hoop stresses in the hub due to TH interference, and the lowering of fracture toughness at cryogenic temperatures caused the cracks to propagate (open up). Their (Besterfield et al. [2]) conclusions explained why the hub cracked during the construction of Christa McAuliffe bridge fulcrum in 1995.

### 1.9.1 Assembly Procedure-2 (AP2)

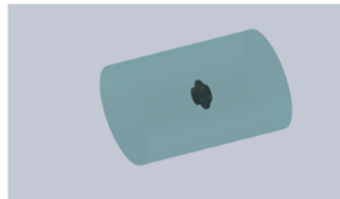
To avoid the exposure of components under tensile stress to low (cryogenic) temperatures, a different assembly procedure, AP2 was proposed [2]. AP2 is an assembly procedure adopted mostly in the northern states of United States. However, it is not as widely implemented as AP1 due to some limitations which is explained in Section 1.10 of this dissertation. AP2 is characterized by the following four steps (Figure 7).

1. Step 1: The steel (ASTM A148) hub is shrunk by immersing in cold bath like liquid nitrogen ( $-321^{\circ}F$ ). The hub is left in the cold bath till it reaches a steady state temperature; typically the steady temperature would be the temperature of the cooling medium in the bath.
2. Step 2: The shrunk hub is inserted into the steel girder. The cold hub ( $-321^{\circ}F$ ) and the warm (room temperature) girder are left in the ambient air till both the hub and the girder reach the room temperature. This creates an interference fit assembly (HG assembly) between the hub and the girder (hub-girder interface) due to the expansion of the hub in the girder.
3. Step 3: The trunnion is immersed in a cold bath, such as liquid nitrogen ( $-321^{\circ}F$ ) for shrinking. The trunnion is left in the bath till it reaches the steady state temperature.

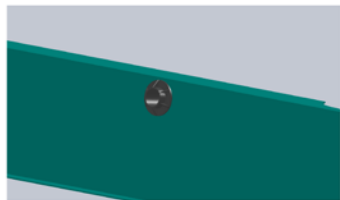
4. Step 4: The cold (shrunk) trunnion is inserted into the HG assembly which is at room temperature. The entire assembly (THG) is left in ambient air till it reaches the room temperature. This creates an interference fit between the trunnion and the HG assembly (trunnion-hub interface).



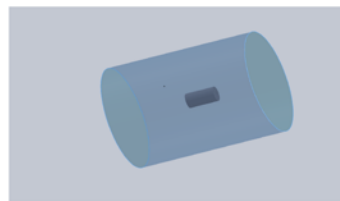
**THG Components**



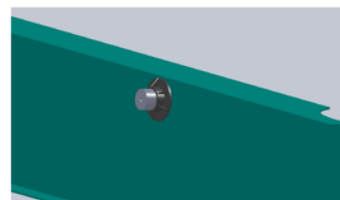
**Step 1: Hub in cold bath**



**Step 2: Shrunk hub into the girder**



**Step 3: Trunnion in cold bath**



**Step 4: THG assembly**

**Figure 7 AP2 steps of bascule bridge fulcrum**

The assembly procedure AP2 removes the possibility of an assembled part being subjected to cryogenic temperatures. Besterfield et al. [2] work concluded that AP2

lowered the likelihood of failure by increasing the critical crack lengths. To confirm their previous work [2], Besterfield et al. [4] conducted a full-scale testing of the THG assembly. Their testing confirmed the stresses predicted by the FEM model in their previous work [2] and the conclusion that AP2 is a safer assembly procedure than AP1.

### **1.9.2 Assembly Procedure-3 (AP3)**

In 2004, Berlin [1] proposed a assembly procedure called AP3 in which rather than cooling the TH assembly (step 3 of AP1), the girder is heated. His work proposed to heat the girder with heating coils to create enough expansion of the girder hole so that hub component could be inserted into the girder. Berlin's work [1] laid the foundation for future researchers to study/explore the possibilities of implementing heating procedures rather than cooling. However, his work did not include a complete analysis of the expansion of the girder hole.

AP3 is also an assembly procedure implemented by bridge contractors in USA. However, it is not as widely implemented as AP1 and AP2. In the literature, we only found an assembly procedure very similar to AP3 being used in the construction of Pamunkey River bridge in West Point, Virginia [58].

AP3 is characterized by the following steps [1] (Figure 8).

1. Step 1: The girder is heated by placing induction coils to create sufficient expansion of the girder hole for the hub to go inside the girder.
2. Step 2: The steel (ASTM A148) hub that is now at room temperature is inserted into the warm steel girder. The hub-girder assembly is left in the ambient air till both the hub and the girder reach the room temperature.

This creates an interference fit assembly (HG assembly) between the girder and the hub (hub-girder interface).

3. Step 3: The trunnion is shrunk in cooling medium such as liquid nitrogen.
4. Step 4: The trunnion is then inserted into the HG assembly is allowed to reheat to the ambient temperature to create an interference fit between the trunnion and the hub (trunnion-hub interface).



Figure 8 AP3 steps of bascule bridge fulcrum

Assembly procedure AP3 is not usually preferred by many bridge contractors because the heating of the girder hole is a complex, time consuming, and relatively

expensive process when compared with assembly procedures like AP1 and AP2 which involve only cooling mechanisms like dipping in liquid nitrogen. These limitations of heating the girder caused the demand to research/explore for better/safer cooling mechanisms. To reduce the large thermal stresses in AP1, Collier et al. [5] replaced the single staged shrink-fitting with multi-staged shrink-fitting. This work [5] studied the temperature dependence of material properties in a long compounded composite cylinder using an axisymmetric finite difference method and also included studying four staged shrink-fitting methods involving only cooling. This work concluded that performing staged (stepped) cooling, that is, cooling in refrigerated air ( $-32^{\circ}F$ ) and then cooling in liquid nitrogen ( $-320^{\circ}F$ ) decreased the possibility of failure by 50% when compared to cooling the material in liquid nitrogen alone [5]. Collier et al. [5] study also reported that staged cooling method of cooling in refrigerated air and then in liquid nitrogen gave higher critical crack lengths than the staged cooling method of cooling in dry-ice/alcohol mixture first and then in liquid nitrogen.

Nguyen et al. [8] developed a finite element model in ANSYS [57] with actual TH geometry and conducted a full design of experiments (DOE) [59] study on three Florida bridges namely, 17<sup>th</sup> street Causeway bascule bridge (small), Christa McAuliffe bridge (medium), and Hallandale bridge (large). Their DOE [8] study was conducted by taking shrink-fitting methods (four different shrink-fitting methods [5] involving only cooling), interference (FN2 interference - high and low values), and American Association of State Highway and Transportation (AASHTO)  $\alpha$  ratio (hub radial thickness/hub inner diameter-three values) as factors. The output parameters for this study were: Overall Minimum Critical Crack Length (OMCCL) - a measure of likelihood

of failure by cracking, and Overall Minimum Stress Ratio (OMSR) - a measure of failure by yielding.

### 1.9.3 OMCCL

OMCCL is the minimum value of critical crack lengths (CCL) found throughout the assembly procedure.

Critical crack length (CCL) is the measure of the largest crack length that could be present in the material before failing by fracture for an applied tensile stress. That is, if the material has cracks larger than the CCL value, it would fail by fracture.

Analytically, the stress intensity factor  $K_1$ , of a radial edge crack of a thick cylinder is given by

$$K_1 = f_e \sigma_\theta \sqrt{\pi a}$$

**Equation 1 Stress intensity factor of a radial edge crack**

where,  $f_e$  is the edge effect factor,  $\sigma_\theta$  is the tensile hoop stress applied, and  $a$  is the crack length.

The crack length  $a$  for which the stress intensity factor  $K_1$  becomes equal to the fracture toughness  $K_{IC}(T)$  of a material is called the critical crack length (CCL). Therefore, if  $K_1 = K_{IC}(T)$ , then  $a = CCL$ . Substituting  $a = CCL$  and  $K_1 = K_{IC}$  in Equation 1 we get

$$K_{IC} = f_e \sigma_\theta \sqrt{\pi(CCL)}$$

**Equation 2 Fracture toughness**

Rewriting Equation 2 gives

$$CCL = \frac{K_{IC}^2(T)}{f_e^2 \pi \sigma_\theta^2}$$

**Equation 3 Critical crack length**

Therefore, as OMCCCL is the minimum value of the critical crack length found throughout the assembly procedure, it is given by

$$OMCCCL = \min\left(\frac{K_{IC}^2(T)}{f_e^2 \pi \sigma_\theta^2}\right)$$

**Equation 4 Overall Minimum Critical Crack Length (OMCCCL) [60]**

Fracture toughness is represented as  $K_{IC}(T)$  rather than the usual notation followed in many fracture mechanics textbooks [61-63] as  $K_{IC}$  because fracture toughness of a material changes with temperature. Fracture toughness of metals such as steel decreases with decrease in temperature [14] (Figure 9).

#### 1.9.4 OMSR

Stress ratio is the ratio of yield strength of the material to the Von-Mises [61-64] stress,  $\sigma_e$ . OMSR is the minimum value of the stress ratio found throughout the assembly process. Therefore, OMSR is given by

$$OMSR = \min\left(\frac{Y_s(T)}{\sigma_e}\right)$$

**Equation 5 Overall Minimum Stress Ratio (OMSR)**

If the Von-Mises [61-64] stress is greater than the yield strength, then the material is considered to have failed by yielding. So, if the stress ratio is found to be less than one, then the component will fail by yielding.

Similarly like fracture toughness, yield strength is also a function of temperature and for metals such as steel increases with the decrease in temperature [14] (Figure 9).

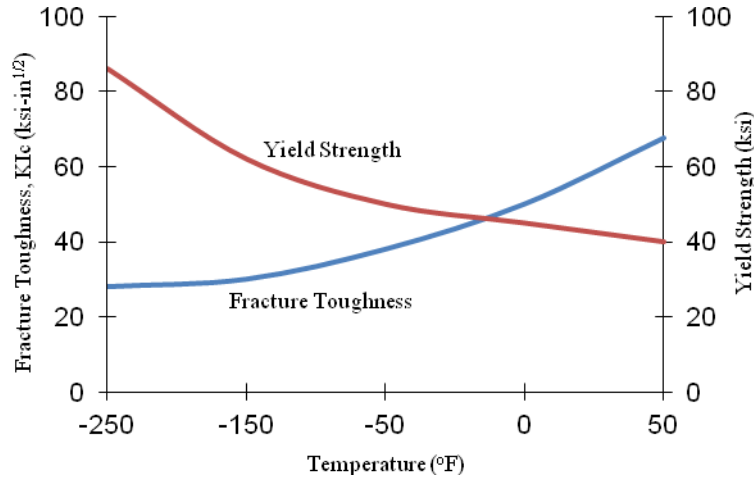


**Figure 9 Yield strength and fracture toughness of cast steel as a function of temperature [14]**

Nguyen et al. [8] concluded that the method of shrink-fitting had the most effect on the output parameters. Their work also proved that performing stepped cooling of dipping in dry-ice/alcohol mixture and then dipping in liquid nitrogen would increase the OMCCCL value by as much as 406% and OMSR values by 87% when compared to conventional cooling method of cooling only in liquid nitrogen. This study [8] showed that staged shrink-fitting method of dipping the TH assembly in dry-ice/alcohol mixture and then dipping in liquid nitrogen gives higher OMCCCL values than the shrink-fitting method of dipping in refrigerated air and then in liquid nitrogen as found by Collier et al. [5]. This contrast in results from these two studies [5, 8] clearly shows that the results from the simplified model of compound cylinders as assumed by Collier et al. [5] are not applicable to drawing conclusions about actual THG assembly. However, the results of Nguyen et al. study [8] is limited to AP1 only and there were some limitations with his finite element model.

To extend Nguyen et al. [8] work to AP2, Snyder [9] developed an improved finite element model. Snyder [9] performed the same analysis as Nguyen et al. [8] on AP1 with an improved finite element model and also extended the study to AP2. His work also included analyzing AP3 proposed by Berlin [1]. However, his AP3 analysis included heating of a rectangular plate rather than heating the actual girder geometry. For AP1, Snyder [9] concluded that the medium bridge with high  $\alpha$  value of 0.4 gives higher OMCCCL and OMSR values. Staged shrink-fitting method of cooling in dry-ice/alcohol mixture and then cooling in liquid nitrogen, increased the OMCCCL values in AP1 and AP2 by as much as 897% and 927%, respectively, when compared to single-staged shrink-fitting method of cooling in liquid nitrogen. Snyder's [9] results also agree with Nguyen et al. [8] results that OMCCCL values are significantly higher when the TH assembly is dipped in dry-ice/alcohol mixture first and then in liquid nitrogen when compared to single-staged shrink-fitting method of dipping TH assembly in liquid nitrogen. Snyder's [9] AP3 analysis is not comprehensive but his work included an important observation that in AP3, the critical step is dipping the hub in liquid nitrogen. Both Nguyen et al. [8] and Snyder [9] used ANSI FN2 [65-67] fits for the TH assembly interference as required by FDOT [3]. However, current AASHTO standards call for ANSI FN3 [65-67] fits for TH assemblies. In this study, we have followed the latter standard.

### **1.10 Present Study**

To solve the problem of cracking of the TH assembly when immersed in a cooling medium, an extensive literature search was performed for the analytical solution of transient stresses for a relatively simple model of two long compounded cylinders with

temperature dependent material properties, radial interference between them, and one subjected to thermal boundary conditions. No such model could be found in the literature. Although there are some numerical solutions [5] available in the literature, we thought developing an analytical model would give us a very good insight/understanding of the problem. So, in this study, an analytical solution is developed for one such model (Chapter 2).

Although the analytical solution for two long compounded cylinders is developed, we cannot model the actual TH problem analytically because of the complex geometry of the TH assembly (hub contains gussets etc). Previous studies [8, 9] showed that the results of the compound cylinder problem are not applicable to the actual TH geometry. To solve the cracking of the hub in actual TH geometry, we chose the finite element method approach. To gain confidence in our finite element model, we first built a simple model of two long cylinders and used our analytical solution to validate the approximations of finite element model. During this process we conducted a convergence study of both the finite element model and the analytical model (Chapter 2).

Although previous studies [8, 9] showed staged shrink-fitting method provides significant improvement in OMCCCL values in AP1, the effect of the shrink-fitting method is not measured qualitatively and quantitatively. To find the effect of geometrical parameters like hub radial thickness to hub inner diameter ratio, interference in TH assembly, and the type of shrink-fitting method on the design parameter OMCCCL, a complete full factorial design of experiments (DOE) [59] study is performed on AP1 (Chapter 3).

Although previous studies [2, 8, 9] showed that AP2 gives significantly higher OMCCCL values than AP1, AP2 is not a preferred choice of assembly procedure because AP2 requires manufacturers to ship the trunnion and hub components separately to the construction site. This would overlap the responsibility of the manufacturers of the trunnion and hub and the bridge contractors. Due to this reason, the manufacturers prefer AP1 where they assemble trunnion-hub (TH) components in the factory and ship the TH assembly to the construction site. At the construction site, it is the responsibility of the contractor to perform the final assembly of the TH assembly into the girder. This clearly separates the responsibility of the manufacturers and the bridge contractors. If AP1 is hence the preferred choice of assembly procedure, is it worth to adopt AP2 in some cases? To answer this question, we performed a full factorial design of experiments study on AP2 and then compared these results to that of AP1 so that the contractors have a better reference for the choice of assembly procedures (Chapter 4).

Although, similar studies were conducted on AP1 [8, 9] and AP2 [9], they included TH interference as ANSI FN2 fit [65-67] as requested by the FDOT [3]. However, Association of State Highway and Transportation Officials (AASHTO) standards [65, 66] calls for ANSI FN3 fit [65-67] for TH assemblies. We have adopted the FN3 fit requirements throughout the study.

In Chapter 5, Berlin's [1] finite element model of heating the girder is refined by modeling the heating of the girder with commercially available heating coils, by applying gravity and temperature dependent natural convection coefficients, and by modeling insulation blankets more realistically. Previous work [1] proposed an assembly procedure, called AP3, which studied the possibility of heating the girder rather than

cooling the TH components. But in that work [1], the girder is heated to create sufficient expansion of the girder hole so that only the hub component could go inside. This was followed by the trunnion cooling so that it could go into the hub-girder (HG) assembly. This creates the same overlap of manufacturer-contractor responsibility problem of AP2. In this study, we modified the assembly procedure AP3 so that the girder is to be heated to get clearance for TH assembly (instead of just the hub component) to could go inside the girder hole. We defined two assembly procedures by modifying the previously defined assembly procedure AP3, and called them AP3-A and AP3-B.

In AP3-A, the girder is heated alone to get enough thermal expansion of the girder hole so that the TH assembly at room temperature could completely go inside the girder hole. In AP3-B, girder is heated to get enough expansion of the girder hole so that TH assembly that is dipped in dry-ice/alcohol could completely go inside the girder hole. Heating of the girder can be relatively time consuming. Hence, a full factorial design of experiments study is conducted on the new assembly procedures and compared with traditional assembly procedure AP1 to again give the bridge contractors a better reference for the choice of assembly procedures.

## CHAPTER 2 ANALYTICAL MODELING OF THE PROBLEM

### 2.1 Analytical Modeling

Modeling the TH assembly analytically is quite complex due to the geometry of the TH assembly. So, we instead solve the problem by modeling both the trunnion and hub as two infinitely long hollow cylinders in a compounded configuration. The geometry is shown in Figure 10. The inner radius of the trunnion is taken as  $a$  and the outer radius of the trunnion is taken as  $b + \delta$ , where  $\delta$  is the interference between the trunnion and the hub. The hub is modeled as hollow cylinder with inner radius  $b$  and outer radius  $c$ .

For simplicity, we assume simple temperature boundary conditions of  $T_a$  as the temperature at the inner radius of the trunnion and  $T_c$  as the temperature at the outer radius of the hub. To solve the TH thermal stress problem analytically, we have to solve the thermal problem first to get the temperature distribution at a particular time value and use that temperature distribution to solve for the thermal stresses. The interference stresses are then calculated and superimposed (added) on thermal stresses to give the overall stress state of the assembly.

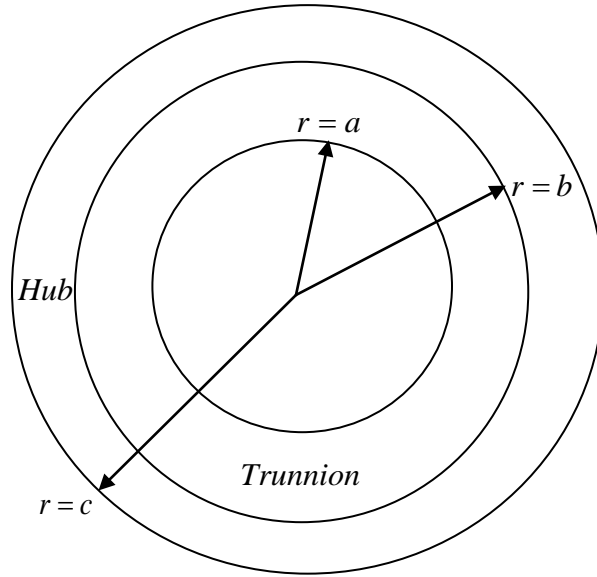


Figure 10 Geometry of trunnion-hub modeled as simple hollow cylinders

## 2.2 Thermal Problem

The heat conduction equation in cylindrical coordinate system is given by [68, 69]

$$\frac{1}{r} \frac{\partial}{\partial r} \left( rk \frac{\partial T}{\partial r} \right) + \frac{1}{r^2} \frac{\partial}{\partial \phi} \left( k \frac{\partial T}{\partial \phi} \right) + \frac{\partial}{\partial z} \left( k \frac{\partial T}{\partial z} \right) = \rho C_p \frac{\partial T}{\partial t}$$

Equation 6 Fourier's heat conduction equation in cylindrical coordinates [68, 69]

where  $r$  = radial coordinate,  $\phi$  = tangential coordinate,  $z$  = axial coordinate,  $k$  = thermal conductivity of the material,  $\rho$  = density of the material,  $C_p$  = specific heat of the material, and  $T(r, t)$  = temperature at a radial distance of  $r$  after a time  $t$ .

As the cylinder is infinitely long,

$$\frac{\partial T}{\partial z} = 0$$

Equation 7 Infinitely long cylinder condition

and as the loading is axisymmetric,

$$\frac{\partial T}{\partial \phi} = 0$$

**Equation 8 Axisymmetric loading condition**

substituting Equation 7 and Equation 8 in Equation 6 gives

$$\frac{1}{r} \frac{\partial}{\partial r} \left( rk(T) \frac{\partial T}{\partial r} \right) = \rho(T) C_p(T) \frac{\partial T}{\partial t}$$

**Equation 9 Fourier's heat conduction equation for a infinitely long cylinder with axisymmetric loading**

Assume the boundary conditions to be

$$T = T_a \text{ at } r = a$$

**Equation 10 Constant temperature boundary condition at the inner surface of the trunnion**

and

$$T = T_c \text{ at } r = c .$$

**Equation 11 Constant temperature boundary condition at the outer surface of the hub**

Let the initial temperature of the two cylinders (trunnion and hub) be  $T_{initial}$ , that is

$$T(r,0) = T_{initial}, \quad a < r < c$$

**Equation 12 Initial temperature of the whole assembly**

The thermal conductivity, specific heat, and density of the material in the Equation 9 are denoted as  $k(T)$ ,  $C_p(T)$ , and  $\rho(T)$ , respectively because these properties are dependent on temperature of the material. The thermal properties of the steel are taken from a metals handbook [70], and are listed in Table 2. Properties are shown from

–120°F to 80°F only because I am checking if the problem could be solved analytically or not.

**Table 2 Thermal material properties of cast steel [70]**

Temperature, $T$ °F	Thermal conductivity, $k(T)$ $\frac{BTU}{\text{sec.in.}^\circ F} \times 10^{-4}$	Specific heat, $C_p(T)$ $\frac{BTU}{\text{lbm.}^\circ F}$	Density, $\rho(T)$ $\frac{\text{lbm}}{\text{in}^3}$
-120	9.23888	0.092	0.3032
-100	9.48888	0.095	0.3015
-80	9.62778	0.098	0.2933
-60	9.76666	0.100	0.2932
-40	9.90556	0.102	0.2872
-20	10.00444	0.104	0.2855
0	10.18334	0.1055	0.2846
20	10.02500	0.107	0.2840
40	10.31666	0.108	0.2833
60	10.38888	0.109	0.2824
80	10.46112	0.110	0.2835

The thermal conductivity of cast steel is found to vary linearly with temperature [69]. Hence we assume that

$$k(T) = k_0(1 + \beta T)$$

**Equation 13 Regression model for thermal conductivity of steel [69]**

where  $k_0$  and  $\beta$  are the regression constants. To solve differential equation denoted by Equation 9, we assume a variable called  $\theta(T)$ , which is given by

$$\theta(T) = \frac{1}{k_0} \int_0^T k(x) dx$$

**Equation 14 Transformation variable, theta**

From Equation 14, we can write

$$\frac{\partial(\theta(T))}{\partial T} = \frac{k(T)}{k_0}$$

**Equation 15 Differentiation of transformation variable with respect to temperature, T**

We can also write

$$\begin{aligned}\frac{\partial(\theta(T))}{\partial r} &= \frac{\partial \theta}{\partial T} \cdot \frac{\partial T}{\partial r} \\ &= \frac{k(T)}{k_0} \frac{\partial T}{\partial r}\end{aligned}$$

Rewriting it gives

$$\frac{\partial T}{\partial r} = \frac{k_0}{k(T)} \frac{\partial \theta}{\partial r}$$

Similarly

$$\frac{\partial T}{\partial t} = \frac{k_0}{k(T)} \frac{\partial \theta}{\partial t}$$

Writing the above two equations together

$$\frac{\partial T}{\partial r} = \frac{k_0}{k(T)} \cdot \frac{\partial(\theta(T))}{\partial r} \quad \text{and} \quad \frac{\partial T}{\partial t} = \frac{k_0}{k(T)} \cdot \frac{\partial(\theta(T))}{\partial t}$$

**Equation 16 Differentiation of temperature in terms of transformation variable theta**

Substituting Equation 16 in Equation 9 gives

$$\frac{1}{r} \frac{\partial \left( rk(T) \frac{k_0}{k(T)} \cdot \frac{\partial(\theta(T))}{\partial r} \right)}{\partial r} = \rho(T) C_p(T) \frac{k_0}{k(T)} \cdot \frac{\partial(\theta(T))}{\partial t}$$

$$\frac{1}{r} \frac{\partial \left( r k_0 \cdot \frac{\partial(\theta(T))}{\partial r} \right)}{\partial r} = \frac{k_0}{\alpha(T)} \cdot \frac{\partial(\theta(T))}{\partial t}$$

**Equation 17 Transformed conduction equation in terms of transformation variable theta**

where  $\alpha(T) = \frac{k(T)}{\rho(T) \cdot C_p(T)}$  is called the thermal diffusivity of the material. For cast

steels, the thermal diffusivity is found to be a very weak function of temperature [69]. To

check this result, the  $\frac{k}{\rho \cdot C_p}$  value is found at every temperature value from the material

properties of the steel given in Table 2. The value is almost constant and hence in this

modeling the value of thermal diffusivity is taken as constant. Hypothesis testing

showing  $\alpha$  is not a function temperature is given in Appendix A. Hence, in further

equations it is denoted as  $\alpha$  instead of  $\alpha(T)$ . Expanding Equation 17, gives

$$\frac{\partial^2 \theta(T)}{\partial r^2} + \frac{1}{r} \frac{\partial \theta(T)}{\partial r} = \frac{1}{\alpha} \cdot \frac{\partial \theta(T)}{\partial t}$$

Multiplying on both sides by  $r^2$  gives

$$r^2 \frac{\partial^2 \theta(T)}{\partial r^2} + r \frac{\partial \theta(T)}{\partial r} = \frac{r^2}{\alpha} \cdot \frac{\partial \theta(T)}{\partial t}$$

$$r^2 \frac{\partial^2 \theta}{\partial r^2} + r \frac{\partial \theta}{\partial r} = \frac{r^2}{\alpha} \cdot \frac{\partial \theta}{\partial t}$$

**Equation 18 Simplified form of transformed conduction equation**

Now because we transformed the differential equation (Equation 9) in terms of  $\theta$  (Equation 18), we change the boundary conditions and initial conditions also.

$$\theta(a, t) = \theta_a, \quad \theta(c, t) = \theta_c, \quad \text{and} \quad \theta(r, 0) = \theta_{initial}$$

The values of  $\theta_a$ ,  $\theta_c$ , and  $\theta_{initial}$  are found by substituting the values of  $T_a$ ,  $T_c$ , and  $T_{initial}$  for  $T$ , respectively in Equation 14.

Equation 18 is the differential equation to be solved to get the solution  $\theta(r,t)$ .

After obtaining the  $\theta$  values, the temperature  $T$  could be found.

Let us assume the solution of the differential equation to be,

$$\theta(r,t) = \theta_s(r) + \theta_{trans}(r,t)$$

**Equation 19 Transformed conduction equation solution is the sum of steady state and transient solutions**

where  $\theta_s(r)$  is the steady-state solution and  $\theta_{trans}(r,t)$  is the transient solution. Also the boundary conditions could also be broken as  $\theta_s(a) = \theta_a$  and  $\theta_s(c) = \theta_c$  for steady-state and  $\theta_{trans}(a,t) = 0$  and  $\theta_{trans}(c,t) = 0$  for the transient solution. Also, for the transient solution, the initial condition is  $\theta_{trans}(r,0) = \theta_{initial} - \theta_s(r)$ .

### 2.2.1 Steady State Solution

As  $\theta_s(r)$  is the steady state solution, substituting it in Equation 18 gives

$$r^2 \frac{\partial^2 \theta_s}{\partial r^2} + r \frac{\partial \theta_s}{\partial r} = 0$$

**Equation 20 Transformed steady state equation**

Equation 20 is a Cauchy-Euler equation and the solution will be of the form,

$\theta_s = r^m$ . Substituting  $\theta_s = r^m$  in Equation 20 gives

$$r^2 \frac{\partial^2 r^m}{\partial r^2} + r \frac{\partial r^m}{\partial r} = 0$$

$$r^2 .m.(m-1).r^{m-2} + r.m.r^{m-1} = 0$$

$$\begin{aligned}
m(m-1) + m &= 0 \\
m(m-1+1) &= 0 \\
m^2 &= 0
\end{aligned}$$

Therefore the solution will be of the form  $\theta_s(r) = C_1 + C_2 \ln(r)$ . Substituting the boundary conditions  $\theta_s(a) = \theta_a$  and  $\theta_s(c) = \theta_c$ , we get two equations

$$\theta_a = C_1 + C_2 \ln(a)$$

and

$$\theta_c = C_1 + C_2 \ln(c).$$

Solving these two equations we get the constants  $C_1$  and  $C_2$  as

$$C_1 = \frac{\theta_c \ln(a) - \theta_a \ln(c)}{\ln(a) - \ln(c)} \text{ and } C_2 = \frac{\theta_a - \theta_c}{\ln(a) - \ln(c)}$$

Therefore the steady state solution is given as

$$\theta_s(r) = \frac{\theta_c \ln(a) - \theta_a \ln(c)}{\ln(a) - \ln(c)} + \frac{\theta_a - \theta_c}{\ln(a) - \ln(c)} \ln(r)$$

**Equation 21 Steady state solution of the transformed conduction equation**

### 2.2.2 Transient Solution

As  $\theta_{trans}(r, t)$  is the steady state solution, substituting it in Equation 18 gives

$$r^2 \frac{\partial^2 \theta_{trans}}{\partial r^2} + r \frac{\partial \theta_{trans}}{\partial r} = \frac{r^2}{\alpha} \cdot \frac{\partial \theta_{trans}}{\partial t}$$

**Equation 22 Transformed transient conduction equation**

Let us assume the transient solution is a product of spatial function  $R(r)$  and temporal function  $\tau(t)$  which are independent of each other. Hence

$$\theta_{trans} = R(r)\tau(t)$$

**Equation 23 Transient solution as product of temporal and spatial solutions**

where  $R(r)$  and  $\tau(t)$  are the function of  $r$  and  $t$ , respectively. Substituting

$\theta_{trans} = R(r)\tau(t)$  in Equation 22 gives

$$r^2 \cdot \tau \cdot R'' + r \cdot \tau \cdot R' = \frac{r^2}{\alpha} R \cdot \tau'$$

**Equation 24 Transformed transient conduction equation in terms of spatial and temporal functions**

where  $R'' = \frac{\partial^2 R}{\partial r^2}$ ,  $R' = \frac{\partial R}{\partial r}$ , and  $\tau' = \frac{\partial \tau}{\partial t}$ . Rearranging the term in Equation 24 we get

$$\frac{r \cdot R'' + R'}{rR} = \frac{1}{\alpha} \cdot \frac{\tau'}{\tau}$$

**Equation 25 Rearranged transformed transient conduction equation**

Let us say the Equation 25 is equal to  $-\lambda^2$ . That is

$$\frac{r \cdot R'' + R'}{rR} = \frac{1}{\alpha} \cdot \frac{\tau'}{\tau} = -\lambda^2 \text{ (say)}$$

**Equation 26 Rearranged transformed conduction equal to a constant**

**2.2.2.1 Temporal Solution**

From Equation 26, considering only the temporal equation gives

$$\frac{1}{\alpha} \cdot \frac{\tau'}{\tau} = -\lambda^2$$

Rewriting the above equation gives

$$\tau' + \lambda^2 \alpha \tau = 0$$

**Equation 27 Temporal differential equation**

Solution to this equation is of the form  $\tau = e^{mt}$ . Substituting  $\tau = e^{mt}$  in Equation 27 gives

$$me^{mt} + \lambda^2 \alpha e^{mt} = 0$$

$$m = -\lambda^2 \alpha .$$

Therefore the temporal solution is given by

$$\tau(t) = C_3 e^{-\lambda^2 \alpha t}$$

**Equation 28 Solution to the temporal differential equation**

In Equation 28,  $C_3$  is a constant.

**2.2.2.2 Spatial Solution**

From Equation 26, considering only the spatial equation gives

$$\frac{r.R'' + R'}{rR} = -\lambda^2$$

Rewriting the above equation gives

$$R'' + \frac{1}{r}R' + \lambda^2 R = 0$$

**Equation 29 Spatial differential equation**

The solution to this equation is given in Bessel's functions of first and second kind,

$$R(r) = C_4 J_0(\lambda r) + C_5 Y_0(\lambda r)$$

**Equation 30 Solution to the spatial differential equation**

where  $C_4$  and  $C_5$  are constants. Therefore, substituting Equation 28 and Equation 29 in

Equation 23 gives

$$\theta_{trans} = [C_4 J_0(\lambda r) + C_5 Y_0(\lambda r)] C_3 e^{-\lambda^2 \alpha t}$$

$$\theta_{trans} = [A J_0(\lambda r) + B Y_0(\lambda r)] e^{-\lambda^2 \alpha t}$$

where  $A$  ( $A = C_3 \cdot C_4$ ) and  $B$  ( $B = C_3 \cdot C_5$ ) are new constants. Applying the boundary conditions for the transient solution, that is  $\theta_{trans}(a, t) = 0$  and  $\theta_{trans}(c, t) = 0$ , gives the following equations

$$A J_0(\lambda a) + B Y_0(\lambda a) = 0$$

**Equation 31 Transient boundary condition at inner radius of the trunnion**

and

$$A J_0(\lambda c) + B Y_0(\lambda c) = 0$$

**Equation 32 Transient boundary condition at outer radius of the hub**

Writing these equations in matrix form gives

$$\begin{bmatrix} J_0(\lambda a) & Y_0(\lambda a) \\ J_0(\lambda c) & Y_0(\lambda c) \end{bmatrix} \begin{bmatrix} A \\ B \end{bmatrix} = \begin{bmatrix} 0 \\ 0 \end{bmatrix}$$

**Equation 33 Transient boundary conditions in matrix form**

For having a solution, the determinant of the coefficient matrix in the Equation 33 should be zero. Therefore

$$J_0(\lambda a) Y_0(\lambda c) - J_0(\lambda c) Y_0(\lambda a) = 0$$

**Equation 34 Equation to obtain eigenvalues of the problem**

This Equation 34 has infinite roots called eigenvalues and is denoted by  $\lambda_1, \lambda_2, \lambda_3, \dots, \lambda_\infty$ . The eigenvalues of the Equation 34 are obtained by using the open source numerical subroutines developed in MATLAB [71] by the chebfun group [72] at

Oxford University. Please note that only positive eigenvalues are considered due to the physics of the problem. The solution will be of the form

$$\theta_{trans} = \sum_{i=1}^{\infty} [A_i J_0(\lambda_i r) + B_i Y_0(\lambda_i r)] e^{-\lambda_i^2 a t}$$

**Equation 35 Transient solution**

Also rewriting the Equation 31 gives

$$B_i = -\frac{J_0(\lambda_i a)}{Y_0(\lambda_i a)} A_i$$

Substituting the value of  $B_i$  in Equation 35 gives

$$\begin{aligned} \theta_{trans} &= \sum_{i=1}^{\infty} A_i \left[ J_0(\lambda_i r) - \frac{J_0(\lambda_i a)}{Y_0(\lambda_i a)} Y_0(\lambda_i r) \right] e^{-\lambda_i^2 a t} \\ \theta_{trans} &= \sum_{i=1}^{\infty} A_i \left[ \frac{J_0(\lambda_i r) Y_0(\lambda_i a) - J_0(\lambda_i a) Y_0(\lambda_i r)}{Y_0(\lambda_i a)} \right] e^{-\lambda_i^2 a t} \\ \theta_{trans} &= \sum_{i=1}^{\infty} A_i \varphi(\lambda_i r) e^{-\lambda_i^2 a t} \end{aligned}$$

**Equation 36 Simplified transient solution**

This is the transient solution, where  $\varphi(\lambda_i r) = \left[ \frac{J_0(\lambda_i r) Y_0(\lambda_i a) - J_0(\lambda_i a) Y_0(\lambda_i r)}{Y_0(\lambda_i a)} \right]$ . Using

the initial condition, gives

$$\sum_{i=1}^{\infty} A_i \varphi(\lambda_i r) = \theta_{initial} - \theta_s$$

**Equation 37 Equation obtained by applying initial condition**

Using the orthogonality of the eigen function,  $\varphi(\lambda_i r)$  [73]

$$\int_a^b r\varphi(\lambda_i r)\varphi(\lambda_j r)dr = 0 ; i \neq j \text{ and } \int_a^b r\varphi^2(\lambda_i r)dr = \left[ \frac{r^2}{2} (\varphi(\lambda_i r)^2 + \varphi'(\lambda_i r)^2) \right]_a^b ; i = j$$

For obtaining  $A_i$ , both sides of Equation 37 should be multiplied by  $r\varphi(\lambda_i r)$  and integrated from  $a$  to  $b$ .

$$A_i = \frac{(\theta_{initial} - \theta_s) \int_a^b r\varphi(\lambda_i r)dr}{\left[ \frac{r^2}{2} (\varphi(\lambda_i r)^2 + \varphi'(\lambda_i r)^2) \right]_a^b}$$

Hence, the final solution to the differential equation (Equation 18) is obtained by substituting Equation 21 and Equation 36 in Equation 19.

$$\theta = \frac{\theta_b \ln(a) - \theta_a \ln(b)}{\ln(a) - \ln(b)} + \frac{\theta_a - \theta_b}{\ln(a) - \ln(b)} \ln(r) + \sum_{i=1}^{\infty} A_i \varphi(\lambda_i r) e^{-\lambda_i^2 \alpha t}$$

#### Equation 38 Final solution of the transformed conduction equation

Substituting Equation 13 in Equation 14 gives

$$\begin{aligned} \theta(T) &= \frac{1}{k_0} \int_0^T k_0 (1 + \beta x) dx \\ &= T + \beta \frac{T^2}{2} \end{aligned}$$

To get the temperature distribution at a particular time, the entire radial space in the compound cylinder is divided (mesh) into  $n$  equal segments and  $\theta$  is found at each node of the mesh by substituting the radial location of the node in Equation 38. For illustrative purposes, a simple mesh with 4 segments is shown in Figure 11.

Once  $\theta$  is obtained from Equation 38 by using the quadratic formula,  $T$  is found at different radial locations. Out of the two values of  $T$  obtained from the quadratic formula, the value of  $T$  which is in between  $T_a$  and  $T_b$  is taken as the actual temperature

value (physically acceptable root). Mathematically it is represented as  $T_a \leq T \leq T_b$ . All the nodal locations, temperatures of the nodes are stored in separate vectors denoted by  $RR$  and  $TT$ , respectively. Hence

$$RR = \begin{bmatrix} a \\ a + \delta r \\ a + 2\delta r \\ \cdot \\ \cdot \\ \cdot \\ \cdot \\ \cdot \\ \cdot \\ c \end{bmatrix} \quad \text{and} \quad TT = \begin{bmatrix} T_a \\ \cdot \\ T_c \end{bmatrix}$$

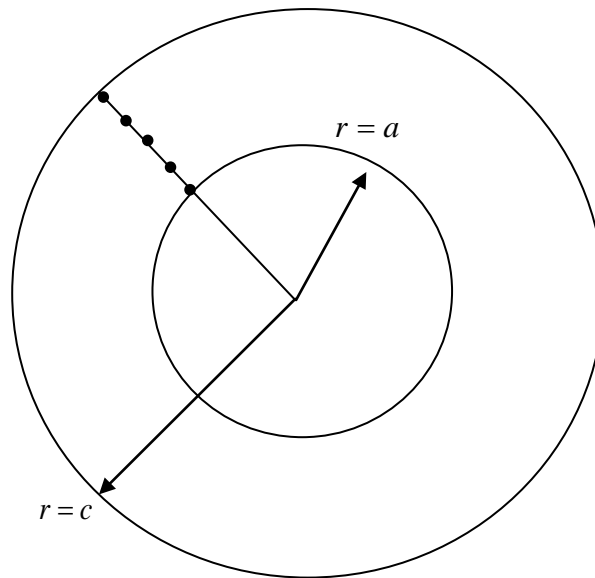


**Figure 11 Radial mesh for analytical temperature distribution**

The number of rows in the vector  $RR$  and  $TT$  is  $n+1$  (number of nodes). Please note that temperature is only a function of  $r$  at any particular time. Therefore, for the structural problem, the load (temperature) is axisymmetric.

## 2.3 Thermal Stresses

The stresses in cylindrical coordinate system are given by

$$\sigma_{rr}^{thermal} = \frac{2G}{1-2\nu} \left[ (1-\nu)\varepsilon_{rr}^{thermal} + \nu\varepsilon_{\phi\phi}^{thermal} + \nu\varepsilon_{zz}^{thermal} \right] - \int_{T_{initial}}^{T(r,t)} \frac{\alpha_x(T)E}{1-2\nu} dT$$

**Equation 39 Radial stress in cylindrical coordinate system**

$$\sigma_{\phi\phi}^{thermal} = \frac{2G}{1-2\nu} \left[ (1-\nu)\varepsilon_{\phi\phi}^{thermal} + \nu\varepsilon_{rr}^{thermal} + \nu\varepsilon_{zz}^{thermal} \right] - \int_{T_{initial}}^{T(r,t)} \frac{\alpha_x(T)E}{1-2\nu} dT$$

**Equation 40 Tangential or hoop stress in cylindrical coordinate system**

$$\sigma_{zz}^{thermal} = \frac{2G}{1-2\nu} \left[ (1-\nu)\varepsilon_{zz}^{thermal} + \nu\varepsilon_{rr}^{thermal} + \nu\varepsilon_{\phi\phi}^{thermal} \right] - \int_{T_{initial}}^{T(r,t)} \frac{\alpha_x(T)E}{1-2\nu} dT$$

**Equation 41 Axial stress in cylindrical coordinate system**

where  $\sigma_{rr}^{thermal}$  is the radial stress,  $\sigma_{\phi\phi}^{thermal}$  is the tangential or hoop stress,  $\sigma_{zz}^{thermal}$  is the axial stress,  $G$  is the shear modulus of the material ( $G = \frac{E}{2(1+\nu)}$ ;  $E$  - Young's modulus of the material and  $\nu$  - Poisson's ratio of the material),  $\alpha_x(T)$  is thermal expansion coefficient of the material which a function of temperature. The variables  $\varepsilon_{rr}^{thermal}$ ,  $\varepsilon_{\phi\phi}^{thermal}$  and  $\varepsilon_{zz}^{thermal}$  are the strains in radial, tangential and axial directions, respectively. The superscript "thermal" is used in the stresses and strains variable only to emphasize that the stresses and strains are due to thermal (temperature) loading only. For the cast steel (ASTM A36) used in bridges, the material properties are taken from metals handbook [70] and are listed in Table 3.

**Table 3 Structural material properties of the steel for this study [70]**

Temperature, $T$ $^{\circ}F$	Coefficient of thermal expansion, $\alpha_x(T)$ $\frac{\mu in}{in.^{\circ}F}$	$E = 29 Msi$ $\nu = 0.26$
-120	5.09	
-100	5.28	
-80	5.43	
-60	5.58	
-40	5.72	
-20	5.86	
0	6.00	
20	6.12	
40	6.24	
60	6.36	
80	6.47	

For infinitely long cylinders and axisymmetric loading, the strains are given by

$$\varepsilon_{rr}^{thermal} = \frac{du^{thermal}}{dr}$$

**Equation 42 Radial strain in cylindrical coordinate system**

$$\varepsilon_{\phi\phi}^{thermal} = \frac{u^{thermal}}{r}$$

**Equation 43 Tangential strain in cylindrical coordinate system**

and assuming generalized plane strain condition, we have

$$\varepsilon_{zz}^{thermal} = \varepsilon \text{ (constant)}$$

**Equation 44 Axial strain in cylindrical coordinate system**

where  $u$  is the displacement in radial direction. Substituting Equation 42, Equation 43, and Equation 44 in Equation 39, Equation 40, and Equation 41, respectively we get

$$\sigma_{rr}^{thermal} = \frac{2G}{1-2\nu} \left[ (1-\nu) \frac{du^{thermal}}{dr} + \nu \frac{u^{thermal}}{r} + \nu \varepsilon \right] - \int_{T_{initial}}^{T(r,t)} \frac{\alpha_x(T)E}{1-2\nu} dT$$

**Equation 45 Radial stress as a function of radial displacement**

$$\sigma_{\phi\phi}^{thermal} = \frac{2G}{1-2\nu} \left[ (1-\nu) \frac{u^{thermal}}{r} + \nu \frac{du^{thermal}}{dr} + \nu \varepsilon \right] - \int_{T_{initial}}^{T(r,t)} \frac{\alpha_x(T)E}{1-2\nu} dT$$

**Equation 46 Hoop stress as a function of radial displacement**

$$\sigma_{zz}^{thermal} = \frac{2G}{1-2\nu} \left[ (1-\nu) \varepsilon + \nu \frac{du^{thermal}}{dr} + \nu \frac{u^{thermal}}{r} \right] - \int_{T_{initial}}^{T(r,t)} \frac{\alpha_x(T)E}{1-2\nu} dT$$

**Equation 47 Axial stress as a function of radial displacement**

Considering the elementary force balance equation, we have

$$\frac{d\sigma_{rr}^{thermal}}{dr} + \frac{\sigma_{rr}^{thermal} - \sigma_{\phi\phi}^{thermal}}{r} = 0$$

**Equation 48 Elementary force balance equation**

Substituting Equation 45 and Equation 46 in Equation 48, and upon simplification we get the differential equation

$$\frac{d^2 u^{thermal}}{dr^2} + \frac{1}{r} \frac{du^{thermal}}{dr} - \frac{u^{thermal}}{r^2} = \frac{1+\nu}{1-\nu} \frac{d \left( \int_{T_{initial}}^{T(r,t)} \alpha_x(T) dT \right)}{dr}$$

$$\frac{d \left[ \frac{du^{thermal}}{dr} + \frac{u^{thermal}}{r} \right]}{dr} = \frac{1+\nu}{1-\nu} \frac{d \left( \int_{T_{initial}}^{T(r,t)} \alpha_x(T) dT \right)}{dr}$$

Integrating with respect to  $r$  gives

$$\frac{du^{thermal}}{dr} + \frac{u^{thermal}}{r} = \frac{1+\nu}{1-\nu} \int_{T_{initial}}^{T(r,t)} \alpha_x(T) dT + C_8$$

where  $C_8$  is an integration constant. Multiplying both sides by  $r$  yields

$$r \frac{du^{thermal}}{dr} + u^{thermal} = r \frac{1+\nu}{1-\nu} \int_{T_{initial}}^{T(r,t)} \alpha_x(T) dT + C_8 r$$

$$\frac{d[ru^{thermal}]}{dr} = r \frac{1+\nu}{1-\nu} \int_{T_{initial}}^{T(r,t)} \alpha_x(T) dT + C_8 r$$

Integrating with respect to  $r$  from  $a$  to  $r$  gives,

$$ru^{thermal} = \frac{1+\nu}{1-\nu} \int_a^r \left[ r \int_{T_{initial}}^{T(r,t)} \alpha_x(T) dT \right] dr + C_8 \frac{r^2}{2} + C_9$$

where  $C_9$  is integration constant. Dividing both sides by  $r$

$$u^{thermal} = \frac{1+\nu}{r(1-\nu)} \int_a^r \left[ r \int_{T_{initial}}^{T(r,t)} \alpha_x(T) dT \right] dr + C_8 \frac{r}{2} + \frac{C_9}{r}$$

we define a constant  $C_{10} = \frac{C_8}{2}$ .

$$u^{thermal} = \frac{1+\nu}{r(1-\nu)} \int_a^r \left[ r \int_{T_{initial}}^{T(r,t)} \alpha_x(T) dT \right] dr + C_{10} r + \frac{C_9}{r}$$

#### Equation 49 Radial displacement solution in cylindrical coordinates

It is found that for cast steels, the best fit for thermal expansion coefficient is the second order polynomial. Using  $\alpha_x(T) = a_0 + a_1 T + a_2 T^2$  as the regression model, and substituting it in Equation 49, we have

$$u^{thermal}(r) = \frac{1}{r} \frac{1+\nu}{1-\nu} \int_a^r r \int_{T_{initial}}^{T(r,t)} (a_0 + a_1 T + a_2 T^2) dT dr + C_{10} r + \frac{C_9}{r}$$

**Equation 50 Simplified displacement solution**

Equation 50 can be broken now into vector form as

$$[U]^{thermal} = \frac{1+\nu}{1-\nu} [RR_{inv}] \int_a^r [Thermalload] dr + C_{10} [RR] + C_9 [RR_{inv}]$$

**Equation 51 Radial displacement in vector form**

where  $U$  is the vector which contains the radial displacement of each node. The

$Thermalload$  vector at each node is obtained by calculating the  $\int_{T_{initial}}^{T(r,t)} (a_0 + a_1 T + a_2 T^2) dT$

value by substituting  $T(r,t)$  with the temperature of the node. The resultant number is then multiplied by the radial location of the node.

$$RR = \begin{bmatrix} a \\ a + \delta r \\ a + 2\delta r \\ \cdot \\ \cdot \\ \cdot \\ \cdot \\ \cdot \\ \cdot \\ c \end{bmatrix},$$

$$RR_{inv} = \begin{bmatrix} \frac{1}{a} \\ \frac{1}{a + \delta r} \\ \frac{1}{a + 2\delta r} \\ \cdot \\ \cdot \\ \cdot \\ \cdot \\ \cdot \\ \cdot \\ \frac{1}{c} \end{bmatrix} \text{ and}$$

$$Thermalload = \begin{bmatrix} RR_{1,1} \int_{T_{initial}}^{T_{1,1}} (a_0 + a_1 T + a_2 T^2) dT \\ RR_{2,1} \int_{T_{initial}}^{T_{2,1}} (a_0 + a_1 T + a_2 T^2) dT \\ RR_{3,1} \int_{T_{initial}}^{T_{3,1}} (a_0 + a_1 T + a_2 T^2) dT \\ \cdot \\ \cdot \\ \cdot \\ \cdot \\ \cdot \\ \cdot \\ RR_{n+1,1} \int_{T_{initial}}^{T_{n+1,1}} (a_0 + a_1 T + a_2 T^2) dT \end{bmatrix}$$

The vector  $RR$  contains the radial location of the nodes. The vector  $RR_{inv}$  contains 1/radial location ( $1/r$ ) of the node. In Equation 51,  $\int_a^r [Thermalload] dr$  is found at each node by numerical integration of discrete data. The resultant vector is named as  $Thermal$ . Now Equation 51 can be written as

$$[U]^{thermal} = \frac{1+\nu}{1-\nu} [RR_{inv}] [Thermal] + C_{10} [RR] + C_9 [RR_{inv}]$$

**Equation 52 Simplified radial displacement in vector form**

The product of the vectors,  $RR_{inv}$  and  $Thermal$  is not the actual matrix multiplication but it is a vector (one dimensional matrix) obtained by multiplying the corresponding elements of the two vectors. The resultant vector is then multiplied by  $\frac{1+\nu}{1-\nu}$ . For simplification, this vector is named as  $RThermal$ , so Equation 52 reduces to

$$[U]^{thermal} = [RThermal] + C_{10} [RR] + C_9 [RR_{inv}]$$

**Equation 53 Final radial displacement equation**

$$RThermal = \frac{1+\nu}{1-\nu} \begin{bmatrix} RR_{inv_{1,1}} \cdot Thermal_{1,1} \\ RR_{inv_{2,1}} \cdot Thermal_{2,1} \\ RR_{inv_{3,1}} \cdot Thermal_{3,1} \\ \cdot \\ \cdot \\ \cdot \\ \cdot \\ \cdot \\ \cdot \\ RR_{inv_{n+1,1}} \cdot Thermal_{n+1,1} \end{bmatrix}$$

Please note that  $C_9$  and  $C_{10}$  are still unknown constants. Now,  $\frac{du}{dr}$  is obtained by the

following steps. From Equation 50 and Equation 53 we can write

$$[U]^{thermal} = [RThermal] + C_{10} [RR] + C_9 [RR_{inv}]$$

$$\frac{d[U]^{thermal}}{dr} = \frac{d[RThermal]}{dr} + C_{10} \frac{d[RR]}{dr} + C_9 \frac{d[RR_{inv}]}{dr}$$

$$[DU]^{thermal} = [DRThermal] + C_{10}[I] + C_9[DRR_{inv}]$$

**Equation 54 Differential of radial displacement in vector form**

where vector  $[DRThermal]$  is obtained by numerical differentiation of  $[RThermal]$  vector with respect to vector  $[RR]$ . While calculating the numerical differentiation, second order accuracy equations were used to reduce the error.  $[I]$  is the vector with all the elements equal to a value of 1. The vector  $[DRR_{inv}]$  is obtained by finding the value of  $-1/(\text{radial location of the node})^2$ .

$$DRR_{inv} = \begin{bmatrix} \frac{-1}{a^2} \\ \frac{-1}{(a + \delta r)^2} \\ \frac{-1}{(a + 2\delta r)^2} \\ \cdot \\ \cdot \\ \cdot \\ \cdot \\ \cdot \\ \cdot \\ \frac{-1}{c^2} \end{bmatrix}, \text{ and } I = \begin{bmatrix} 1 \\ 1 \\ 1 \\ \cdot \\ \cdot \\ \cdot \\ \cdot \\ \cdot \\ \cdot \\ 1 \end{bmatrix}$$

Now  $\frac{u}{r}$  is obtained by the following steps. From Equation 50 and Equation 53 we

can write

$$[U]^{thermal} = [RThermal] + C_{10}[RR] + C_9[RR_{inv}]$$

$$\frac{[U]^{thermal}}{r} = \frac{[RThermal]}{r} + C_{10} \frac{[RR]}{r} + C_9 \frac{[RR_{inv}]}{r}$$

$$[UbyR]^{thermal} = [RThermalbyR] + C_{10}[I] + C_9[RR_{inv}byR]$$

**Equation 55 Radial displacement over radial location in vector form**

where

$$RR_{inv}byR = \begin{bmatrix} \frac{1}{a^2} \\ \frac{1}{(a + \delta r)^2} \\ \frac{1}{(a + 2\delta r)^2} \\ \cdot \\ \cdot \\ \cdot \\ \cdot \\ \cdot \\ \frac{1}{c^2} \end{bmatrix}, \quad RThermalbyR = \begin{bmatrix} \frac{RThermal_{1,11}}{a} \\ \frac{RThermal_{2,11}}{a + \delta r} \\ \frac{RThermal_{3,11}}{a + 2\delta r} \\ \cdot \\ \cdot \\ \cdot \\ \cdot \\ \frac{RThermal_{n+1,11}}{c} \end{bmatrix}$$

Substituting Equation 53, Equation 54, and Equation 55 in Equation 45, Equation 46, and Equation 47, respectively gives the stresses in vector form as

$$[\sigma_{rr}]^{thermal} = \frac{2G}{1-2\nu} [(1-\nu)[DU] + \nu[UbyR] + \nu\varepsilon] - [Thermalload]$$

**Equation 56 Radial stress as a function of radial displacement in vector form**

$$[\sigma_{\phi\phi}]^{thermal} = \frac{2G}{1-2\nu} [(1-\nu)[UbyR]^{thermal} + \nu[DU]^{thermal} + \nu\varepsilon] - [Thermalload]$$

**Equation 57 Hoop stress as a function of radial displacement in vector form**

$$[\sigma_{zz}]^{thermal} = \frac{2G}{1-2\nu} [(1-\nu)\varepsilon + \nu[DU]^{thermal} + \nu[UbyR]^{thermal}] - [Thermalload]$$

**Equation 58 Axial stress as a function of radial displacement in vector form**

Please note that in these equations (Equation 56, Equation 57, and Equation 58),  $C_9$ ,  $C_{10}$ , and  $\varepsilon$  are still unknown constants. We solve for these constants by using the following conditions.

At the inner radius,  $r = a$ , the radial stress is zero (free surface). Therefore the first row in the  $[\sigma_{rr}]$  vector is zero.

$$[\sigma_{rr}]_{1,1}^{thermal} = 0$$

**Equation 59 Free surface boundary condition at the inner radius**

At the outer radius,  $r = c$  the radial stress is zero (free surface). Therefore the last row in the  $[\sigma_{rr}]$  vector is zero.

$$[\sigma_{rr}]_{n+1,1}^{thermal} = 0$$

**Equation 60 Free surface boundary condition at the outer radius**

Equation 59 and Equation 60 gives two equations, and we need one more equation to solve for constants  $C_9$ ,  $C_{10}$ , and  $\varepsilon$ . The third equation is obtained from the generalized plane strain condition which states that the the overall axial force is zero.

$$\int_a^c 2\pi r \sigma_{zz} dr = 0$$

**Equation 61 Overall axial force is zero**

This equation is setup by numerical integration (trapezoidal rule) for discrete data of the vectors  $[RR]$  and  $[R\sigma_{zz}]$ , where

$$R\sigma_{zz} = \begin{bmatrix} RR_{1,1} \cdot \sigma_{zz,1}^{thermal} \\ RR_{2,1} \cdot \sigma_{zz,1}^{thermal} \\ RR_{3,1} \cdot \sigma_{zz,1}^{thermal} \\ \cdot \\ \cdot \\ \cdot \\ \cdot \\ \cdot \\ \cdot \\ RR_{n+1,1} \cdot \sigma_{zz,n+1,1}^{thermal} \end{bmatrix}$$

Solving Equation 59, Equation 60, and Equation 61 gives three values of the constants, and hence the stresses and displacements for a particular temperature distribution are obtained.

## 2.4 Interference Stress

If  $\delta$  is the interference present between two cylinders which are press or shrink-fit then the interface pressure,  $P_{interface}$  is given by Equation 62 [63, 74-76].

$$P_{interface} = \frac{E\delta}{b} \left[ \frac{(c^2 - b^2)(b^2 - a^2)}{2b^2(c^2 - a^2)} \right]$$

**Equation 62 Interface pressure developed between the two shrink-fit components**

This interface pressure  $P_{interface}$  acts as a compressive radial stress on the outer surface of the inner cylinder, which in this case is the trunnion; and on the inner surface of the outer cylinder, which in this case is the hub.

### 2.4.1 Interference Stresses in Trunnion

The trunnion could be modeled as a hollow thick cylinder with no pressure acting on the inside surface and a pressure,  $P_{\text{interface}}$  (compressive radial stress) acting on the outer surface (Figure 12).

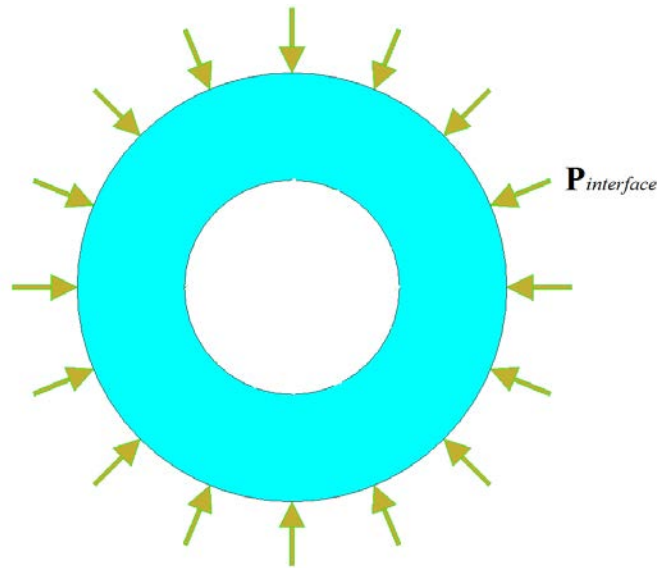


Figure 12 Trunnion modeled as thick cylinder with external pressure

For a thick walled cylinder with internal and external radii of  $a$  and  $b$ , respectively and with no internal pressure, and external pressure of  $P_{\text{interface}}$ , the stresses are given by [74, 76, 77].

$$\sigma_{rr}^{\text{interference}} = \frac{-b^2 P_{\text{interface}}}{b^2 - a^2} - \frac{-P_{\text{interface}} a^2 b^2}{(b^2 - a^2) r^2}$$

$$\sigma_{\phi\phi}^{\text{interference}} = \frac{-b^2 P_{\text{interface}}}{b^2 - a^2} + \frac{-P_{\text{interface}} a^2 b^2}{(b^2 - a^2) r^2}$$

$$\sigma_{zz}^{\text{interference}} = 0$$

All the above equations are valid in the domain  $a \leq r \leq b$ .

## 2.4.2 Interference Stresses in Hub

The hub is modeled as a hollow thick cylinder with  $P_{\text{interface}}$  (compressive radial stress) pressure acting on the inside surface and with no pressure acting on the outer surface (Figure 13).

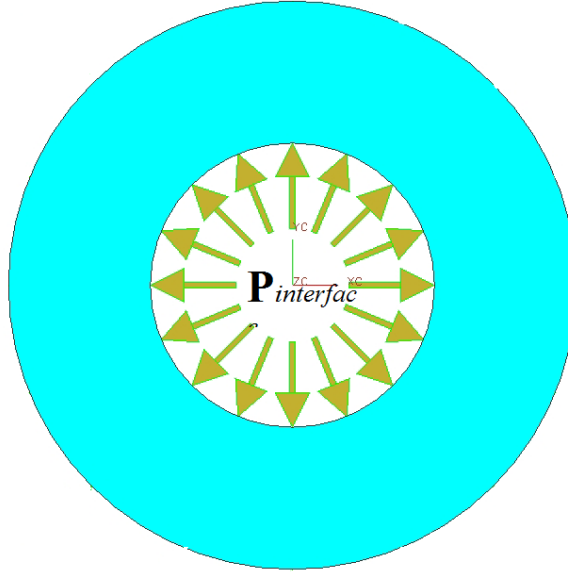


Figure 13 Hub modeled as thick cylinder with internal pressure

For a thick walled cylinder with internal and external radii of  $b$  and  $c$ , respectively and with no external pressure, and internal pressure of  $P_{\text{interface}}$ , the stresses are given by [74, 76, 77]

$$\sigma_{rr}^{\text{interference}} = \frac{b^2 P_{\text{interface}}}{c^2 - b^2} - \frac{P_{\text{interface}} b^2 c^2}{(c^2 - b^2) r^2}$$

$$\sigma_{\phi\phi}^{\text{interference}} = \frac{b^2 P_{\text{interface}}}{b^2 - c^2} + \frac{P_{\text{interface}} b^2 c^2}{(c^2 - b^2) r^2}$$

$$\sigma_{zz}^{\text{interference}} = 0$$

All the above equations are valid in the domain  $b \leq r \leq c$ .

### 2.4.3 Interference Stresses in the Assembly

The interference stress in the assembly, in the hub and trunnion are given by the equations

$$\sigma_{rr}^{\text{interference}} = \begin{cases} \frac{-b^2 P_{\text{interface}}}{b^2 - a^2} - \frac{-P_{\text{interface}} a^2 b^2}{(b^2 - a^2) r^2} & a \leq r \leq b \\ \frac{b^2 P_{\text{interface}}}{c^2 - b^2} - \frac{P_{\text{interface}} b^2 c^2}{(c^2 - b^2) r^2} & b \leq r \leq c \end{cases}$$

**Equation 63 Radial interference stress in the assembly**

$$\sigma_{\phi\phi}^{\text{interference}} = \begin{cases} \frac{-b^2 P_{\text{interface}}}{b^2 - a^2} + \frac{-P_{\text{interface}} a^2 b^2}{(b^2 - a^2) r^2} & a \leq r \leq b \\ \frac{b^2 P_{\text{interface}}}{c^2 - b^2} + \frac{P_{\text{interface}} b^2 c^2}{(c^2 - b^2) r^2} & b \leq r \leq c \end{cases}$$

**Equation 64 Tangential interference stress in the assembly**

$$\sigma_{zz}^{\text{interference}} = 0 \quad a \leq r \leq c$$

**Equation 65 Axial interference stress in the assembly**

Using Equation 63 and Equation 64, the interference stresses (both radial and hoop) are found at each node by substituting the corresponding radial location of node in the Equation 63 and Equation 64. The interference radial and hoop stress at each node is denoted by the vectors  $[\sigma_{rr}]^{\text{interference}}$  and  $[\sigma_{\phi\phi}]^{\text{interference}}$ , respectively.

### 2.5 Net or Total Stress State in the Assembly

The total or net stress in the assembly is obtained by the sum of the thermal stresses and interference stresses.

$$[\sigma_{rr}]^{net} = [\sigma_{rr}]^{thermal} + [\sigma_{rr}]^{interference}$$

**Equation 66 Net radial stress in the assembly**

$$[\sigma_{\phi\phi}]^{net} = [\sigma_{\phi\phi}]^{thermal} + [\sigma_{\phi\phi}]^{interference}$$

**Equation 67 Net hoop stress in the assembly**

$$[\sigma_{zz}]^{net} = [\sigma_{zz}]^{thermal}$$

**Equation 68 Net axial stress in the assembly**

So far, we solved for transient stresses in a simple model of TH assembly assumed as two infinitely long cylinders with interference between them and subjected to boundary temperatures (temperature boundary conditions). This model incorporated the temperature dependent material properties (density, specific heat, thermal conductivity and thermal expansion coefficient). Since, the solution of this model cannot be found explicitly, we used numerical methods (to setup vectors, integrating and differentiating discrete data) to get the solution.

## 2.6 Effect of Nonlinearity of the Material Properties on OMCCL

After reading the entire discussion in this chapter, the reader might think why did the researcher incorporate the variation of material properties in the model? What effect does it have on his design parameter OMCCL? If the inclusion of variation of material properties in the model is not giving significantly different results in his critical crack lengths, why did he take the effort of incorporating the material properties in his model, therefore making it very complex to solve? To answer these questions, we conducted a study on critical crack lengths by the taking the material property of the cylinders as

1. Varying with temperature
2. Constant property values taken at room temperature ( $80^{\circ}F$ )
3. Constant property values taken at the low temperature ( $-100^{\circ}F$ )
4. Constant property values taken at mean temperature ( $-10^{\circ}F$ )

Temperatures of  $-100^{\circ}F$  at the inner radius ( $a = 4''$ ) of the inner cylinder and  $80^{\circ}F$  at the outer radius of the outer cylinder ( $c = 8''$ ) are chosen as boundary conditions for this study. For this study, the interference is chosen as  $0.005''$  ( $\delta$ ) and the outer radius of the inner cylinder is chosen to be  $6''$  ( $b$ ).

Figure 14 shows the critical crack lengths as a function of radius in the compound cylinder model at a particular time. The discontinuity in the graph is because the hoop stress is negative from  $r = 4.81''$  to  $r = 6''$ . From, Figure 14, at radial locations close to the inner radius, the crack lengths obtained by actual material properties are very close to the crack lengths obtained by modeling the material with low temperature properties. The reason for this is that the inner radius is maintained at constant low temperature (boundary condition). But as we go close to outer radius, the difference in crack lengths is significant. Also from the Figure 14, the crack lengths are significantly different for each of the material model chosen to study.

**Table 4 OMCCCL comparison for different material models**

Material model	OMCCCL (inches)
Actual material properties	1.6406
Room temperature properties	8.9139
Low temperature properties	1.7380
Mean temperature properties	3.9105

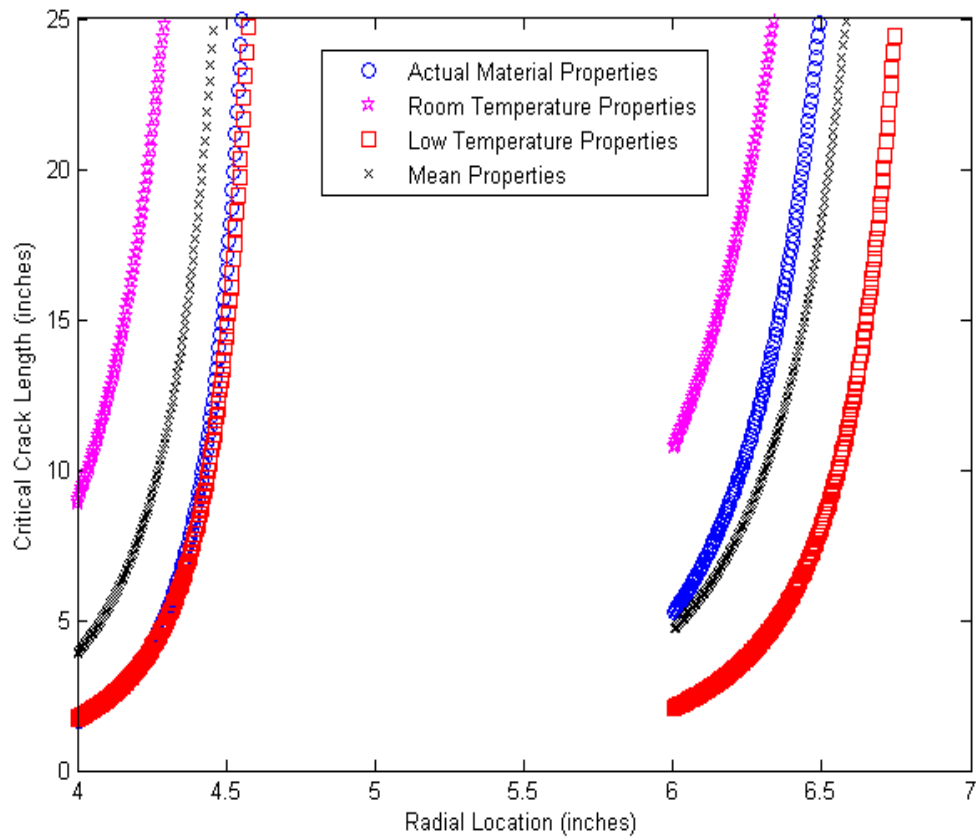


Figure 14 Critical crack lengths along the radial location of compound cylinder model

## 2.7 Finite Element Method

The geometry of the hub contains features like gussets, flanges etc. and modeling the problem with actual TH geometry makes the problem quite complex. Also previous studies [8, 9] showed that the results of simple long compound cylinders are not applicable to actual TH geometry. To solve the cracking of the TH problem with actual TH geometry, we chose the finite element approach because finite element modeling is the one of the best tools available to modern day engineers to solve complex engineering problems that otherwise cannot be solved analytically. The ANSYS [57] finite element program is chosen for conducting this study considering its nonlinear capabilities.

## 2.7.1 Finite Element Verification Model

A finite element model is built in ANSYS [57] for the long compounded cylinder geometry. The purpose of building this model is to gain confidence on finite element model so that it could be used to solve the TH assembly cooling problem. So, we start by building the same model as in the analytical part (Section 2.1) by using finite elements.

### 2.7.1.1 Geometry

Two concentric hollow cylinders are modeled in ANSYS [57] with interference between them. The inner cylinder is the trunnion and the outer cylinder is the hub (simplified form). The inner hollow cylinder is modeled with a inner radius of 4" and outer radius of 6.005". The outer hollow cylinder is modeled with inner radius of 6" and outer radius of 8". This model incorporates an interference of 0.005". The length of these cylinders is taken as 400" inches (very long) to simulate cylinders of infinite length.

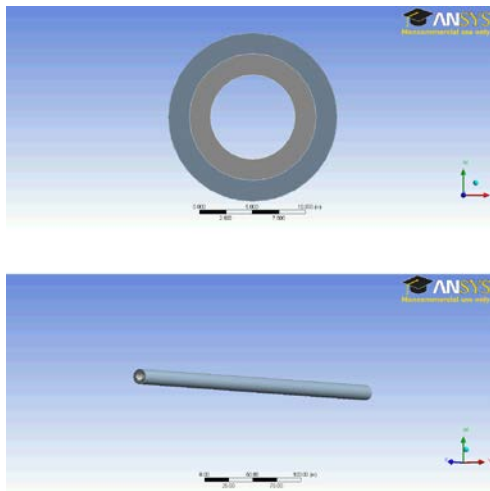


Figure 15 Geometry of the finite element verification model

### 2.7.1.2 Material Modeling

The material in the finite element model is modeled exactly as the analytical model so that when comparing the results, we are comparing the same models.

For the thermal problem, values for thermal conductivity of the material are taken from Table 2 in Section 2.2 and regressed to first order polynomial equation (Equation 13) defined by

$$k(T) = k_0(1 + \beta T)$$

**Equation 69 Regression equation of thermal conductivity**

where,  $k_0 = 0.001 \frac{BTU}{sec.in.F}$  and  $\beta = 5.8673 \frac{BTU}{sec.in.F^2}$ .

Using this regression equation, thermal conductivity of the material is defined in the finite element model as discrete data. The density of the material,  $\rho$ , is taken from Table 2. The thermal diffusivity of material is defined as a constant value at room temperature. The value of thermal diffusivity at room temperature is found by using the relation  $\alpha = \frac{k}{\rho C_p}$ , where the values of  $k$ ,  $\rho$ , and  $C_p$  are taken from Table 2 at

$T = 80^\circ F$ . From this  $\alpha$  value, the specific heat at a temperature is found by using the relation

$$C_p(T) = \frac{k(T)}{\rho(T)} \frac{1}{\alpha}$$

**Equation 70 Specific heat model formula in finite element model**

where,  $k(T)$  is the regressed thermal conductivity value at a particular temperature,  $\rho(T)$  is the density value taken from Table 2, and  $\alpha$  is the thermal diffusivity at room temperature.

For the structural problem, Young's modulus and Poisson's ratio of the material are taken from Table 3. The thermal expansion coefficient  $\alpha_x(T)$  from Table 3 is regressed to second order polynomial of the type

$$\alpha_x(T) = a_0 + a_1T + a_2T^2$$

**Equation 71 Regression equation for thermal expansion coefficient**

where

$$a_2 = -0.0000078962730396 \times 10^{-6}$$

$$a_1 = 0.00650687645 \times 10^{-6}$$

$$a_0 = 5.9966993 \times 10^{-6}$$

Note the regression constants have multiplication factor of  $10^{-6}$  because the thermal expansion coefficient data in Table 3 is given in units of  $\mu$  inch/inch.

### 2.7.1.3 Meshing

The model is meshed with SOLID 90 [78] element in the ANSYS element library for the thermal analysis and with SOLID 186 [78] for the structural analysis. The outside surface of the trunnion is meshed with TARGE 170 [78] target element in the ANSYS element library and the inner surface of the hub is modeled with CONTA 174 [78] contact element. Uniform (mapped) meshing is done and the mesh is refined at the contact and target surfaces so that contact is modeled accurately.

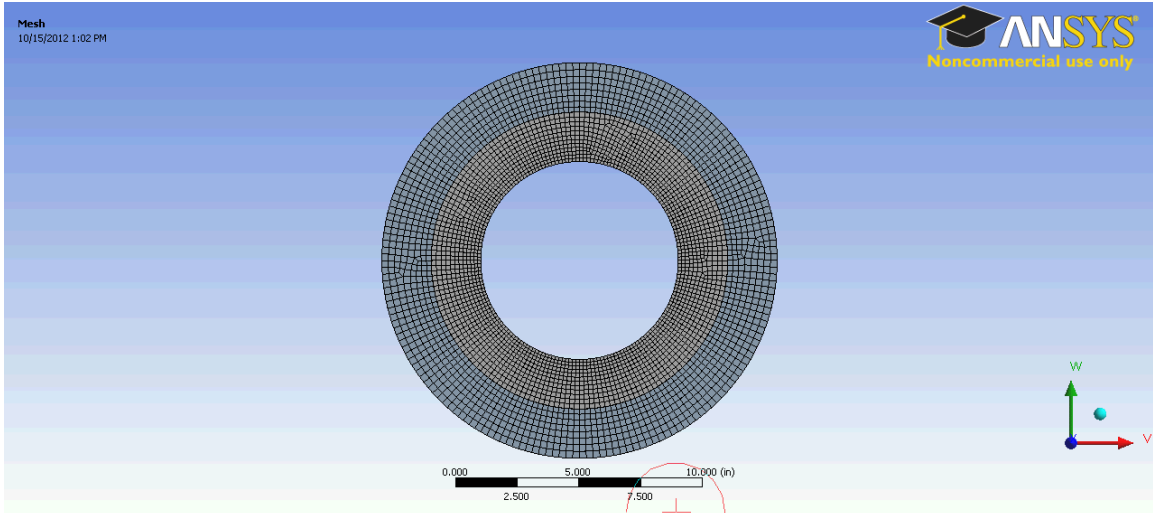


Figure 16 Finite element mesh of two concentric cylinders

#### 2.7.1.4 Loading, Boundary Conditions and Solution

For the thermal problem, a temperature of  $-100^{\circ}F$  is applied on the inner surface of the trunnion and  $80^{\circ}F$  is applied on the outer radius of the hub. The initial temperature is specified to be  $80^{\circ}F$ . The model is solved for the temperature distribution, till it reached the steady state temperature.

The results from the thermal analysis (nodal temperatures) after each time step are applied as thermal loads, and the problem is solved for stresses. The interference is already included in the model via the chosen dimensions of the trunnion during the geometric modeling. This process is repeated for all the time steps of the transient heat analysis. Only the nodal temperatures and stresses of the mid section of the model (both trunnion and hub) are written to a text file after each time step. Only the data from the mid section of the model is taken to avoid the effect of the boundary conditions imposed on the model (The model is totally constrained at three nodes at one end to avoid rigid body motion). A convergence test is performed and the mesh with a global element size of 0.4 inches and with 22 radial divisions is found to be adequate (see Appendix B, B.2).

Please note that there is surface mesh refinement done on the contact surfaces for increased accuracy of the stresses (especially interference stresses).

## 2.8 Comparison of Analytical Model and Finite Element Model

In this section, we will compare the finite element model results with the analytical model results to make sure that finite element model is accurate.

The finite element model built in Section 2.7.1 is same as the analytical model by substituting  $a = 4$ ,  $b = 6$ ,  $c = 8$ ,  $\delta = 0.005$ ,  $T_a = -100$ ,  $T_c = 80$ , and  $T_{initial} = 80$ . A MATLAB [71] program is written to calculate the analytical net stresses (thermal + interference) and a convergence testing is performed on the number of divisions ( $n$  value) chosen for the analytical solution. It is found that for a  $n$  value of 200, the solution converged and the results are within 0.05% of the values obtained from a mesh whose  $n$  value is 400 (see Appendix B, B.1). Although the program is computationally not much time consuming we chose the value of  $n = 200$ .

Using MATLAB [71] to read the data from ANSYS [57] written text files, the maximum absolute relative percentage difference between ANSYS [57] solution and analytical solution for the thermal problem is found to be less than 0.5% (Figure 17). For the structural problem, the stresses (hoop) predicted by ANSYS [57] are within 2% (Figure 18) of the analytical solution.

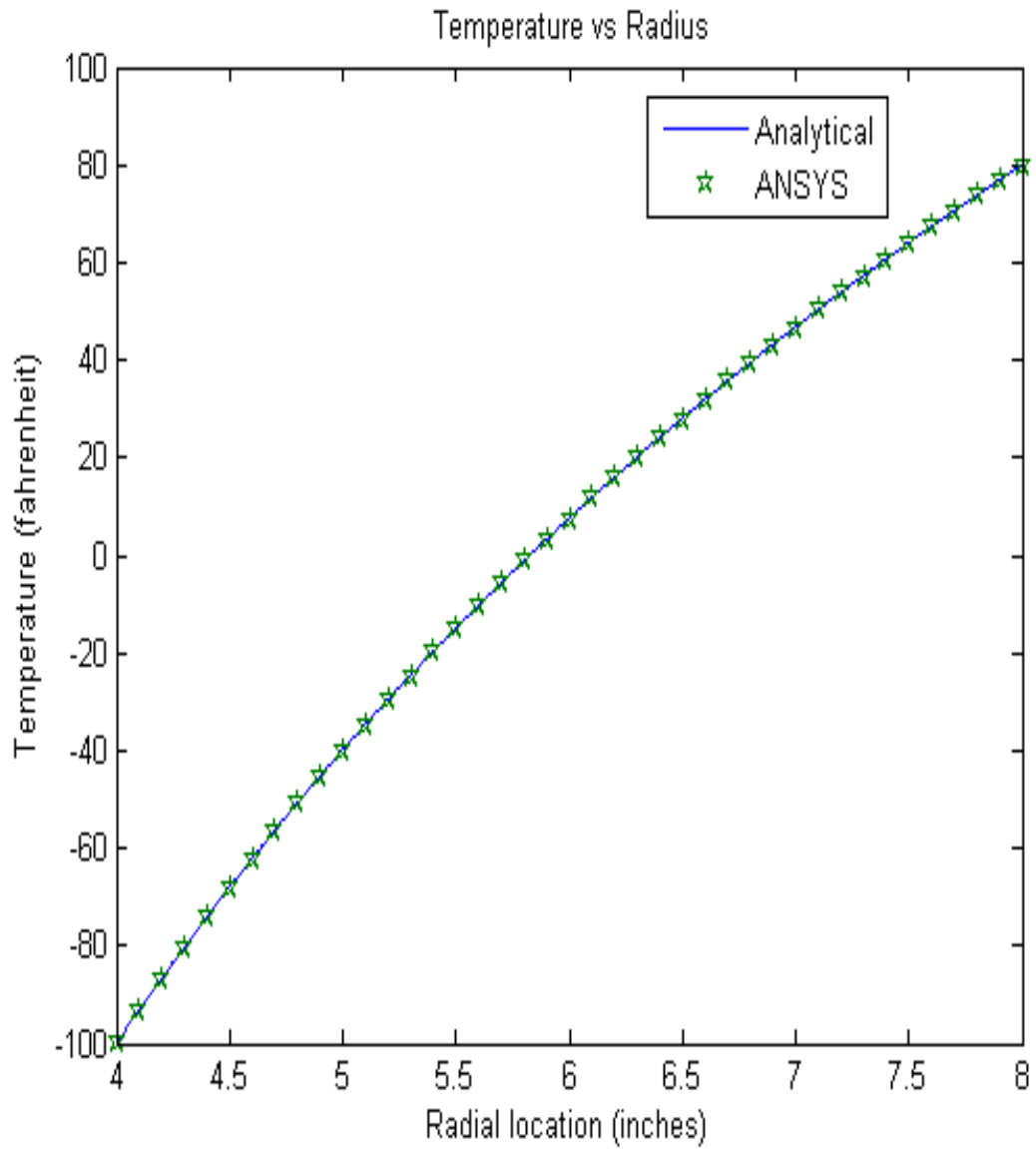
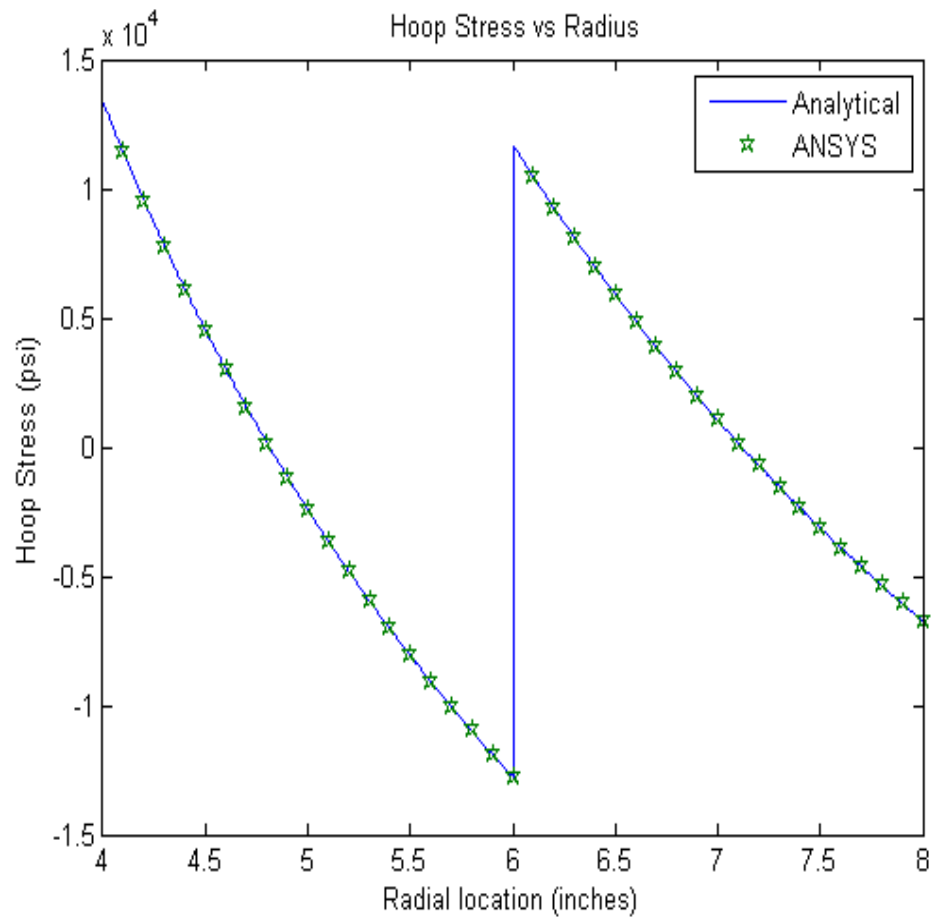
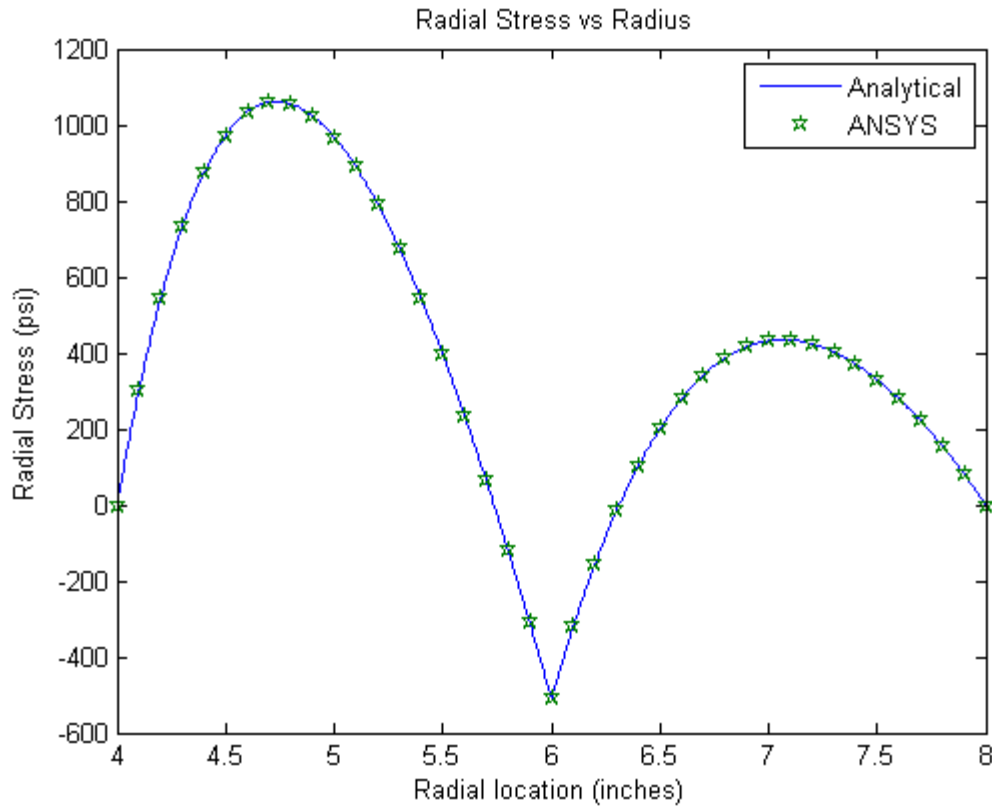


Figure 17 Comparison of ANSYS and analytical solution for temperature



**Figure 18 Comparison of ANSYS and analytical solution for hoop stresses**



**Figure 19 Comparison of ANSYS and analytical solution for radial stresses**

Though the absolute relative percentage difference between ANSYS and analytical solutions is very small, there is a small error that might have crept either in the finite element model or the analytical model or both. The following might be the reasons for this error.

1. The error that crept into the thermal problem (temperature distribution would have propagated onto the structural problem).
2. In the analytical solution for stresses, thermal expansion coefficient is modeled as a continuous 2<sup>nd</sup> order polynomial function of temperature. In finite element model thermal expansion coefficient is given as discrete data of the second order polynomial. ANSYS always does linear interpolation between two discrete data points in its calculation.

3. In analytical solution for stresses, numerical techniques were used to differentiate. Though second order accuracy formulas were used for differentiation, there might be some small error that could have crept into the analytical model.
4. As the finite element model approximated the solution with acceptable accuracy, and as the analytical modeling of the actual TH geometry with temperature dependent material properties and temperature dependent convection coefficient boundary conditions is intractable, we chose finite element method as the method of choice to study the assembly procedures.

## CHAPTER 3 ASSEMBLY PROCEDURE AP1

To find the effect of geometrical parameters like hub radial thickness to hub inner diameter ratio, radial interference in TH assembly, and the type of shrink-fitting method on the design parameter OMCCL, a complete full factorial design of experiments (DOE) [59] study is performed on AP1. I used a finite element model developed in ANSYS [57]. This study is similar to previous studies [8, 9] but this study is done with the AASHTO recommended FN3 fit [65-67] instead of FN2 fit [65-67] as recommended by FDOT [3]. We submitted this work to “Bridge Structures” journal and based on the feedback and recommendations given by the reviewers and the editor, we included an additional shrink-fitting method of heating the girder slowly and cooling the TH assembly in dry-ice/alcohol mixture in the analysis. The work in this chapter is published in the journal “Bridge Structures” titled as “Comparing Two Procedures for Assembling Steel Fulcra in Simple-Trunnion Bascule Bridges”. Only the results were used, none of the figures and tables had been reproduced in this dissertation.

### 3.1 Factors for DOE Study

The factors used in the DOE study are the following.

#### 3.1.1 Hub Radial Thickness to Hub Inner Diameter Ratio

Hub radial thickness to hub inner diameter ratio,  $\alpha$  is defined as the ratio of hub radial thickness to hub inner diameter. It is calculated as (Figure 3 and Figure 4).

$$\alpha = \frac{RHO - RTO}{2 \times RTO}$$

**Equation 72 Hub radial thickness to hub inner diameter ratio**

AASHTO recommends the value of  $\alpha$  to be 0.4 [66], while the ratios of 0.1-0.2 are used in bascule bridges in Florida, USA [3].

Values of  $\alpha$  of 0.1, 0.25 and 0.4 are used in this study. The symbol used to represent this factor in DOE study is “D”. To make the comparison easy, same symbolic notations from the previous studies [8, 9] are used to represent the factors in this study.

### 3.1.2 Shrink-Fitting Method

Five types of shrinking methods are chosen to be studied in this dissertation.

1. Cooling TH assembly in liquid nitrogen ( $-320^{\circ}F$ ).
2. Cooling TH assembly in dry-ice/alcohol mixture ( $-108^{\circ}F$ ) and then cooling in liquid nitrogen ( $-320^{\circ}F$ ).
3. Cooling TH assembly in refrigerated air ( $-32^{\circ}F$ ) and then cooling in liquid nitrogen ( $-320^{\circ}F$ ).
4. Cooling TH assembly in refrigerated air ( $-32^{\circ}F$ ) followed by cooling in dry-ice/alcohol mixture ( $-108^{\circ}F$ ) and then cooling in liquid nitrogen ( $-320^{\circ}F$ ).
5. Cooling in TH assembly in dry-ice/alcohol mixture ( $-108^{\circ}F$ ) and heating of the girder.

In shrink-fitting method 5, it is assumed that the girder is heated very slowly. Hence the critical part is assumed to be dipping TH assembly in dry-ice alcohol mixture.

The symbol used for representing this factor in this study is “X”.

### 3.1.3 TH Radial Interference

Previous works [8, 9] included the FN2 fit as an interference parameter. Since AASHTO calls for FN3 fit for fixed-trunnion bascule bridges, in this study FN3 radial interference fit is used. The extreme values of the radial interference are chosen for this study.

The symbolic notation used to represent the radial interference factor is “C”. The radial interference values chosen for the three bridges in this study are show in Table 5. Appendix C shows how the radial interferences are calculated.

**Table 5 FN3 fit radial interference values for three bridges used in this study**

FN3 fit	17th street Causeway Bascule Bridge	Christa McAuliffe Bascule Bridge	Hallandale Bascule Bridge
Low (inches)	0.003324702	0.00371097	0.004194894
High (inches)	0.00505984	0.005647698	0.006384197

All the factors and their levels used in this study are given in the Table 6. Table 6 lists all the factors, values and also the symbols used for those factors in this study.

**Table 6 All factors and levels for general factorial design**

Symbol	Factor	Levels
D	Hub radial thickness to hub inner diameter ratio, $\alpha$	0.10
		0.25
		0.40
X	Shrink-Fitting Method	1. Liquid Nitrogen
		2. Dry-Ice/Alcohol + Liquid Nitrogen
		3. Refrigerated Air + Liquid Nitrogen
		4. Refrigerated Air + Dry-Ice/Alcohol + Liquid Nitrogen
		5. Dry-Ice/Alcohol + Heating Girder
C	Radial Interference (FN3)	Lower Limit
		Upper Limit

## 3.2 Finite Element Modeling of AP1

Finite element model of AP1 is built in ANSYS [57] with actual geometry of the TH assembly components. This model is meshed with the same elements used in the finite element model built in Section 2.7.1. Also the meshing is very similar to the verification model in Section 2.7.1.3.

### 3.2.1 Building Geometry

To perform analyses on AP1 in ANSYS, the geometry has to be modeled as trunnion inside the hub (Figure 20). To simulate interference at the trunnion-hub interface, the outer diameter of the trunnion is increased by the amount of FN3 diametrical interference value.

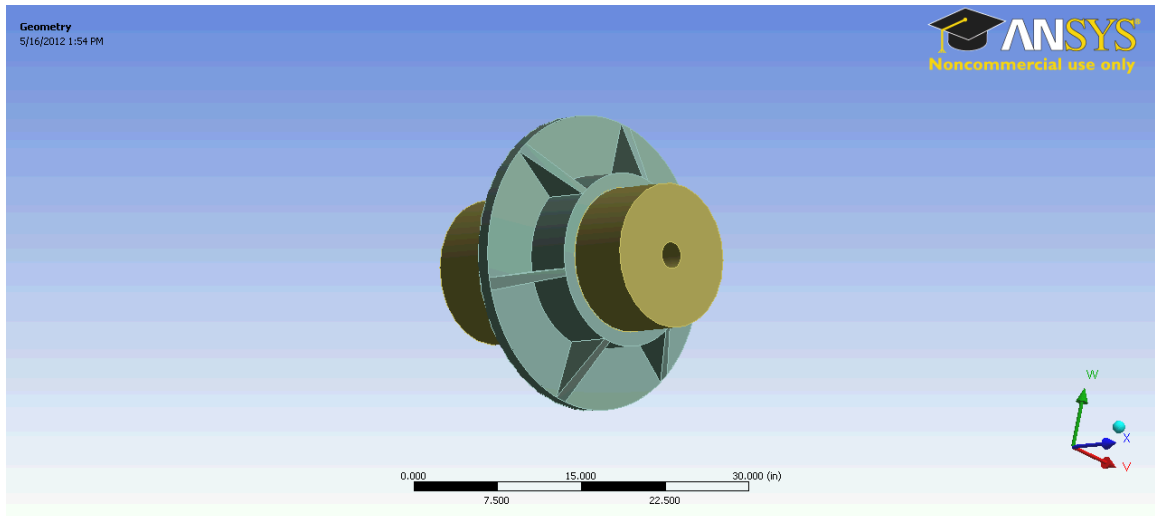


Figure 20 Trunnion-hub assembly

Due to  $1/6^{\text{th}}$  symmetric nature of the geometry and also due to the loading, the full geometric model is reduced to one sixth model (Figure 21) to save computational time.

Figure 21 shows the one sixth model of the TH assembly with interference incorporated in the geometry itself. The volume of the hub is modeled as 13 volumes instead of just one volume for meshing purposes. The one sixth model of the trunnion

are created inside the ANSYS (classical) using an APDL code, so that parametric study could be performed inside ANSYS easily.

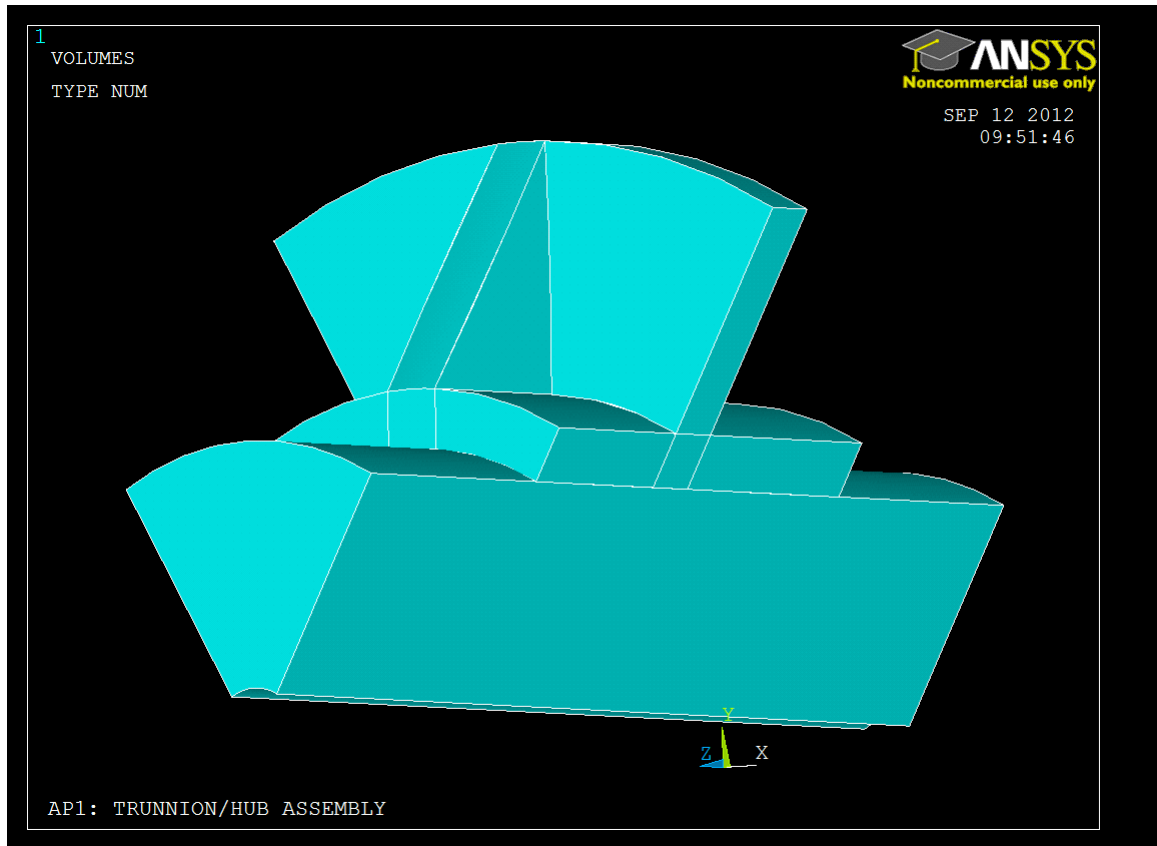


Figure 21 1/6<sup>th</sup> geometry of TH assembly

### 3.2.2 Material Properties

During the construction of Venetian Causeway bascule bridge, the trunnion got stuck inside the hub before it could be completely inserted into the hub. This failure occurred because the contractor overestimated the contraction of the trunnion by considering the thermal expansion coefficient to be a constant function of temperature and by using the room temperature values (thermal expansion coefficients of steel decreases with decrease in temperature). Hence, temperature dependence of the properties is taken into account for more accurate modeling.

### 3.2.3 Meshing

The volume of the hub is broken into 13 volumes and modeled separately in ANSYS. This modeling of the hub allowed performing a mapped meshing rather than free meshing. Mapped meshing is uniform and requires fewer elements to mesh the model. Also, mapped meshing gives more accurate results when compared to free meshing. The model is meshed in such a way that there is perfect nodal continuity (Figure 22). The elements chosen for meshing are SOLID90 [78] for the thermal problem and SOLID 186 [78] for the structural problem.

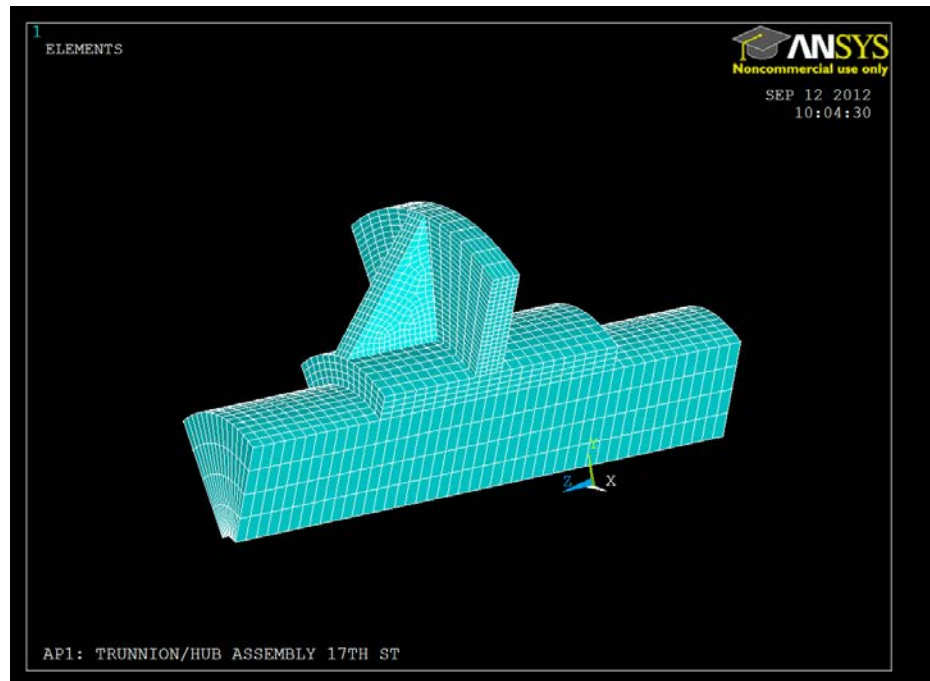


Figure 22 1/6<sup>th</sup> TH assembly meshed in ANSYS

The outer radius surface (circumferential face) of the trunnion and the inner radius surface of the hub are meshed with contact elements (CONTA 174 [78]) and target elements (TARGET 170 [78]) elements, respectively to simulate contact.

### 3.2.4 Loading and Boundary Conditions

Interference is already included in the FEM model because during the geometric modeling, the trunnion outer radius is modeled as the sum of the outer radius of the trunnion and the FN3 fit radial interference value. The boundary conditions for the structural problem is chosen as symmetric displacement conditions applied on the surfaces of the 1/6<sup>th</sup> symmetry.

For the thermal problem, convection loads are applied on the appropriate surfaces which are exposed to the cooling medium when the full model is dipped in the cooling medium. For better accuracy, the temperature dependence of convective heat transfer coefficients is incorporated in the FEM model.

### 3.2.5 Solving

A cluster machine from research computing [79] with 64GB of RAM and 16 CPU cores is used to solve the model. FEM model is solved with thermal convective loads, and the temperature at each node after each minute of cooling is obtained. Now these temperatures are applied as thermal loads and solved to obtain displacements and stresses. This process is repeated for each minute of transient analysis till the TH assembly reached the steady-state temperature. The output of the FEM solver (nodal displacements, stresses, temperatures) after each minute of cooling is written to a separate text file.

A MATLAB [71] code is developed to read the data from the text file to calculate the critical crack length and stress ratio value at each node. The minimum values of critical crack length and stress ratio obtained are taken as critical crack length and stress ratio value of the assembly at that time of cooling. This process is repeated throughout

the cooling process (till the steady-state temperature) and the minimum value of critical crack length and stress ratio of all the time steps is taken as the OMCCCL value and OMSR value, respectively.

### **3.3 AP1 Results: OMSR**

The OMSR values found for all the runs in AP1 for all the bridges are greater than one. From these results, we can conclude that in AP1, the bridge will not fail by yielding. Also, we found no record of contractors reporting the failure of TH assembly by yielding of the material. So no further study is done on OMSR.

### **3.4 AP1 Results: OMCCCL**

In all the shrink-fitting methods involving cooling TH assembly in liquid nitrogen, the critical part is dipping the TH assembly in liquid nitrogen. This result verifies with the cracking of the hub that was observed in the field during the Christa McAuliffe bridge construction [3]. Hence, in-depth DOE study is performed on OMCCCL values to address the cracking of the hub.

The factors for the DOE study are mentioned in Section 3.1. A total of 90 models are solved for all the bridges (3 bridges  $\times$  3  $\alpha$  values  $\times$  5 cooling methods  $\times$  2 interference value) to perform a general factorial DOE study for AP1. All these models are solved sequentially by developing a code in ANSYS Parametric Design Language (APDL) [80]. The names of bridges are not used as a factor because the name is not quantifiable and is not a categorical variable. OMCCCL values obtained for all the combinations of the factors for three bridges are noted and DOE analysis is carried out using Minitab [81].

### 3.4.1 Percentage Contribution of the Factors

For AP1, Table 7 shows the contribution of each factor to OMCCCL in AP1. The shrink-fitting method (Factor X) has the largest contribution of 51% to 75%. The contribution of shrink-fitting method increases with the increase in bridge size. The interaction between hub radial thickness to hub inner diameter ratio,  $\alpha$  (Factor D) and shrink-fitting method (Factor D) has a contribution of 15% to 22%. The contribution of interaction between the factors D and X decreases with the increase in bridge size. Hub radial thickness to hub inner diameter ratio,  $\alpha$  has a contribution of 7% to 12%. From, the above results, it is clear that the largest contributing factor is the shrink-fitting method.

**Table 7 Contribution of factor to OMCCCL in AP1**

Parameter	Contribution to OMCCCL (%)		
	17th Street Causeway Bascule Bridge	Christa McAuliffe Bascule Bridge	Hallandale Bascule Bridge
X	51	69.4	75.1
D	11.9	6.88	6.18
C	6.02	5.08	2.45
XD	22.1	13.8	14.6
XC	5.50	4.27	1.27
DC	0.927	0.0859	0.102
XDC	2.48	0.487	0.268

### 3.4.2 Sensitivity Analyses

A sensitivity analysis is performed to study the effect of these factors on the OMCCCL values.

#### 3.4.2.1 Shrink-Fitting Method

In Figure 23, OMCCCL is plotted as a function of shrink-fitting method. Table 8 gives the OMCCCL values for all the three bridges used in this study. Stepped cooling methods like shrink-fitting method 2, which involves two steps, that is, dipping TH

assembly in dry-ice/alcohol mixture and then dipping in liquid nitrogen, increased the OMCCCL values by as much as 212% for small bridge (17<sup>th</sup> street Causeway), 328% for medium bridge (Christa McAuliffe), 466% for large bridge (Hallandale) when compared to conventional single staged cooling method like shrink-fitting method 1, which involves single step of dipping TH assembly in liquid nitrogen. This result is consistent with the previous works [8, 9].

From Figure 23 and Table 8, stepped cooling methods like shrink-fitting method 3, which involves two steps, that is, dipping TH assembly in refrigerated air and then dipping in liquid nitrogen, increased the OMCCCL values by as much as 95% for small bridge (17<sup>th</sup> street Causeway), 125% for medium bridge (Christa McAuliffe), 151% for large bridge (Hallandale) when compared to conventional single-staged cooling method like shrink-fitting method 1, which involves the single step of dipping TH assembly in liquid nitrogen. Although, shrink-fitting method 2 and shrink-fitting method 3 are both multi-stage cooling methods involving two steps, shrink-fitting method 2 gives higher OMCCCL values than shrink-fitting method 3. This result agrees with previous work of Nguyen et al. [8] and Snyder [9] that in actual THG geometry, staged shrink-fitting method of dipping in liquid dry-ice/alcohol mixture and then dipping in liquid nitrogen gives higher OMCCCL values than the staged shrink-fitting method of cooling in refrigerated air and then dipping in liquid nitrogen. Like the previous works [8, 9], this result is in contrast with the results of the previous work conducted on long compounded cylinders [5]. This result once again proves that, the results obtained by conducting a study on simple compound cylinders are not applicable to actual THG geometry.

Shrink-fitting method 4 is a three-staged cooling method (first in refrigerated air, second in dry ice alcohol and lastly in liquid nitrogen) whereas shrink-fitting method 2 is a two staged cooling method, but both the methods yielded the same OMCCCL values (Figure 23 and Table 8). This result tells us that if a contractor would like to implement stepped cooling to reduce the danger of hub cracking during assembly, it is recommended for him/her to adopt a two-staged cooling procedure of dipping the TH assembly in dry-ice/alcohol mixture followed by dipping in liquid nitrogen. Implementing three-staged stepped cooling will not enhance safety but will increase the amount of money, time and work for the contractor.

Stepped cooling methods like shrink-fitting method 5 which involves slow heating of the girder and cooling of the TH assembly in dry-ice/alcohol mixture increased the OMCCCL values by as much as 265% for a small bridge (17<sup>th</sup> street Causeway), 384% for medium bridge (Christa McAuliffe), 642% for large bridge (Hallandale) when compared to conventional single staged cooling method like shrink-fitting method 1.

From the above results and Figure 23, it is clear that shrink-fitting method 5 gives the highest OMCCCL values for all bridges and one may believe that adopting shrink-fitting method 5 rather than shrink-fitting method 1 would give higher OMCCCL values. But adopting shrink-fitting method 5 at the site of construction can be quite tedious and cumbersome because heating a large steel structure like the girder slowly with heating coils is very complicated, costly and time consuming. The next best choice of shrink-fitting method is shrink-fitting method 2 and it is relatively easy to implement. To determine if it is worth to adopt complex shrink-fitting method 5 rather than easy shrink-

fitting method 2, percentage increase in OMCCCL values had to be found by adopting shrink-fitting method 5 over shrink-fitting method 2.

Shrink-fitting method 5 increases the OMCCCL values by only 19% for a small bridge, 13% for medium bridge and 31% for large bridge over shrink-fitting method 2. From this result, we can conclude that since the increase in OMCCCL value is not very high, the contractor is better off choosing shrink-fitting method 2.

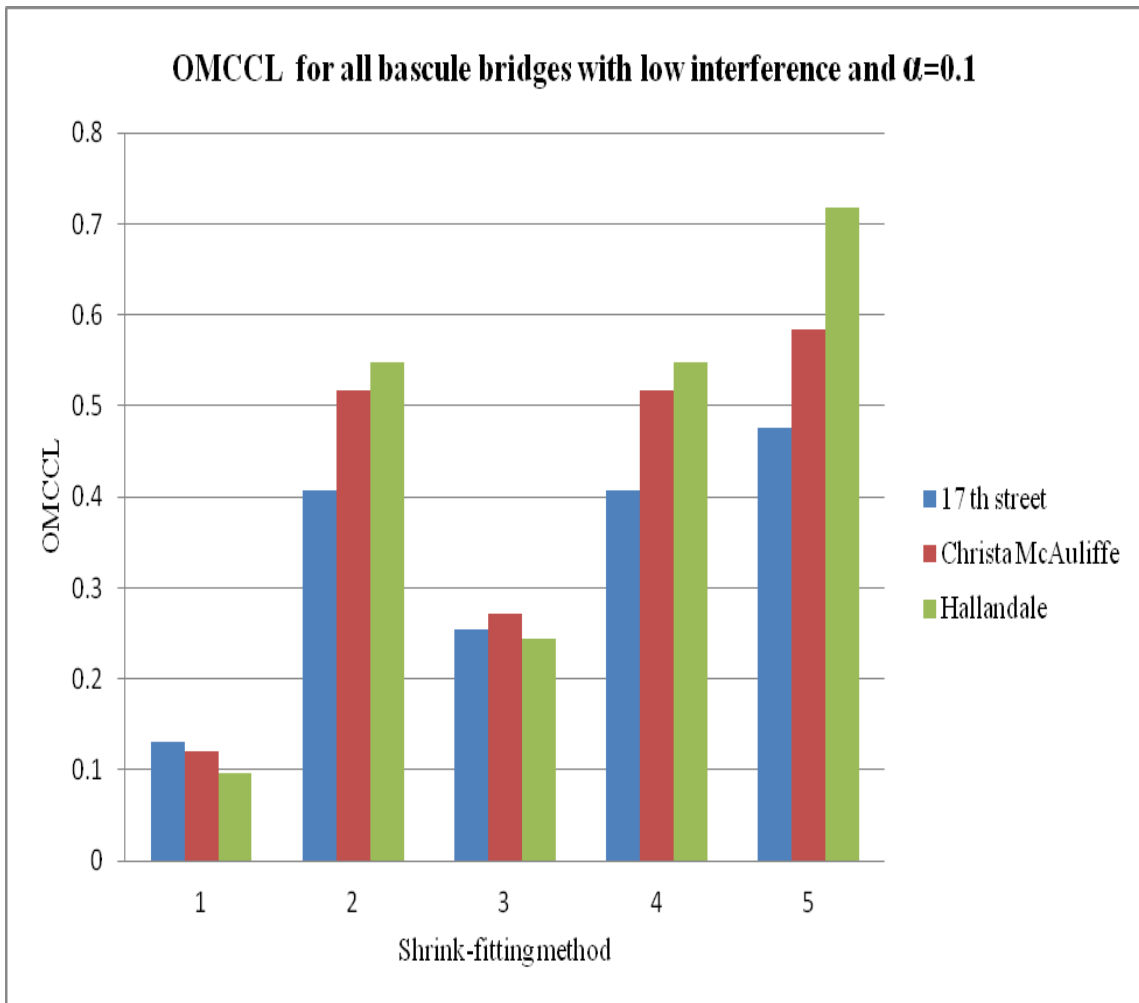


Figure 23 Variation of OMCCCL with shrink-fitting method for three bridges for low interference value and  $\alpha=0.1$

**Table 8 OMCCCL values for different shrink-fitting methods for three bridges for low interference value and alpha=0.1**

Cooling Method	OMCCCL value (inches)		
	17 <sup>th</sup> Street Causeway Bascule Bridge	Christa McAuliffe Bascule Bridge	Hallandale Bascule Bridge
Shrink-fitting Method 1	0.130567	0.120888	0.0968193
Shrink-fitting Method 2	0.407968	0.51715	0.548033
Shrink-fitting Method 3	0.254862	0.272345	0.243558
Shrink-fitting Method 4	0.407968	0.51715	0.548033
Shrink-fitting Method 5	0.476451	0.5845	0.718071

### 3.4.2.2 Hub Radial Thickness to Hub Inner Diameter Ratio

Figure 24, Figure 25, and Table 9 gives the variation of OMCCCL with hub radial thickness to hub inner diameter ratio,  $\alpha$ . For all the bridges, for shrink-fitting methods involving dipping TH assembly in liquid nitrogen (shrink-fitting methods 1, 2, 3, and 4), the increase in OMCCCL is only 3% for the low interference case and only 14% for the high interference case. Although one may intuitively think that increasing the radial thickness (higher value of  $\alpha$ ) would increase the OMCCCL values significantly, from the above results it is found that, it is not so.

**Table 9 OMCCCL values for different alpha values for all the bridges for both high and low interference case for shrink-fitting method 1**

$\alpha$ - value	Interference Low			Interference High		
	17 <sup>th</sup> Street Causeway Bascule Bridge	Christa McAuliffe Bascule Bridge	Hallandale Bascule Bridge	17 <sup>th</sup> Street Causeway Bascule Bridge	Christa McAuliffe Bascule Bridge	Hallandale Bascule Bridge
0.1	0.130567	0.120888	0.096819	0.104304	0.098783	0.083787
0.25	0.129778	0.119800	0.094301	0.109364	0.105106	0.085925
0.40	0.128704	0.123481	0.100089	0.114335	0.112614	0.09376

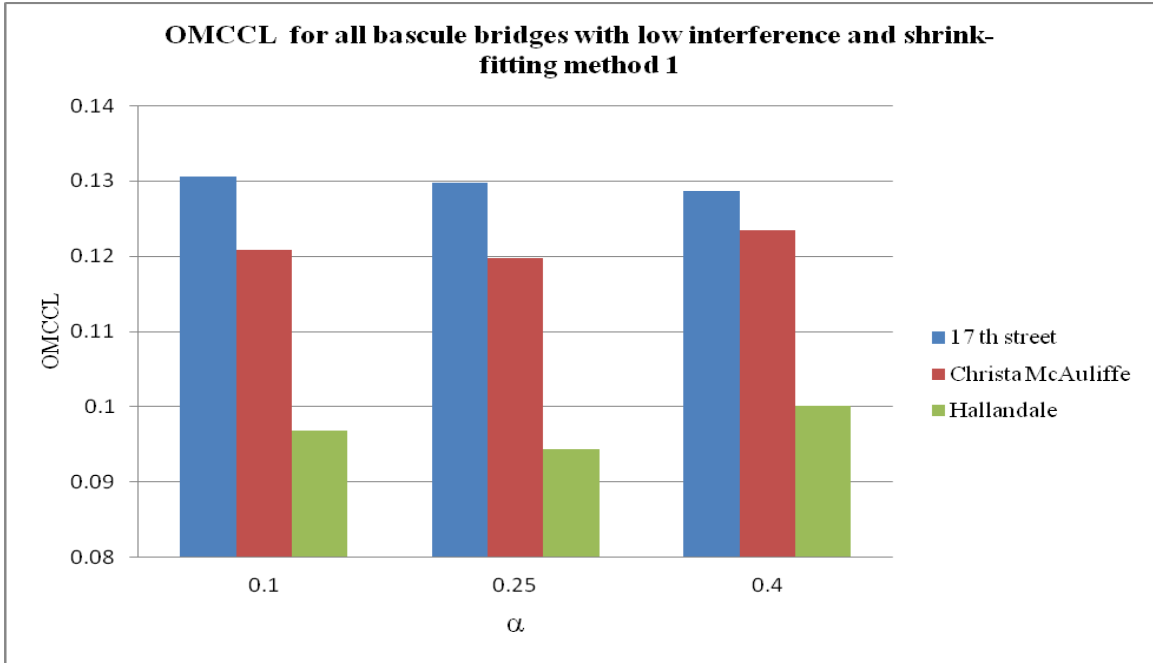


Figure 24 OMCCL as a function of alpha for low interference and shrink-fitting method 1

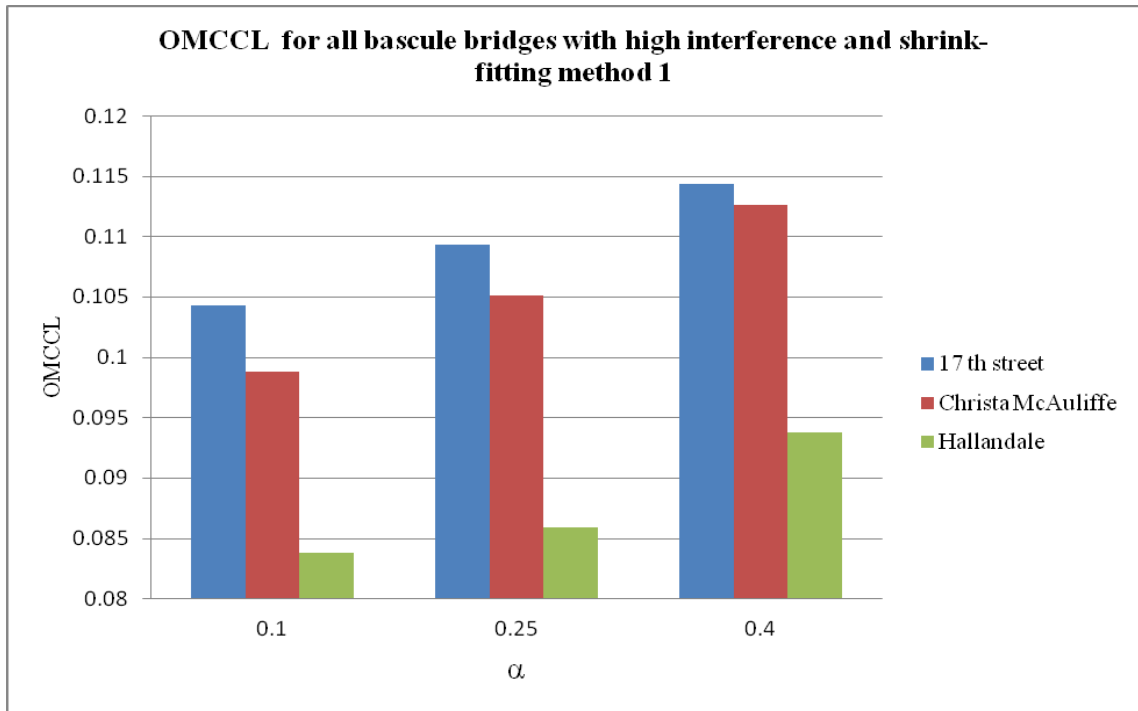


Figure 25 OMCCL as a function of alpha for high interference and shrink-fitting method 1

In contrast, for shrink-fitting method 5 which did not involve dipping of TH assembly in liquid nitrogen, OMCCL values increase with hub radial thickness by as

much as 386% for small bridge, 448% for the medium bridge, and 178% for the large bridge (Figure 26, Figure 27, and Table 10). For the small and medium bridges, the OMCCCL values increase with the radial thickness of the hub. For the large bridge, the OMCCCL values increase with the increase in radial thickness of the hub up to a certain value and then decreases.

**Table 10 OMCCCL values for different alpha values for all the bridges for both high and low interference case for shrink-fitting method 5**

$\alpha$ - value	Interference Low			Interference High		
	17 <sup>th</sup> Street Causeway Bascule Bridge	Christa Mc Auliffe Bascule Bridge	Hallandale Bascule Bridge	17 <sup>th</sup> Street Causeway Bascule Bridge	Christa Mc Auliffe Bascule Bridge	Hallandale Bascule Bridge
0.1	0.47645	0.5845	0.718071	0.285488	0.326135	0.491705
0.25	1.31524	1.77331	1.90052	0.717612	1.04547	1.43898
0.40	2.31918	2.17744	1.5552	1.24758	1.78832	1.36837

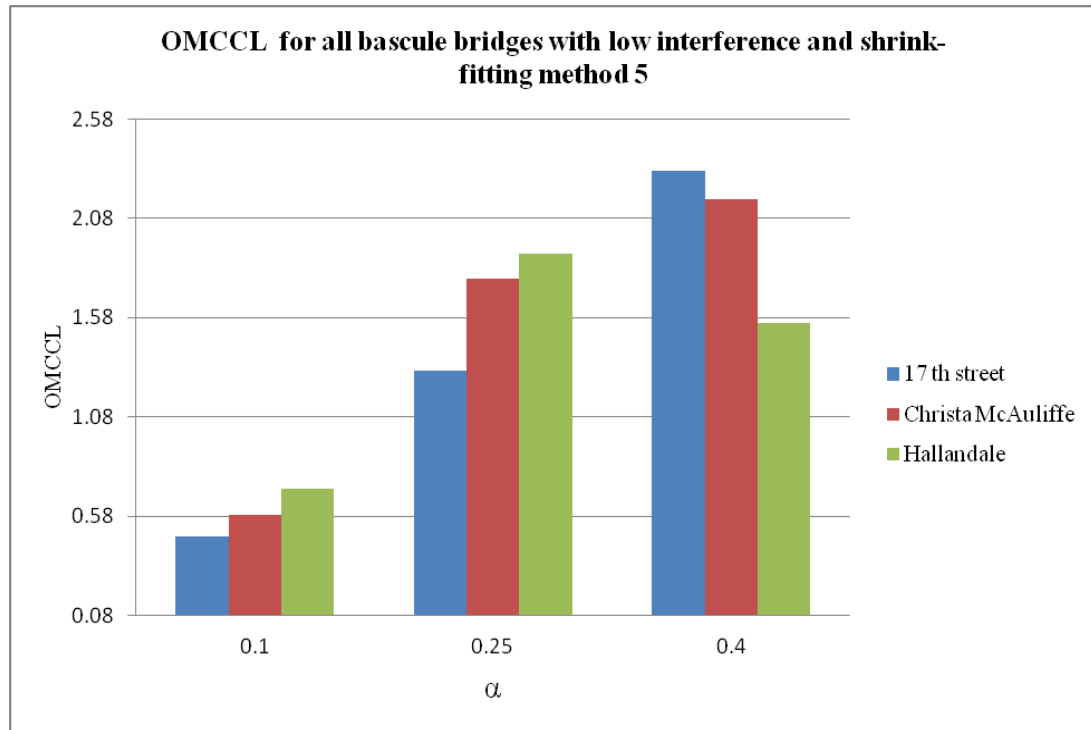


**Figure 26 OMCCCL as a function of alpha for low interference and shrink-fitting method 5**

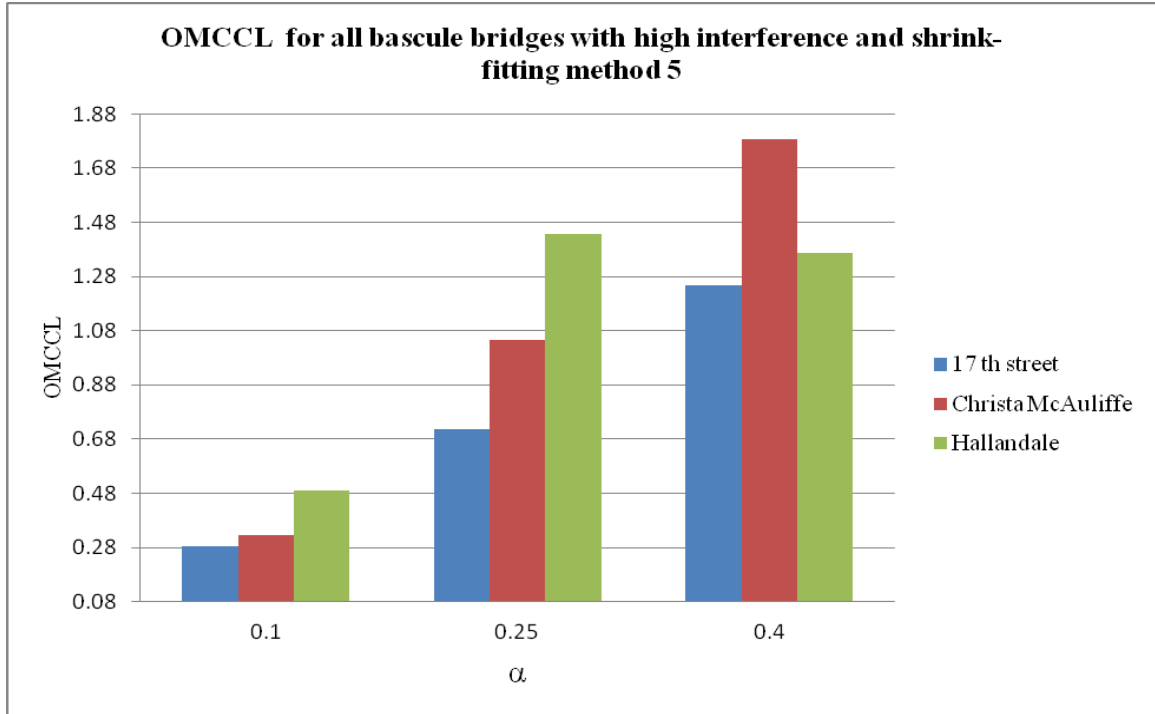


Figure 27 OMCCL as a function of alpha for high interference and shrink-fitting method 5

### 3.4.2.3 Radial Interference

Figure 28 gives the variation of OMCCL as function of interference for a radial thickness to hub inner diameter ratio,  $\alpha$  of 0.4 and shrink-fitting method 2. The increase in interference decreases the OMCCL value by 39% for small bridge, 35% for medium bridge, and 29% for large bridge. As the bridge size increases, the effect of interference on OMCCL value decreases.

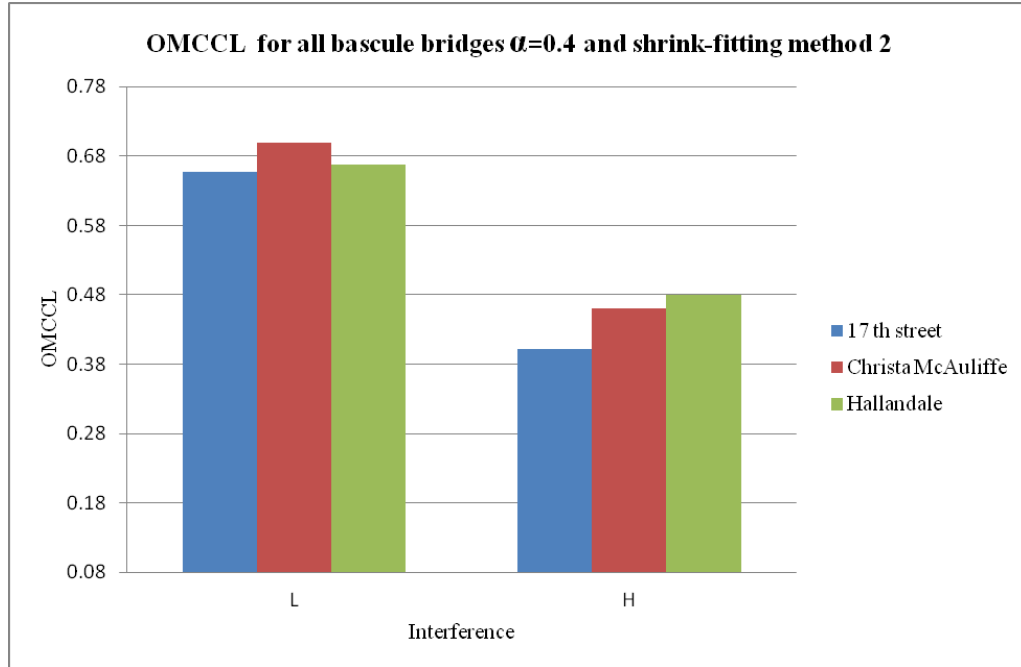


Figure 28 OMCCL as a function of interference for shrink-fitting method 2

### 3.5 Conclusions of API

1. Shrink-fitting method (Factor X) is the largest contribution factor to OMCCL, ranging from 51% to 75%, depending on the size of the bridge.
2. Shrink-fitting method 2, dipping TH assembly in dry-ice/alcohol mixture followed by dipping in liquid nitrogen increases the OMCCL value by as much as 212% for a small bridge, 328% for medium bridge and 466% for a large bridge.
3. Though shrink-fitting method 5 gives higher OMCCL values than shrink-fitting method 2, it is easier to implement shrink-fitting method 2 as slow heating of the girder is a time consuming process.
4. If the TH assembly is to be dipped in liquid nitrogen, increasing the hub radial thickness does not increase the safety of the assembly. However, if the TH assembly is to be cooled only in dry-ice/alcohol mixture (shrink-

fitting method 5), increasing the hub radial thickness increases the OMCCCL values significantly. The increase is up to 386% in small bridges, 448% in medium bridges, and 178% in large bridges.

## CHAPTER 4 ASSEMBLY PROCEDURE AP2

It is very important to conduct a very similar DOE study on AP2, as AP2 is also a commonly used assembly procedure in North America. The results are also compared to the DOE results of AP1.

Similar to AP1, the DOE study is performed on AP2 by using a finite element model developed in ANSYS. The output parameters for the study are OMCCCL and OMSR values. This work is similar to previous study [9] but in this dissertation, we consider AASHTO recommended FN3 fits for interferences and also include an additional shrink-fitting method of heating the girder slowly and cooling the hub in dry-ice/alcohol mixture. The work in this chapter is published in the journal “Bridge Structures” titled as “Comparing Two Procedures for Assembling Steel Fulcra in Simple-Trunnion Bascule Bridges”. Only the results were used, none of the figures and tables had been reproduced in this dissertation.

### 4.1 Factors for DOE Study

The same factors used in the DOE study of AP1 (Section 3.1) are used as the factors in AP2. However, in AP2, the factor TH radial interference (factor C) is not a factor because the critical step of AP2 is cooling of the hub (step 1 of AP2).

### 4.2 Finite Element Modeling of AP2

ANSYS finite element program is used to build the model.

### 4.2.1 Building Geometry

From previous works [2, 9], cooling the hub (Step 1) is the critical part of the assembly procedure. So to model AP2, only hub component needs to be modeled. To verify previous works, and also to be certain, in this work, both the hub and trunnion models are built separately and the analysis is carried out on both the components.

Due to  $1/6^{\text{th}}$  symmetric nature of the geometry and also due to the loading, the full geometric model is reduced to one sixth model (Figure 29) to save computational time.

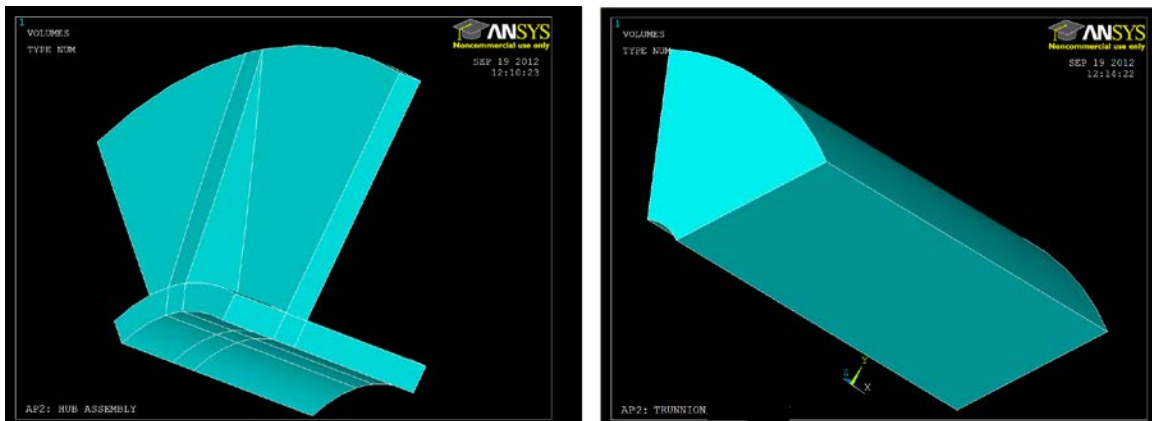


Figure 29 AP2: Hub and trunnion geometry

### 4.2.2 Material Properties

Like in AP1, temperature dependence of the properties is taken into account for better accurate modeling in AP2.

### 4.2.3 Meshing

The models of trunnion and hub are meshed separately. In AP2, similar meshing scheme followed in AP1 is used. That is, the volume of the hub is broken into 13 volumes and modeled separately in ANSYS for performing a mapped meshing. Figure 30 shows the finite element mesh of hub and trunnion models used in AP2.

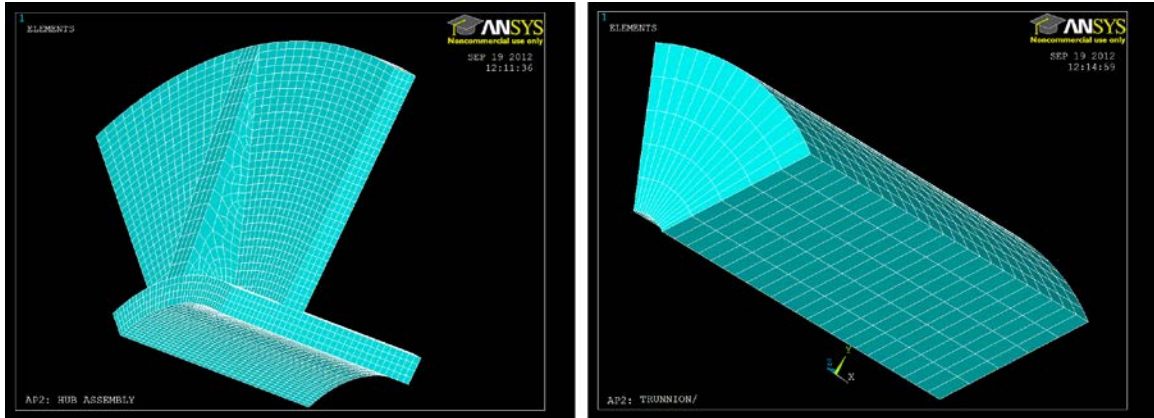


Figure 30 AP2: Meshed models of hub and trunnion

#### 4.2.4 Loading and Boundary Conditions

For both trunnion and hub models, the boundary conditions for the structural problem is chosen as symmetric displacement conditions applied on the surfaces of  $1/6^{\text{th}}$  symmetry.

For the thermal problem, convection loads are applied on the appropriate surfaces which are exposed to cooling medium when the full model is dipped in cooling medium. For better accuracy, the temperature dependence of convective heat transfer coefficients is incorporated in the finite element model.

#### 4.2.5 Solving

Both the hub and the trunnion models are solved separately with thermal convective loads. The temperature at each node after each minute of cooling is obtained. Now these temperatures are applied as thermal loads and solved to obtain displacements and stresses. This process is repeated for each minute of transient analysis till the models reach the steady state temperature. The output of the finite element (ANSYS [57]) solver (nodal displacements, stresses, temperatures) after each minute of cooling is written to a separate text file.

Using the similar MATLAB [71] code developed for AP1, the data from the text file is read to calculate the OMCCCL and OMSR values in both the hub and trunnion components.

### **4.3 AP2 Results: OMSR**

The OMSR values found for all the runs in AP2 in both the trunnion and the hub components is greater than one for all the bridges. From these results, we can conclude that similar to AP1, in AP2, failure will not occur due to yielding of the material. Hence, no further study is carried out on OMSR values.

### **4.4 AP2 Results: OMCCCL**

In AP2, an assembled part is never subjected to cryogenic temperatures. In fact, the interference stresses at the hub-girder interface caused in Step 2 (Figure 7 and Section 1.9.1) provide a compressive hoop stress to the trunnion-hub interface as it warms up in Step 4 in AP2 (Figure 7 and Section 1.9.1). This compressive hoop stress negates some of the tensile hoop stresses produced by the trunnion as it warms back up to the ambient temperature.

In AP2, it is found that the critical part is dipping the hub in the cooling medium. That is, the OMCCCL values are obtained when the hub is dipped in cooling medium. This result concurs with Snyder's work [9]. In all the shrink-fitting methods involving cooling hub in liquid nitrogen (shrink-fitting methods 1, 2, 3, and 4), the critical part is dipping the hub in liquid nitrogen. In shrink-fitting method 5, the girder is assumed to be heated slowly and hence the critical step is dipping the hub component in dry-ice/alcohol mixture.

A DOE [59] study is performed on OMCCCL with factors mentioned in Section 3.1 with an exception that in this study, radial interference (Factor C) is not a factor. A total of 45 models are solved for all the bridges (3 bridges  $\times$  3  $\alpha$  values  $\times$  5 cooling methods) to perform a general factorial design DOE [59] study for AP2. All these models are solved sequentially by developing a code in ANSYS Parametric Design Language (APDL) [80].

#### 4.4.1 Percentage Contribution of the Factors

Table 11 shows the contribution of each factor to OMCCCL in AP2. The shrink-fitting method (factor X) has the largest contribution of 68% to 73%. Unlike in AP1, in AP2, the contribution of shrink-fitting method does not necessarily increase with the increase in bridge size. The interaction between hub radial thickness to hub inner diameter ratio,  $\alpha$  (Factor D) and shrink-fitting method (Factor D) has a contribution of 18% to 21%. Hub radial thickness to hub inner diameter ratio  $\alpha$  has a contribution of 9% for all the bridges. From the above results, it is clear that the shrink-fitting method has the largest contribution (about 70%) to OMCCCL values in AP2.

**Table 11 Contribution of factors to OMCCCL in AP2**

Parameter	Contribution to OMCCCL (%)		
	17 <sup>th</sup> Street Causeway Bascule Bridge	Christa McAuliffe Bascule Bridge	Hallandale Bascule Bridge
X	73.1	68.4	70.8
D	8.43	9.41	8.33
XD	18.5	22.2	20.9

#### 4.4.2 Sensitivity Analyses

A sensitivity analysis is performed to study the effect of these factors on the OMCCCL values.

#### 4.4.2.1 Shrink-Fitting Method

In Figure 31, OMCCCL is plotted as a function of shrink-fitting method while Table 12 gives the OMCCCL values for all the three bridges used in this study. Stepped cooling methods like shrink-fitting method 2, which involves two steps, that is, dipping hub in dry-ice/alcohol mixture and then dipping in liquid nitrogen, increased the OMCCCL values by as much as 728% for small bridge (17<sup>th</sup> street Causeway), 771% for medium bridge (Christa McAuliffe), 866% for large bridge (Hallandale) when compared to conventional shrink-fitting method 1, which involves the single step of dipping hub in liquid nitrogen. This result is consistent with previous works [9].

From Figure 31 and Table 12, stepped cooling methods like shrink-fitting method 3, which involves two steps, that is, dipping hub assembly in refrigerated air and then dipping in liquid nitrogen, increased the OMCCCL values by as much as 207% for small bridge (17<sup>th</sup> street Causeway), 195% for medium bridge (Christa McAuliffe), and 197% for large bridge (Hallandale) when compared to conventional single staged cooling method like shrink-fitting method 1, which involves single step of dipping the hub in liquid nitrogen. Although, shrink-fitting method 2 and shrink-fitting method 3 are both multi-stage cooling methods involving two steps, shrink-fitting method 2 gives higher OMCCCL values than shrink-fitting method 3.

Shrink-fitting method 4 is a three-staged cooling method (first in refrigerated air then in dry ice alcohol and then in liquid nitrogen) where as shrink-fitting method 2 is a two staged cooling method, but both the methods yielded the same OMCCCL values (Figure 31 and Table 12). This result tells us that if a contractor would like to implement AP2 with stepped cooling to reduce the danger of hub cracking during the assembly, it is

recommended to adopt a two-staged cooling procedure of dipping the hub in dry-ice/alcohol mixture followed by dipping in liquid nitrogen. Implementing three-staged stepped cooling will not increase safety but will increase the amount of money, time and work for the contractor.

Stepped cooling methods like shrink-fitting method 5 which involves slow heating of the girder and cooling of the hub in dry-ice/alcohol mixture increased the OMCCCL values by as much as 4618% for a small bridge (17<sup>th</sup> street Causeway), 4511% for medium bridge (Christa McAuliffe), 4608% for large bridge (Hallandale) when compared to conventional single-staged cooling method like shrink-fitting method 1.

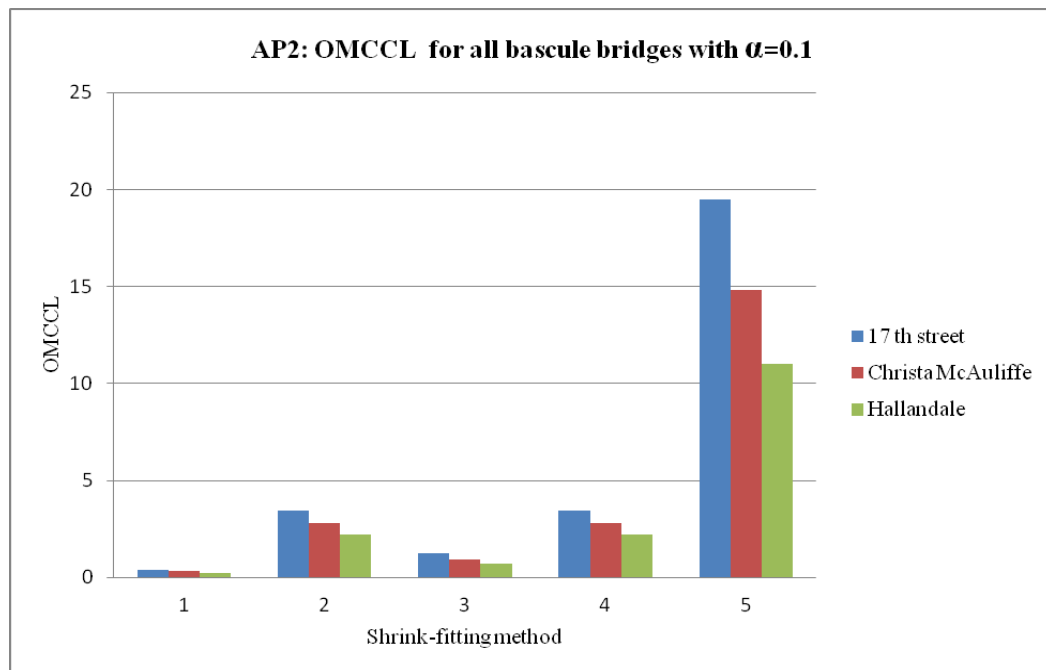


Figure 31 Variation of OMCCCL in AP2 with shrink-fitting method for three bridges for alpha=0.1

**Table 12 OMCCCL values in AP2 for different shrink-fitting methods for three bridges for alpha=0.1**

Cooling Method	OMCCCL value (inches)		
	17 <sup>th</sup> Street Causeway Bascule Bridge	Christa McAuliffe Bascule Bridge	Hallandale Bascule Bridge
Shrink-fitting Method 1	0.41311	0.321192	0.233909
Shrink-fitting Method 2	3.42358	2.79805	2.23033
Shrink-fitting Method 3	1.27217	0.948367	0.695341
Shrink-fitting Method 4	3.42358	2.80035	2.23033
Shrink-fitting Method 5	19.4937	14.813	11.0136

From the above results, and from Figure 31 and Table 12, it is clear that shrink-fitting method 5 is the best choice of shrink-fitting. However, shrink-fitting method 5 assumes that the girder is heated slowly. To confidently say that shrink-fitting method 5 is a good choice of shrink-fitting method, further study had to be done on how to heat the girder relatively quickly (not too slowly) so that the heating of the girder does not become a critical step.

#### **4.4.2.2 Hub Radial Thickness to Hub Inner Diameter Ratio**

Figure 32 and Table 13 gives the variation of OMCCCL with hub radial thickness to hub inner diameter ratio,  $\alpha$  for shrink-fitting method 1. The smaller bridge gives higher OMCCCL values when compared to the larger bridge. Although one may intuitively think that increasing the radial thickness (higher value of  $\alpha$ ) would increase the OMCCCL values significantly, surprisingly in AP2, for all the bridges, for shrink-fitting methods involving dipping hub in liquid nitrogen (shrink-fitting methods 1, 2, 3, and 4), the OMCCCL values decrease with increase in hub radial thickness. For the small bridge, the

OMCCL values decrease up to 53% with the increase in hub radial thickness. For medium bridge, the OMCCL values decrease up to 42% with increase in hub radial thickness, and in large bridge, the OMCCL values decrease up to 34%. Similar trend is observed in all other cooling methods which involved cooling the hub in liquid nitrogen.

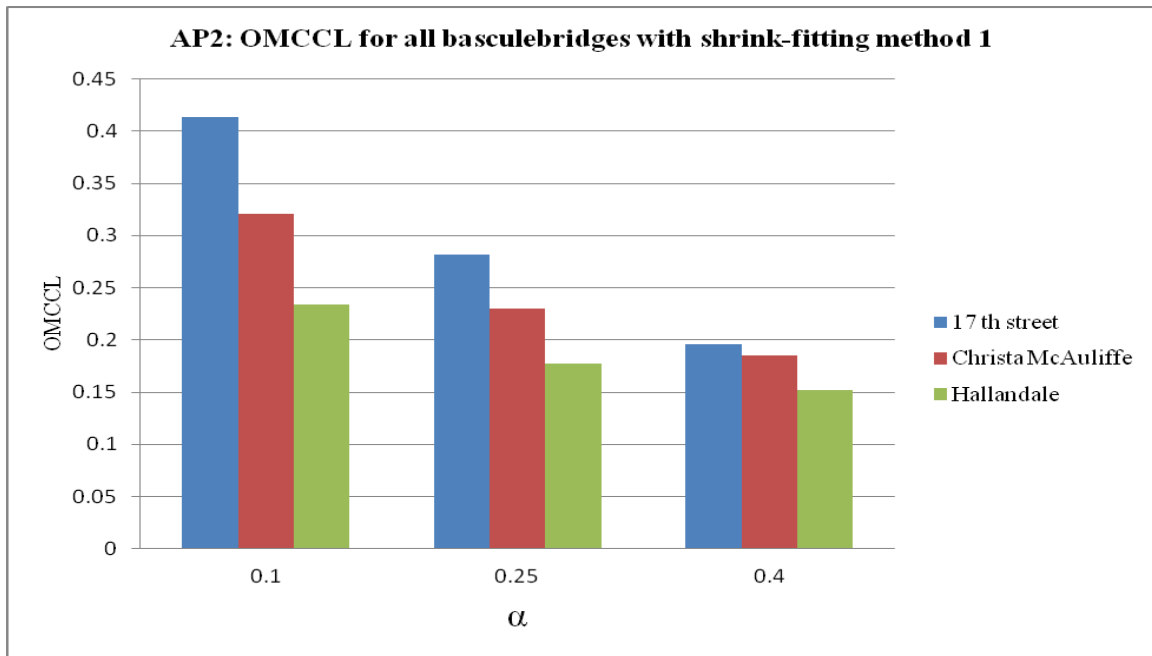


Figure 32 OMCCL as a function of alpha in AP2 for shrink-fitting method 1

Table 13 OMCCL values for different alpha values for all the bridges in AP2 with shrink-fitting method 1

$\alpha$ - value	OMCCL (inches)		
	17 <sup>th</sup> Street Causeway Bascule Bridge	Christa Mc Auliffe Bascule Bridge	Hallandale Bascule Bridge
0.1	0.41311	0.321192	0.233909
0.25	0.281708	0.229681	0.177095
0.40	0.196217	0.184993	0.152358

For shrink-fitting method 5 which did not involve dipping of hub in liquid nitrogen, OMCCL values decrease with hub radial thickness by as much as 63% for small bridge, 74% for the medium bridge, and 71% for the large bridge (Figure 33 and Table 14). For the medium and large bridges, the OMCCL values decrease with the radial

thickness of the hub. For the small bridge, the OMCCCL values decrease with the radial thickness of the hub up to a certain value and then increases.

**Table 14 OMCCCL values for different alpha values for all the bridges in AP2 for shrink-fitting method 5**

$\alpha$ - value	OMCCCL (inches)		
	17 <sup>th</sup> Street Causeway Bascule Bridge	Christa Mc Auliffe Bascule Bridge	Hallandale Bascule Bridge
0.1	19.4937	14.813	11.0136
0.25	7.21683	7.45489	5.55466
0.40	8.33249	3.78633	3.20381

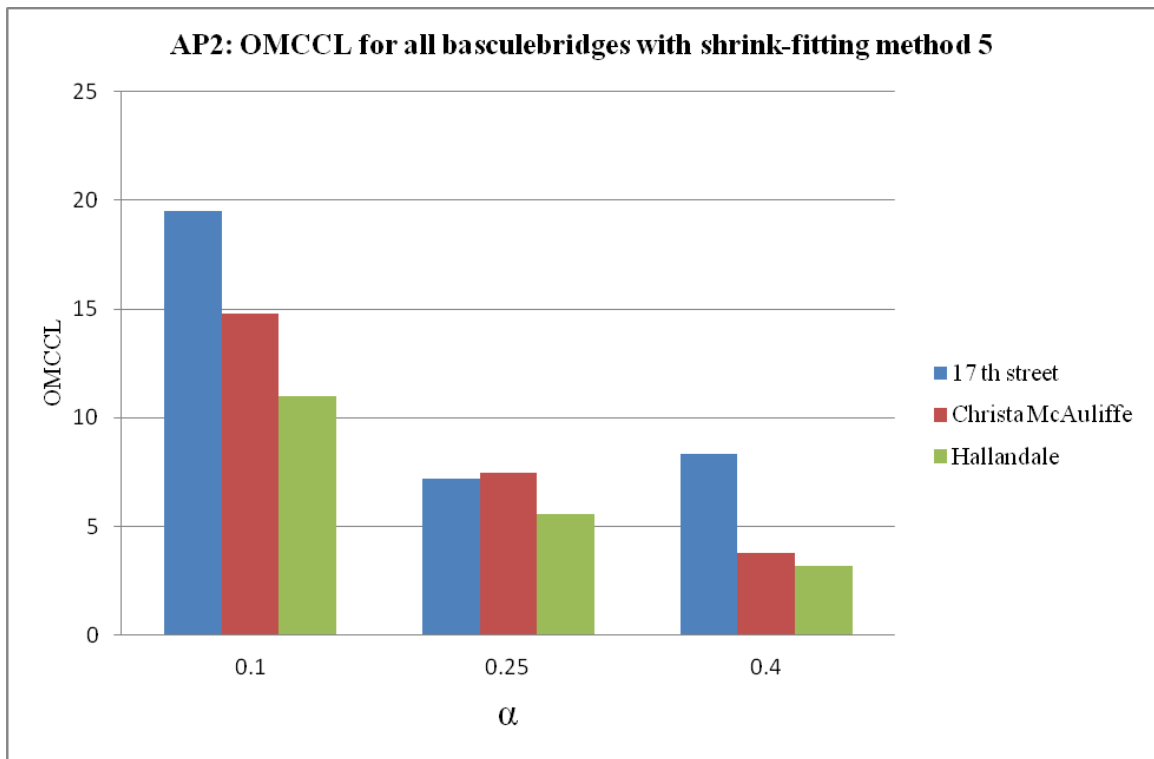


**Figure 33 OMCCCL values for different alpha values for all the bridges in AP2 with shrink-fitting method 5**

#### 4.5 Conclusions of AP2

1. Shrink-fitting method (Factor X) is the largest contribution factor to OMCCCL, from 68% to 73%, depending on the size of the bridge.

2. Shrink-fitting method 2, dipping TH assembly in dry-ice/alcohol mixture followed by dipping in liquid nitrogen increases the OMCCCL value by as much as 728% for a small bridge, 771% for medium bridge and 853% for a large bridge.
3. Shrink-fitting method 5 gives highest OMCCCL values but, shrink-fitting method 5 involves the assumption of heating the girder very slowly. Shrink-fitting method 2 is the next best choice of shrink-fitting.
4. In AP2, for all the shrink-fitting methods, increasing the hub radial thickness decreases OMCCCL values.

#### **4.6 Comparison of AP1 and AP2**

From the limited analysis conducted in previous studies, one would be led to believe that AP2 is the better choice of assembly procedure over AP1, but manufacturing logistics make AP2 to be less attractive. In AP1, the trunnion-hub (TH) assembly is performed by the manufacturing company (Step 1 and Step 2) and the TH assembly is then shipped to bridge site. The contractor assembles the TH assembly in bridge girder (Step 3 and Step 4). This separates the responsibility of the TH assembly manufacturers and the bridge contractors. However, in AP2, trunnion and hub components have to be shipped as separate components to the bridge site and the entire assembly procedure has to be at the site of construction. This overlaps the responsibility of the trunnion and hub manufacturers and the bridge contractors for the success of the assembly.

A comparative study is performed on AP1 and AP2 so that the bascule bridge contractors will have a better reference to the variations in assembly procedure and the associated strengths and weaknesses of each.

#### 4.6.1 Percentage Contribution of Factors

Table 15 shows the contribution of factors to OMCCCL in both AP1 and AP2. For both assembly procedures, shrink-fitting method (Factor X) is the largest contributing factor. In AP1, the contribution of shrink-fitting method has the largest contribution of 68% to 73%. In AP2, shrink-fitting method has the contribution of 51% to 75%. In AP1, the interaction between the hub radial thickness to hub inner diameter ratio,  $\alpha$  (Factor D) and shrink-fitting method has a contribution of 14% to 22%. In AP2, the interaction between factor D and factor X has a contribution of 18% to 22%. Shrink-fitting method contribution increases with increase in bridge size in AP1. However, in AP2 it does not show a significant trend.

**Table 15 Contribution of factors to OMCCCL in AP1 and AP2**

Parameter	Contribution to OMCCCL (%)					
	17 <sup>th</sup> Street Causeway Bascule Bridge		Christa McAuliffe Bascule Bridge		Hallandale Bascule Bridge	
	AP1	AP2	AP1	AP2	AP1	AP2
X	51.0	73.1	69.4	68.4	75.1	70.8
D	11.9	8.43	6.88	9.41	6.18	8.33
C	6.02	-	5.08	-	2.45	-
XD	22.1	18.5	13.8	22.2	14.6	20.9
XC	5.50	-	4.27	-	1.27	-
DC	0.927	-	0.0859	-	0.102	-
XDC	2.48	-	0.487	-	0.268	-

#### 4.6.2 Single-Step Shrink-Fitting Methods

From the above results, it is clear that shrink-fitting method is the largest contributing factor to OMCCCL values in both AP1 and AP2. Shrink-fitting method 1 (single step cooling in liquid nitrogen) is the most common shrink-fitting method implemented in the field and it is also the simplest (relatively easy to implement than multi-staged shrink-fitting methods) method of shrink-fitting method. If single step

shrink-fitting method is chosen, what would be the choice of assembly procedure? Intuitively, AP2 is the choice of assembly procedure but as explained in Section 4.6, manufacturing logistics makes it complex to implement. AP1 is easy to implement but is a less safe procedure than AP2. So, if the bridge contractor prefers to implement single step shrink-fitting method 1 then what assembly procedure should he/she choose, AP1 or AP2? To answer this question, OMCCCL values of both AP1 and AP2 for different  $\alpha$  values for shrink-fitting method 1 and for low and high interference case are compared for all the bridges used in this study.

In Figure 34, OMCCCL is plotted as a function of hub radial thickness to hub inner diameter ratio,  $\alpha$  for shrink-fitting method 1 and low value of FN3 radial interference for all the three bridges used in this study. The OMCCCL values are consistently smaller in AP1 as compared to AP2. For low value of  $\alpha = 0.1$ , the OMCCCL value is 59 to 69% less in AP1 when compared to AP2, but for high value of  $\alpha = 0.4$ , the OMCCCL value is only 33% to 34% less in AP1 than AP2. In AP1, the OMCCCL values do not vary with hub radial thickness (This result is already stated in the sensitivity analyses of AP1 in Section 3.4.2.2). In AP2, OMCCCL values decrease with hub radial thickness (This result is stated in the sensitivity analyses of AP2 in Section 4.4.2.2).

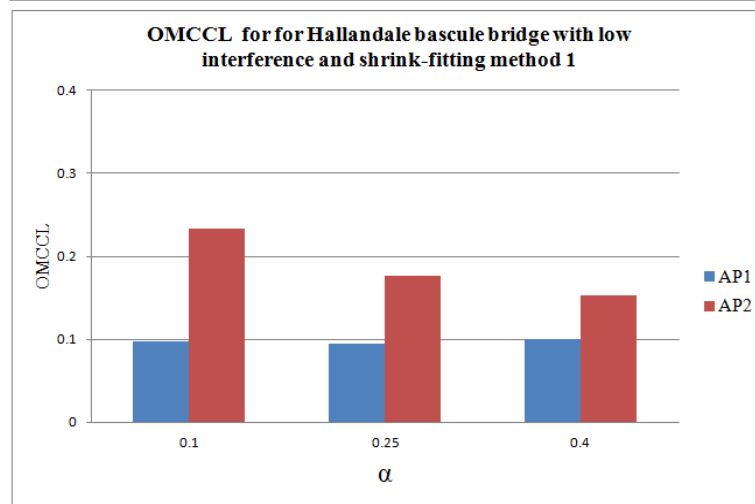
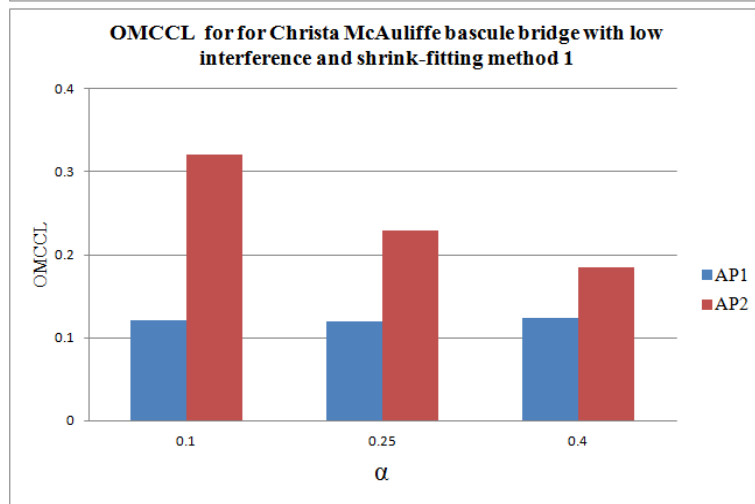
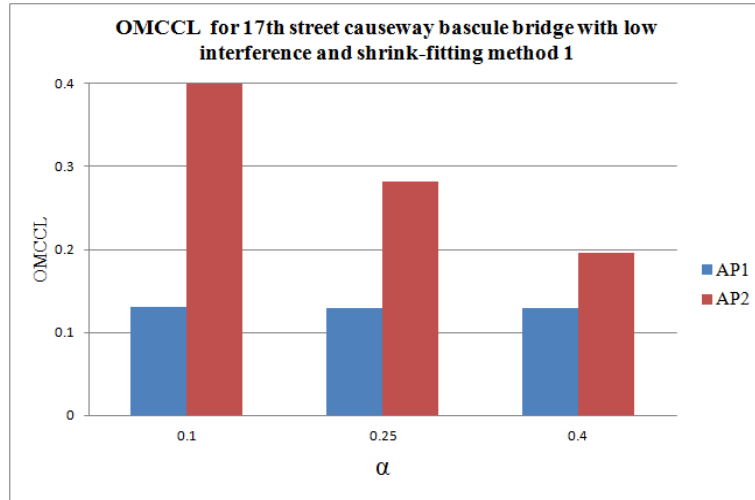


Figure 34 Variation of OMCCCL with alpha in AP1 and AP2 for low interference case

In Figure 35, OMCCCL is plotted as a function of hub radial thickness to hub inner diameter ratio,  $\alpha$  for shrink-fitting method 1 and high value of FN3 radial interference for all the three bridges used in this study. OMCCCL values vs.  $\alpha$  for high interference case follows the same trend of low interference case, that is, OMCCCL values of AP1 are consistently smaller when compared to AP2. In AP1, the OMCCCL values do not change with the change in  $\alpha$  value and in AP2, OMCCCL values decrease with the increase in  $\alpha$ . Comparing the OMCCCL values of AP1 from Figure 34 and Figure 35, we notice the OMCCCL values of AP1 are slightly lower in the high interference case. This is because higher radial interference causes higher tensile hoop stresses in the hub, hence decreasing the OMCCCL values. For low  $\alpha = 0.1$ , the OMCCCL values are 64% to 75% less in AP1 when compared to AP2, and for high  $\alpha = 0.4$ , the OMCCCL values are 38% to 42% less in AP1 than AP2.

From the above results, for single step cooling methods like shrink-fitting method 1, AP2 is recommended for bridges with low radial thickness and AP1 is recommended for bridges with high radial thickness.

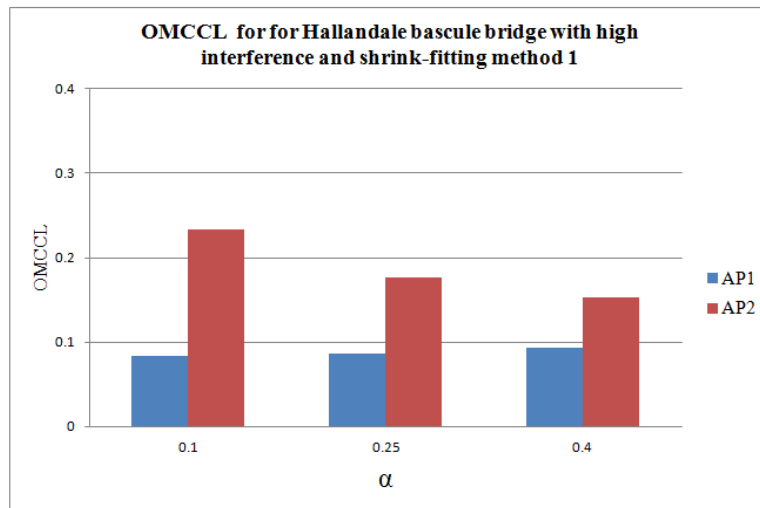
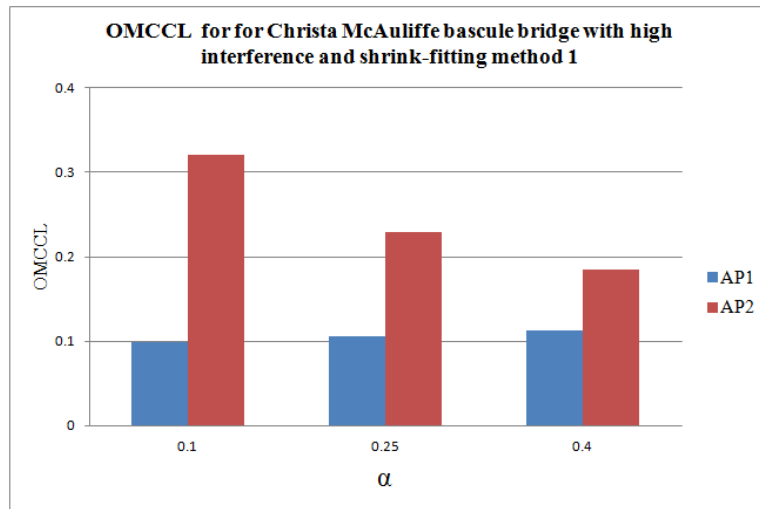
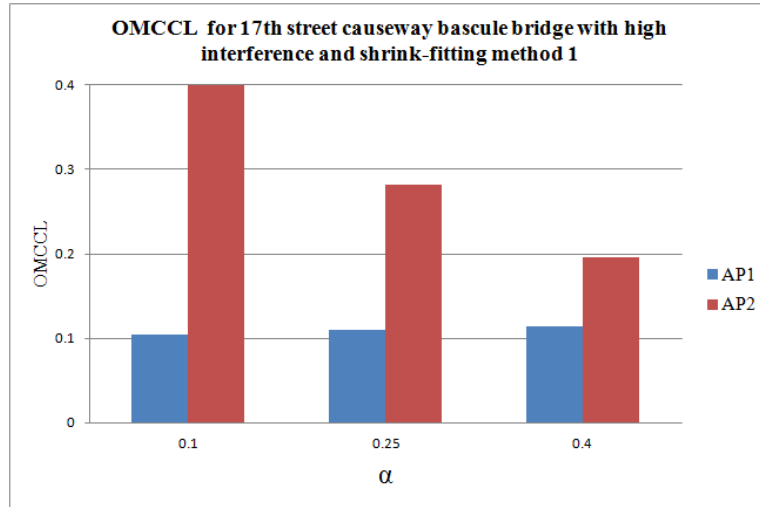


Figure 35 Variation of OMCCL with alpha in AP1 and AP2 for high interference case

### 4.6.3 Multi-Staged Shrink-Fitting Methods

If the bridge contractor prefers to implement staged cooling methods, then what would be the choice of shrink-fitting method and assembly procedure based on the geometrical parameters of the bridge? To answer this question OMCCCL values for different shrink-fitting methods for different values of  $\alpha$  for both AP1 and AP2 are compared for all the bridges used in this study.

In Table 16, OMCCCL is shown as a function of shrink-fitting method for both AP1 and AP2 for  $\alpha = 0.1$  and low interference case for all three bridges used in this study. Shrink-fitting method 5 gives the highest OMCCCL values. Shrink-fitting method 5 involves cooling of the TH (for AP1) or hub component (for AP2) and heating the girder slowly. When compared to conventional cooling, the increase in OMCCCL is up to 640% (result from section 3.4.2.1) in AP1 and more than 4500% (result from section 4.4.2.1) in AP2. Heating the girder may be a complex and time consuming process of the assembly. Amongst the shrink-fitting methods which involve only cooling, shrink-fitting methods 2 and 4 give the highest OMCCCL values. In fact, shrink-fitting methods 2 and 4 give identical OMCCCL values in both AP1 and AP2. Shrink-fitting method 2 is more desirable than shrink-fitting method 4 because shrink-fitting method 2 involves only two steps (immersion in dry-ice/alcohol mixture followed by immersion in liquid nitrogen) where as shrink-fitting method 4 involves three steps (immersion in refrigerated air followed by immersion in dry-ice/alcohol mixture and followed by immersion in liquid nitrogen). The increase in OMCCCL in AP2 by implementing shrink-fitting method 2 is 730% to 850% when compared to shrink-fitting method 1. However, in AP1, the increase in OMCCCL values is only 210% to 460%.

**Table 16 OMCCCL values for different shrink-fitting methods in AP1 and AP2 for low interference case for alpha=0.1**

Shrink-Fitting Method	OMCCCL (inches)					
	17 <sup>th</sup> Street Causeway Bascule Bridge		Christa McAuliffe Bascule Bridge		Hallandale Bascule Bridge	
	AP1	AP2	AP1	AP2	AP1	AP2
1	0.130	0.413	0.121	0.321	0.0968	0.234
2	0.408	3.42	0.518	2.80	0.548	2.23
3	0.255	1.27	0.272	0.948	0.243	0.695
4	0.408	3.42	0.518	2.80	0.548	2.23
5	0.476	19.5	0.585	14.8	0.718	11.0

In Table 17, OMCCCL is shown as a function of shrink-fitting method for both AP1 and AP2 for  $\alpha = 0.1$  and the high interference case for all the three bridges used in this study. For AP2 with high interference, the results are identical as interference is not a factor. For AP1, OMCCCL follows the similar trend as of the lower interference case.

**Table 17 OMCCCL values for different shrink-fitting methods in AP1 and AP2 for high interference case for alpha=0.1**

Shrink-Fitting Method	OMCCCL (inches)					
	17th Street Causeway Bascule Bridge		Christa McAuliffe Bascule Bridge		Hallandale Bascule Bridge	
	AP1	AP2	AP1	AP2	AP1	AP2
1	0.104	0.413	0.0988	0.321	0.0838	0.234
2	0.239	3.42	0.326	2.80	0.388	2.23
3	0.175	1.27	0.202	0.948	0.194	0.695
4	0.239	3.42	0.328	2.80	0.388	2.23
5	0.285	19.5	0.326	14.8	0.492	11.0

Based on the results from Table 16 and Table 17, for the bridges with low radial thickness, AP2 with shrink-fitting method 5 is recommended and if the bridge contractors prefer to implement AP1, shrink-fitting method 2 is recommended.

In Table 18, OMCCCL is shown as a function of shrink-fitting method for both AP1 and AP2 for  $\alpha = 0.4$  and low interference case for all the three bridges used in this

study. For both AP1 and AP2, shrink-fitting method 5 gives the highest OMCCCL values. The trends are very similar to data shown in Table 16 (for  $\alpha = 0.1$ ). However, for AP2, the increase in OMCCCL values is not as large (less than 60%) as  $\alpha = 0.1$ ; for AP1, unlike the low  $\alpha = 0.1$ , the increase in OMCCCL for shrink-fitting method 5 over shrink-fitting method 2 is more than 130%.

**Table 18 OMCCCL values for different shrink-fitting methods in AP1 and AP2 for low interference case for  $\alpha = 0.4$**

Shrink-Fitting Method	OMCCCL (inches)					
	17th Street Causeway Bascule Bridge		Christa McAuliffe Bascule Bridge		Hallandale Bascule Bridge	
	AP1	AP2	AP1	AP2	AP1	AP2
1	0.129	0.196	0.123	0.185	0.100	0.152
2	0.658	2.03	0.699	1.84	0.668	1.61
3	0.341	0.611	0.343	0.532	0.287	0.450
4	0.658	2.03	0.699	1.84	0.668	1.61
5	2.32	8.33	2.18	3.79	1.56	3.20

In Table 19, OMCCCL is shown as a function of shrink-fitting method for both AP1 and AP2 for  $\alpha = 0.4$  and high interference case for all the three bridges used in this study. For both AP1 and AP2, shrink-fitting method 5 gives the highest OMCCCL values. The trends are very similar to data shown in Table 16 (for  $\alpha = 0.1$ ). However, for AP2, the increase in OMCCCL values is not as large (less than 60%) as  $\alpha = 0.1$ . For AP1, unlike the low  $\alpha = 0.1$ , the increase in OMCCCL for shrink-fitting method 5 over shrink-fitting method 2 is more than 180%.

Based on the results from Table 18 and Table 19, for the bridges with high radial thickness, shrink-fitting method 5 is recommended for both AP1 and AP2.

**Table 19 OMCCCL values for different shrink-fitting methods in AP1 and AP2 for high interference case for  $\alpha=0.4$**

Shrink-Fitting Method	OMCCCL (inches)					
	17th Street Causeway Bascule Bridge		Christa McAuliffe Bascule Bridge		Hallandale Bascule Bridge	
	AP1	AP2	AP1	AP2	AP1	AP2
1	0.114	0.196	0.113	0.185	0.0938	0.152
2	0.402	2.03	0.460	1.84	0.479	1.61
3	0.258	0.611	0.261	0.532	0.240	0.450
4	0.402	2.03	0.460	1.84	0.479	1.61
5	1.25	8.33	1.79	3.79	1.37	3.20

#### 4.7 Conclusions from Comparison of AP2 and AP1

This section gives the overall summary of the results of the comparison of AP1 and AP2.

1. The shrink-fitting method is the largest contributing factor to OMCCCL in both AP1 and AP2.
2. For users with single staged shrink-fitting methods, AP1 is recommended for hubs with high radial thickness to inner diameter ratio ( $\alpha = 0.4$ ) while AP2 is recommended for hubs with low radial thickness to inner diameter ratio ( $\alpha = 0.1$ ).
3. For users with multi-staged shrink-fitting methods, for hubs with low  $\alpha$  value of 0.1, shrink-fitting method 5 is recommended for AP2, and shrink-fitting method 2 is recommended for AP1.
4. For users with multi staged shrink-fitting methods, for hubs with high  $\alpha$  value of 0.4, shrink-fitting method 5 is recommended for both AP1 and AP2.

5. The FEM model used in this study could be used for any bridge geometry to determine the assembly procedure and shrink-fitting method that would reduce the likelihood of fracture during the assembly.

## CHAPTER 5 ASSEMBLY PROCEDURE AP3

In the previous chapters (Chapter 3 and Chapter 4), two commonly used assembly procedures of bascule bridge fulcrum called AP1 and AP2 were compared via the design parameter OMCCCL by using the design of experiments (DOE) study. Although AP2 gives higher OMCCCL values, it is not the preferred assembly procedure because manufacturers prefer to supply the trunnion-hub (TH) assembly as per the specifications and leave the assembly of the TH into the girder to the bridge contractor. This clearly separates the responsibility of the manufacturers and the bridge contractor. But if AP2 needs to be implemented, the manufacturers and contractors need to work together for the success of the assembly. If the assembly fails when implementing AP2, it would be hard to place the responsibility on either party. Hence for convenience, AP1 is preferred over AP2. But, AP1 is the assembly procedure with higher likelihood of fracture during the assembly. In this chapter, alternate assembly procedures which give higher OMCCCL values than AP1-single stage shrink-fitting method and possibly AP1 multi-stage shrink-fitting method are proposed. They include realistic heating of the girder with heating coils. The two procedures proposed are:

1. Heating the girder alone for shrink-fitting TH assembly into the girder. In this study, it is called AP3-A.

2. Cooling the TH assembly in dry-ice/alcohol mixture and heating of the girder to shrink-fit TH assembly into the girder. In this study, it is called AP3-B.

Although the assembly procedure is defined as shrink-fitting method 5 in previous chapters (Chapter 3 and Chapter 4), it was assumed that heating of the girder is done very slowly and uniformly. This assumption gives near zero stresses in the girder and is unrealistic. The heating of the girder is done with heating coils placed around the girder hole or open flames on the surface of the girder around the girder hole. In this study, a more realistic heating mechanism of heating the girder with heating coils is chosen by

1. Placing the heating coils on the surface of the girder around the hole.
2. Modeling the heating coil material with commercially available heating coils.
3. Choosing the heat generation rates of commercially available heating coils.
4. Modeling the gap between the coils with actual properties of air.
5. Modeling the gravity and temperature dependent natural convective coefficients.
6. Modeling the insulation blankets with fiber glass material.

A full qualitative and quantitative study is performed on both AP3-A and AP3-B to determine the effect of geometric parameters and the level of interference on the design parameter OMCCL.

## 5.1 Assembly Procedure: AP3-A

In this assembly procedure, the girder is heated alone to shrink-fit the TH assembly (Figure 36).

This assembly procedure is characterized by the following steps.

1. The TH assembly is at room temperature ( $80^{\circ}F$ )
2. Heating coils are placed on the girder and heated till the girder hole expands to allow TH assembly to be inserted in to the girder hole.
3. The TH assembly is inserted in the expanded girder hole.
4. The entire assembly is allowed to cool to ambient room temperature. This creates an interference fit between the hub-girder (HG) interface.

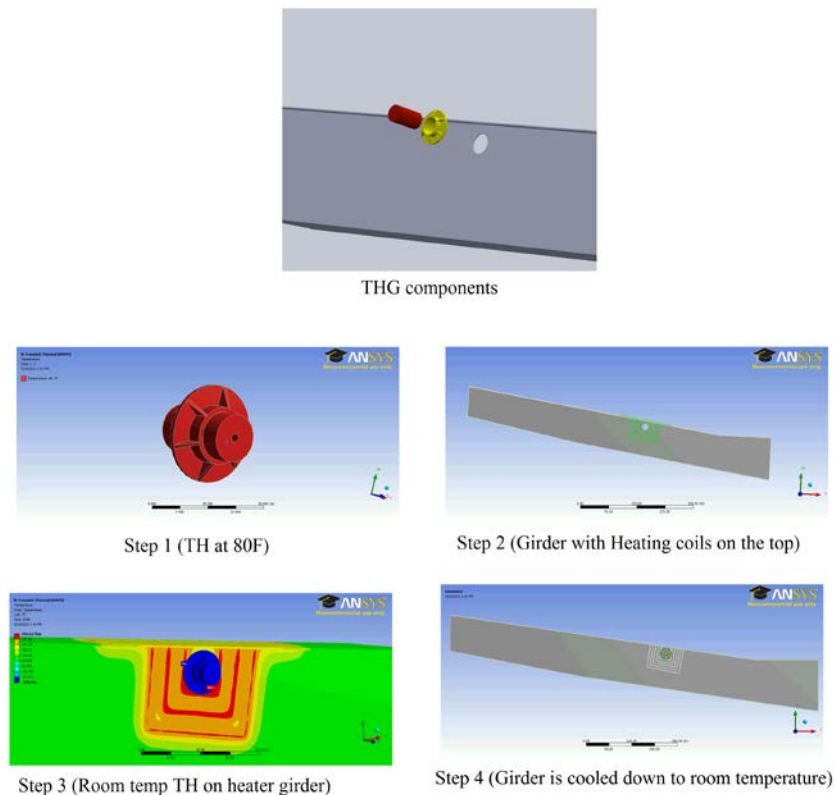


Figure 36 Assembly procedure AP3-A

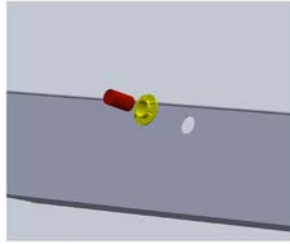
## 5.2 Assembly Procedure: AP3-B

In this assembly procedure, girder is heated and the TH assembly is cooled in dry-ice/alcohol mixture to shrink-fit the TH assembly into the girder hole (Figure 37).

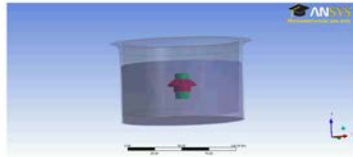
This assembly procedure is characterized by the following steps.

1. The TH assembly is immersed in dry-ice/alcohol mixture to contract the outer radius of the hub.
2. Heating coils are placed on the girder and heated till the girder hole expands to allow contracted TH assembly to be inserted in to the girder hole.
3. The contracted TH assembly is inserted in the expanded girder hole.
4. The entire assembly is allowed to cool/warm to ambient room temperature. This creates an interference fit between the hub-girder (HG) interface.

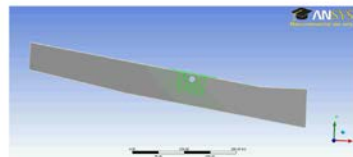
Intuitively in AP3, during the second step, that is, heating of the girder there is less likelihood failure via fracture because the fracture toughness of steel (ASTM A36) increases with temperature. However, the yield strength of the steel decreases with increasing temperature which suggests that the failure could occur by yielding (Figure 38).



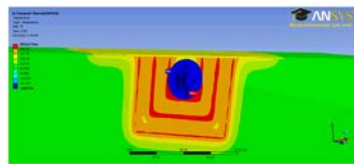
THG components



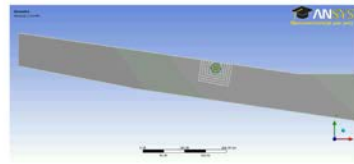
Step 1 (TH dipped in dry-ice alcohol)



Step 2 (Girder with Heating coils on the top)



Step 3 (TH at -108F on heated girder)



Step 4 (Girder is cooled down to room temperature)

**Figure 37 Assembly procedure AP3-B**

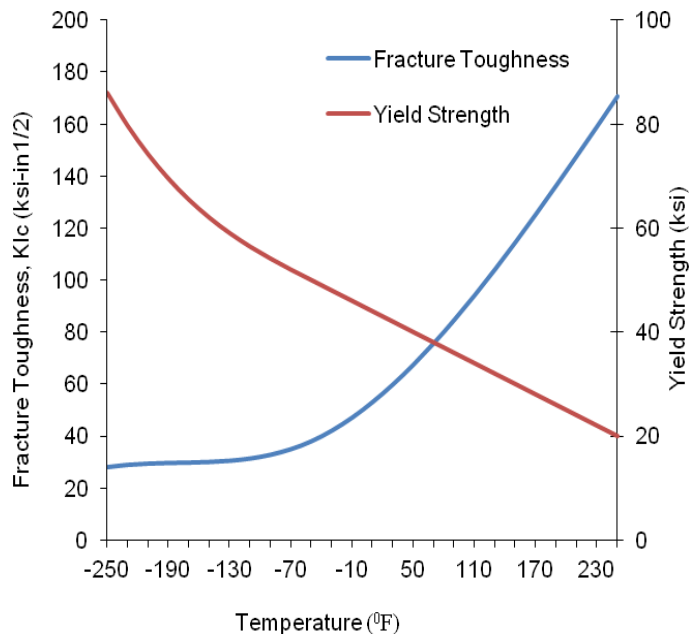


**Figure 38 Yield strength and fracture toughness of ASTM A36 as a function of temperature**

## 5.3 Finite Element Modeling

### 5.3.1 TH Assembly Modeling

A full 3D finite element model is built in ANSYS [57] as shown in Figure 39. The geometry is modeled in such a way that there is FN3 fit interference at trunnion-hub interface at room temperature.

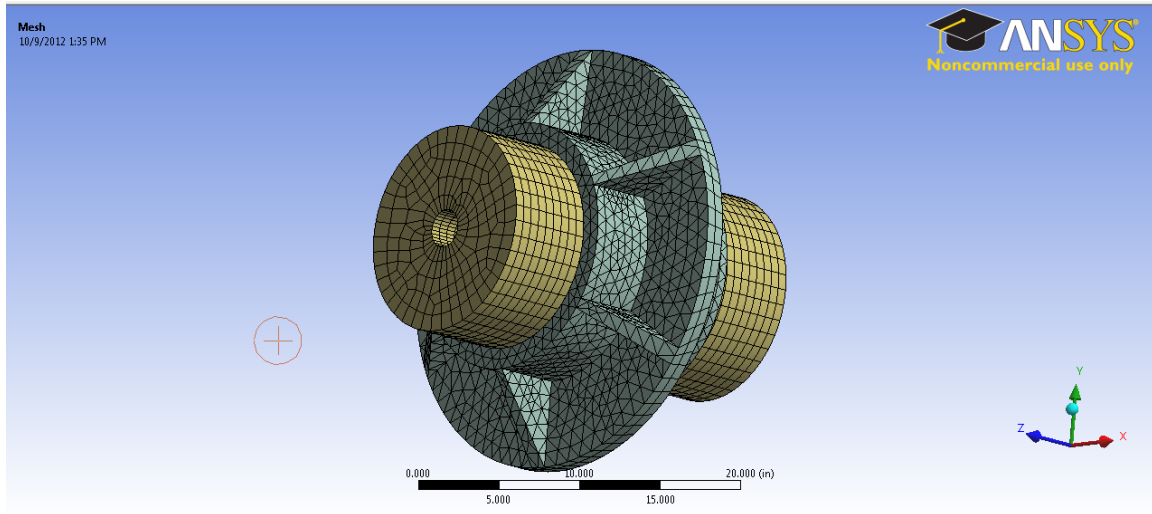


Figure 39 Finite element model of the TH assembly

The FN3 fit interference is modeled by modeling the outer diameter of the hub as slightly larger than its nominal diameter. Due to the TH FN3 interference, the outer diameter of the hub increases. Though the increase in diameter is not uniform throughout the circumference, the non-uniformity is very small. Hence, for this study the largest outer diameter of the expanded hub is taken. For AP3-A, this value of the hub largest diameter is needed because the girder hole diameter needs to reach this value plus the clearance of 0.01 inches when heated.

In the same finite element model, for AP3-B, thermal convection load is applied on the exterior faces which are exposed to dry-ice/alcohol mixture when immersed in the bath. The thermal convection loads simulates the dipping into dry-ice/alcohol mixture.

The model is run till the entire assembly reached the steady state temperature ( $-108^{\circ}F$ ). During the entire process, transient stresses and displacements are noted. Similar to AP3-A, the outer diameter of the hub is noted. The outer diameter of the hub obtained in AP3-B is the net effect of FN3 interference at TH interface and the applied thermal load of  $-108^{\circ}F$ . Hence, the outer diameter of the hub in AP3-B is less than the outer diameter of the hub obtained in AP3-A.

### 5.3.2 Girder Heating Modeling

The FEM model of the girder (Figure 40) is built in ANSYS. To model FN3 interference at room temperature, the girder hole is modeled as the nominal hub outer diameter minus the FN3 diametrical interference. The FN3 radial interference values for three bridges used in this study are given in Appendix C (C.2). The model is built in such a way that the coordinate axes center (0, 0) is the center of the girder hole. This facilitates easier analysis of the expansion of the hole.

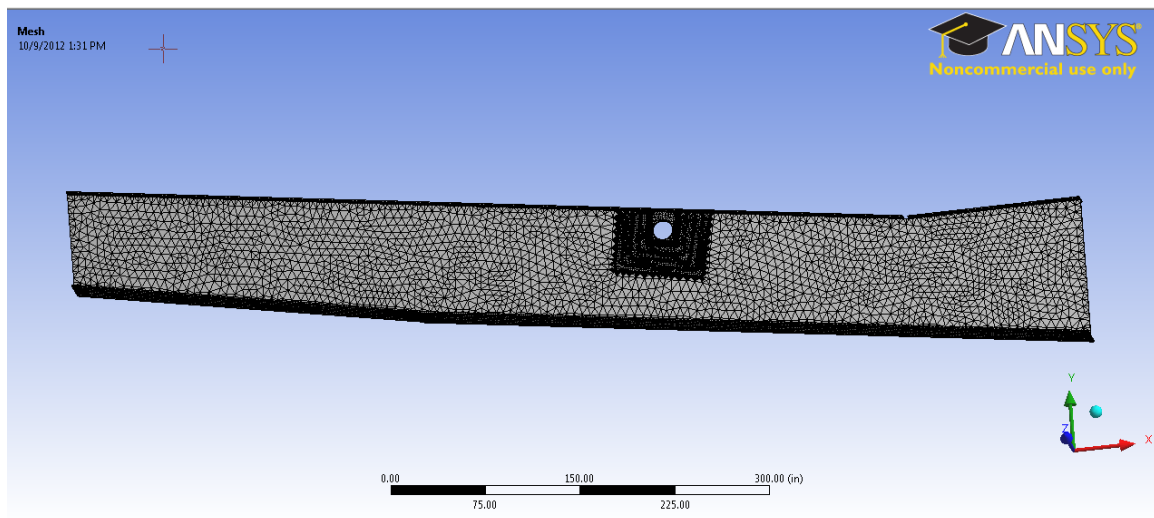
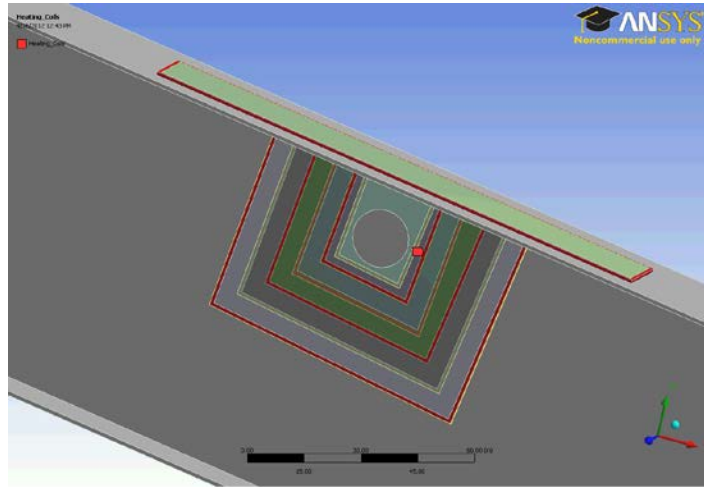


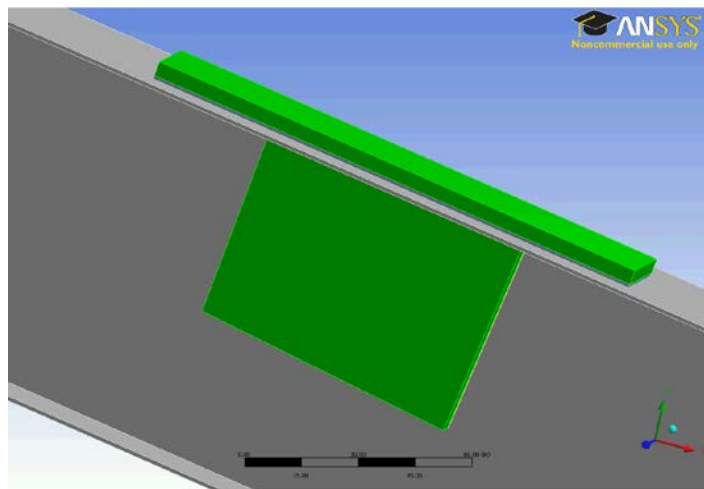
Figure 40 Finite element model of the girder

Three rectangular coils of thickness 1 inch each are placed on the surface of the girder near the hole. The heating coils in reality are composed of steel wire covered by a

ceramic shell. In ANSYS, the coils are modeled with material properties of ceramic shell (GE Advanced Ceramics HBN Hot-Pressed Boron Nitride [1]). The coils were given a heat generation rate of  $1.8 \frac{BTU}{min.in^3}$  [1]. To avoid the heat loss during heating, insulating heat blanket is modeled as fiber glass (E-glass) on the top of the heating coils with a thickness of 4 inches (Figure 41).



(a) Heating Coils



(b) Fiberglass insulation

Figure 41 a) Heating coils and, b) Fiber glass insulation on the girder

The material properties of the fiber glass [82] and ceramic shell [83] are given in the Table 20.

**Table 20 Material properties of fiber glass and ceramic shell [82, 83]**

Material	Density $\frac{lbm}{in^3}$	Thermal Conductivity $\frac{BTU}{in. min. ^\circ F}$	Specific Heat $\frac{BTU}{lbm. ^\circ F}$
Hot-Pressed Boron Nitride (HBN) ceramic	0.0759	0.04734	0.193
E-glass	0.09285	0.00104	0.194

Gravity and temperature dependent natural convection loads are applied on the top, bottom and side surfaces of the model that are exposed to air. To study the expansion of the hole precisely, the FEM model was meshed to have 720 nodes that are equally spaced along the circumference of the girder hole. After many configurations of coils, it is found that the top flange of the girder close to hole is providing resistance to expansion of the hole and causing high stresses. To avoid this problem, a heating coil is placed on the top flange.

### 5.3.2.1 Temperature and Gravity Dependent Natural Convection Coefficients

If  $T_{surface}$  is the temperature at a point on the surface, Rayleigh number  $Ra$  is given by the equation [84]

$$Ra = \frac{g\beta\Delta TL^3}{\nu^2} Pr$$

**Equation 73 Rayleigh number formula [84]**

In Equation 73,  $g$  = acceleration due to gravity,  $\beta$  = expansion coefficient of air,  $\Delta T$  = temperature difference ( $T_{surface} - T_{room}$ ),  $T_{room}$  = temperature of the ambient air,

$L$  = unit length (1 inch),  $Pr$  = Prandtl's number of air,  $\nu$  = coefficient of kinematic viscosity of air.

The values of  $\beta$ ,  $Pr$  and  $\nu$  for air [85] are found at the mean temperature value  $\left(\frac{T_{surface} + T_{room}}{2}\right)$ . Rayleigh number is thus obtained by using these values. After obtaining the Rayleigh number, Nusselt number is to be calculated depending on the orientation of the surface with respect to ground (Facing top, bottom and side).

If the surface is facing upwards, the Nusselt number is calculated by using the two-dimensional flat plate theory of a horizontal plate where the surface is facing upwards [84].

$$\begin{aligned} Nu_{Top} &= 0.16 \times Ra^{1/2}, 7 \times 10^6 < Ra < 2 \times 10^8 \\ &= 0.13 \times Ra^{1/2}, 5 \times 10^8 < Ra \end{aligned}$$

**Equation 74 Nusselt number for surface facing upwards [84]**

If the surface is facing downwards, the Nusselt number is calculated by using the two-dimensional flat plate theory of a horizontal plate where the surface is facing downwards [84].

$$Nu_{Bottom} = 0.27 \times Ra^{1/4}, 10^6 < Ra < 10^{11}$$

**Equation 75 Nusselt number for surface facing downwards [84]**

If the surface is facing sideways, the Nusselt number is calculated by using the two-dimensional flat plate theory of a vertical plate where the surface is facing sideways [84].

$$Nu_{Side} = 0.27 + \frac{0.67 Ra^{\frac{1}{4}}}{\left[1 + \left(\frac{0.492}{Pr}\right)^{\frac{9}{16}}\right]^{\frac{4}{9}}}$$

**Equation 76 Nusselt number for surface facing sideways [84]**

Now the convection coefficients are found by using the relation [84],

$$h = Nu \times k$$

**Equation 77 Convection coefficient [84]**

$k$  - is the thermal conductivity of the air at  $\left(\frac{T_{surface} + T_{room}}{2}\right)$ .

The convection coefficients used in this study are given in Table 21.

**Table 21 Natural convection coefficients used in heating of the girder**

Temperature, °F	Sides BTU	Top BTU	Bottom BTU
	$\frac{\text{BTU}}{\text{min} \cdot \text{in}^2 \cdot ^\circ \text{F}}$	$\frac{\text{BTU}}{\text{min} \cdot \text{in}^2 \cdot ^\circ \text{F}}$	$\frac{\text{BTU}}{\text{min} \cdot \text{in}^2 \cdot ^\circ \text{F}}$
70	$2.5984 \times 10^{-6}$	0	0
102	$9.3211 \times 10^{-5}$	$9.3212 \times 10^{-5}$	$3.6494 \times 10^{-5}$
210	$1.2808 \times 10^{-4}$	$1.4071 \times 10^{-4}$	$5.0630 \times 10^{-5}$
354	$1.5417 \times 10^{-4}$	$1.7260 \times 10^{-4}$	$6.1015 \times 10^{-5}$
714	$1.6672 \times 10^{-4}$	$1.7946 \times 10^{-4}$	$6.6011 \times 10^{-5}$

#### 5.4 Girder Hole Expansion Analysis

The model is solved in two stages; first the thermal problem is solved to get the temperature distribution of the girder after each time step of heating (1 minute). Then these temperatures are applied as loads to find the displacements and the stresses in the girder.

After each time step, the output of the ANSYS is written to a text file which contains the nodal locations, displacements, stresses and the temperatures. A MATLAB

program is developed to read the data from the output text file generated by ANSYS. The expanded location of the nodes on the circumference of the girder hole is obtained by summing the nodal location and nodal displacements in the Cartesian coordinates.

$$x_{heat} = x + u_x$$

$$y_{heat} = y + u_y$$

**Equation 78 Cartesian coordinates of the expanded hole**

where,  $x_{heat}$  = final  $x$  coordinate of the node after heating,  $y_{heat}$  = final  $y$  coordinate of the node after heating,  $x$  = initial  $x$  coordinate of the node before heating,  $y$  = initial  $y$  coordinate of the node before heating,  $u_x$  = displacement of node in  $x$  direction due to heating,  $u_y$  = displacement of node in  $y$  direction due to heating.

Now, the expanded hole is separated out as top curve,  $f(x)$  and bottom curve,  $g(x)$ . The new centroid of the expanded hole is given by [86]

$$x_{centroid} = \frac{\int x[f(x) - g(x)]dx}{\int [f(x) - g(x)]dx}$$

$$y_{centroid} = \frac{1}{2} \frac{\int [(f(x))^2 - (g(x))^2]dx}{\int [f(x) - g(x)]dx}$$

**Equation 79 Cartesian coordinates of the centroid of an irregular area**

$x_{centroid}$  =  $x$ -coordinate of the centroid of the expanded girder hole,  $y_{centroid}$  =  $y$ -coordinate of the centroid of the expanded girder hole.

After obtaining the centroid of the expanded hole, all the nodal locations of the nodes on the expanded girder hole are transformed with respect to the centroid of the

girder hole. This transformation could be done by using the basic transformation of axes theory [87].

$$x_{new} = x_{heat} - x_{centroid}$$

$$y_{new} = y_{heat} - y_{centroid}$$

$x_{new}$  =  $x$ -coordinate of the node on the expanded hole with respect to the new centroid,  $y_{new}$  =  $y$ -coordinate of the node on the expanded hole with respect to the new centroid.

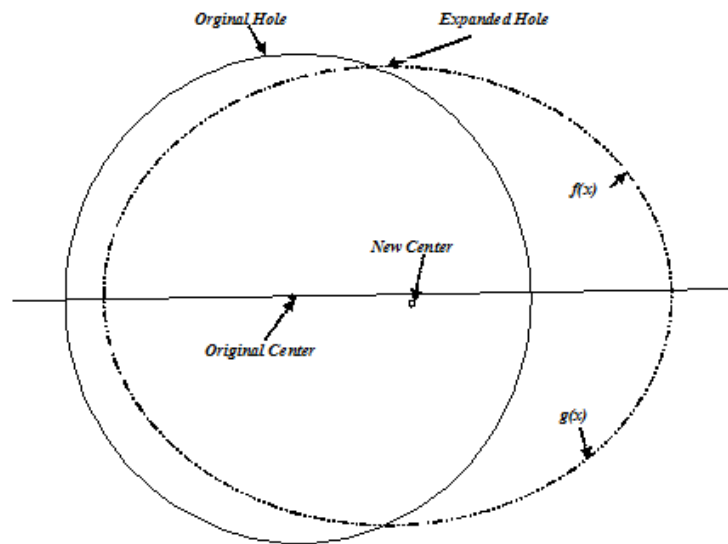


**Figure 42 Breaking the girder hole edge into two curves to find the centroid of the expanded hole**

Now the Cartesian coordinates are transformed to radial coordinates and the lengths of the chords passing through the centroid are found. This procedure is followed throughout the thickness of the girder hole and the length of the smallest chord is taken as the diameter of the expanded girder hole. This process is repeated for each minute of heating till the girder hole expanded to a value equal to the sum of the outer diameter of the hub (expanded due to TH interference) and the clearance value of 0.1 inches. Throughout the heating process, OMCCCL and OMSR values are calculated. Note that

while calculating OMCCCL and OMSR values, temperature dependency of the yield strength and fracture toughness is taken into account.

## 5.5 Results

### 5.5.1 AP3-A

AP3-A is the assembly procedure in which only the girder is heated to get the required expansion of the girder hole. For the coil configuration used in this study, it took 300 minutes of heating time to get the expansion needed for TH assembly to go inside the girder hole. For all the bridges used in this study, the OMCCCL values obtained during this process were very high (about 12 inches) which cancelled out the possibility of failure by crack propagation, however, Von-Mises stresses in the girder were greater than the yield strength ( $OMSR < 1$ ) of the steel causing the girder to fail by yielding. Many different configurations were used to heat the girder and not cause failure by yielding. None of the configurations were able to give lower than failing Von-Mises stresses. This failure by yielding raised concerns and an in-depth study is conducted to find the reason for these high Von-Mises stresses.

The temperature profile explains the primary reason for high Von-Mises stresses. As the girder is heated for a long time (more than 80-90 minutes), the surface of the girder very close to the heating coils gets very hot because the heat conduction rate inside the girder is very slow compared to the heat generation rates of the coils. Also, the heat lost by the girder due to natural convection is relatively very low compared to the heat generation rates of the coil. Hence, high temperature zones are formed around the coils and low temperature zones away from the coils. This high temperature difference (thermal gradient) led to the development of large Von-Mises stresses, causing the girder

to fail by yielding. After this observation several other (about 30) configurations were tried by changing the spatial arrangement of coils, length of coils, and heat generation rate. Most of the configurations gave high Von-Mises stresses ( $OMSR < 1$ ). Few configurations worked, but the heat generation was considerably very low (so that there is enough time for girder steel to conduct the heat) in those configurations. These coil configurations gave very low temperature gradient resulting in low thermal stresses. These configurations are not valid because the heat generation rates are very low compared to the heat generation rates observed in the field and they take about 15 hours of heating time to get enough expansion of the girder hole so that the TH assembly could go inside it.

### **5.5.2 AP3-B**

In AP3-B, the TH assembly is cooled in dry-ice/alcohol mixture and the girder is heated to shrink-fit the TH assembly in the girder. With the coil configuration used in this study, it took only 45 minutes of heating time to get enough expansion of the girder hole. In AP3-B, for all the bridges used in this study, OMSR values during the heating of the girder and also during the cooling of the TH assembly in dry-ice/alcohol mixture are found to be greater than one. These results show that unlike in AP3-A, failure in AP3-B does not occur by yielding. The OMCCCL values were very high (more than 15 inches) during the heating of the girder for all the bridges used in this study. These results indicate that AP3-B is a feasible assembly procedure.

In AP3-B, OMCCCL values obtained during the cooling of the TH assembly in dry-ice/alcohol mixture are smaller than the OMCCCL values obtained during the heating of the girder. Hence in AP3-B, the critical step (OMCCCL values are obtained from this

step) is the dipping of the TH assembly in dry-ice/alcohol mixture. In AP3-B, failure could occur only due to low fracture toughness of material during the immersion of TH assembly in dry-ice/alcohol mixture, a full sensitivity analysis is carried out by using the DOE [59] study only on design parameter OMCCL.

### 5.5.3 Sensitivity Analysis for AP3-B

There are two main factors for the general factorial design. 1) Hub radial thickness to hub inner diameter ratio,  $\alpha$  (factor D), 2) TH interference (Factor C). The interference at hub-girder (HG) interface is not included as a factor because in AP3-B, the critical step is cooling the TH assembly in dry-ice/alcohol mixture. Also, the shrink-fitting method is not a factor because AP3-B has only one shrink-fitting method which is cooling in dry-ice/alcohol mixture. The factors and their levels are shown in Table 22.

**Table 22 All factors and levels for general factorial design of AP3-B**

Factor	Levels
TH interference (factor C)	Low
	High
Hub radial thickness to hub inner diameter ratio, $\alpha$ (factor D)	0.1
	0.25
	0.4

The total number of runs for the DOE is given by the product of all the levels of the factors for each bridge. For this analysis,  $3(\text{hub radial thickness to hub inner diameter ratio, } \alpha) \times 2(\text{levels of interference}) = 6$  runs are made for each bridge. A total of 18 runs are made for all the three bridges used in this study.

The contributions of all factors and their interactions for AP3-B are given in Table 23. Hub radial thickness to hub inner diameter ratio,  $\alpha$  has the largest contribution between 71% and 89%. The factor TH radial interference has a contribution between 9%

and 21%. The contribution of  $\alpha$  increases with the increase in bridge size. An opposite trend is observed for TH interference (Table 23).

**Table 23 Contribution of factors to OMCCCL in AP3-B**

Parameter	OMCCCL (%)		
	17th Street Causeway Bascule Bridge	Christa McAuliffe Bascule Bridge	Hallandale Bascule Bridge
C	21	12	9
D	72	86	89.5
CD	7	2	1.5

Figure 43 shows OMCCCL as a function of  $\alpha$  for all the three bridges for both low and high interference case. For small (17<sup>th</sup> street causeway) and medium (Christa McAuliffe) bridges, OMCCCL values increase with hub radial thickness. For a large bridge (Hallandale), the OMCCCL values increase with hub radial thickness up to a certain value. Beyond a certain value of radial thickness, the OMCCCL values decrease with the hub radial thickness.

From Figure 43, for low interference case, the increase in OMCCCL with hub radial thickness is as much as 387% for small bridge (17<sup>th</sup> street causeway), 272% for medium bridge (Christa McAuliffe), and 164% for large bridge (Hallandale)( $\alpha = 0.25$ ). For high interference case, the increase in OMCCCL with hub radial thickness is as much as 337% for small bridge (17<sup>th</sup> street causeway), 448% for medium bridge (Christa McAuliffe), and 192% for large bridge (Hallandale)( $\alpha = 0.25$ ). From these results, it is clear that increasing the radial thickness of the hub during the design stage significantly increases the safety of the assembly AP3-B by decreasing the possibility of failure by TH cracking.

Figure 44 shows the variation of OMCCCL with TH interference. In AP3-B, OMCCCL value decreases with the increase in TH interference for all the three bridges. For  $\alpha = 0.1$ , OMCCCL value decreases with increase in interference by as much as 40% in a small bridge, 44% in a medium bridge, and 32% in a large bridge. For  $\alpha = 0.25$ , OMCCCL values decrease with increase in interference by as much as 45% in a small bridge, 41% in a medium bridge, and 24% in a large bridge. For  $\alpha = 0.4$ , OMCCCL values decrease with increase in interference by as much as 46% in a small bridge, 18% in a medium bridge, and 12% in a large bridge. Although, intuitively one may believe that high TH interference would endanger the assembly procedure significantly, but from the above results it is clear that TH interference increases the possibility of TH cracking, but this increase is not significant.

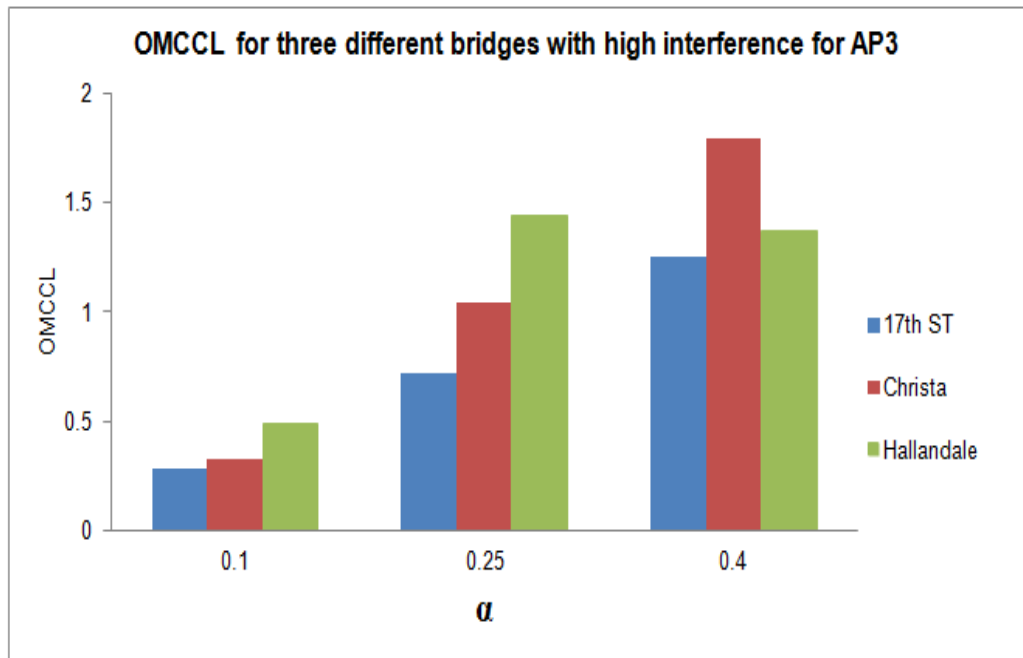
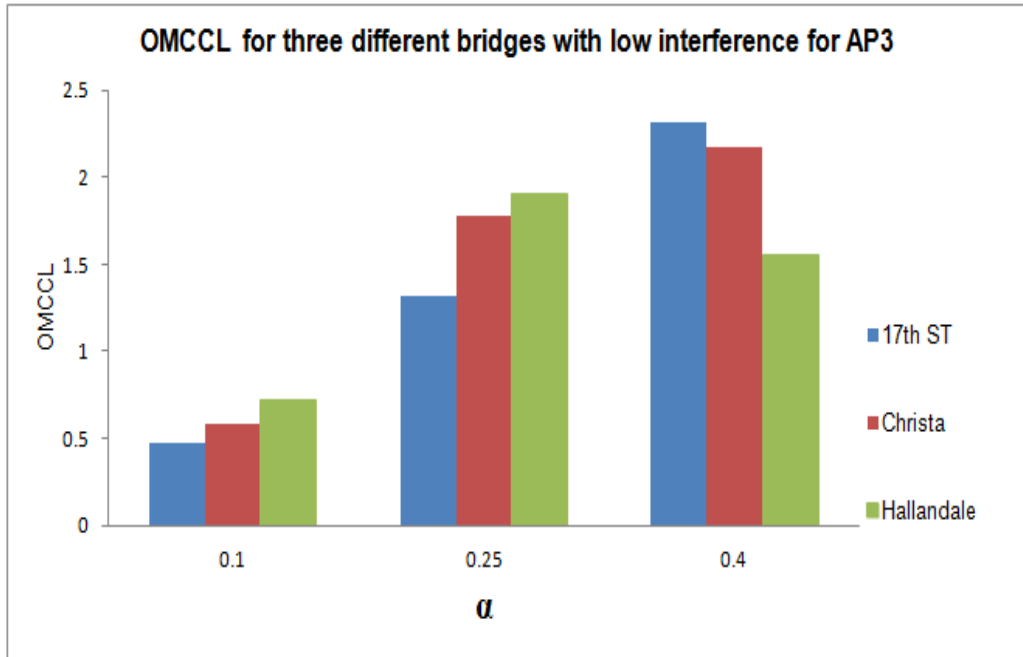


**Figure 43 OMCCL as a function of alpha in AP3-B**

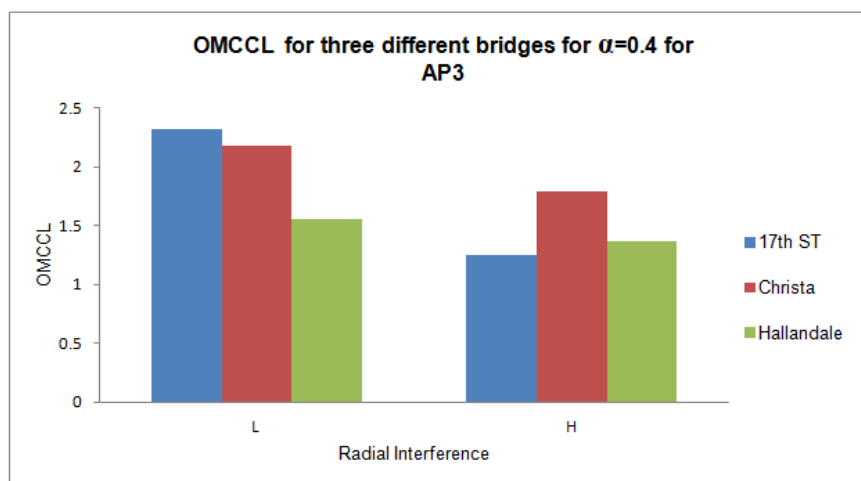
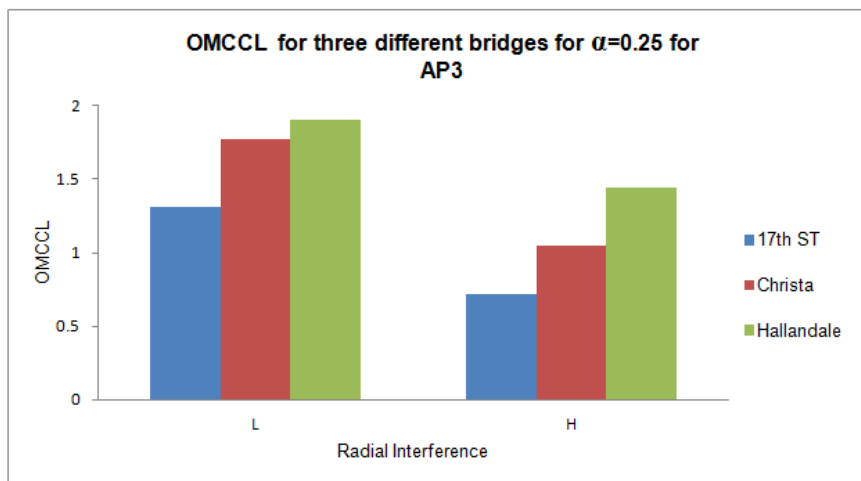
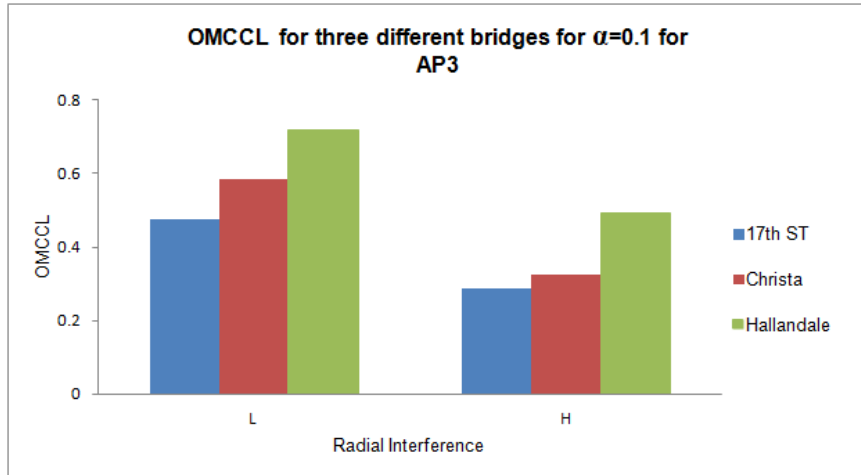


**Figure 44 OMCCL as a function of TH interference in AP3-B**

## 5.6 Comparison of AP3-B with AP1

Both AP3-B and AP1- preferred multistage shrink-fitting (shrink-fitting method 2) assembly procedures are same until the step of cooling the TH assembly in dry-ice/alcohol mixture, but in AP3-B instead of further cooling the TH assembly in liquid nitrogen, the girder is heated to get enough clearance for the assembly. In AP1, in all the shrink-fitting methods that involve only cooling the TH assembly, dipping the TH assembly in liquid nitrogen is the critical step. In AP3-B, cooling TH assembly in dry-ice/alcohol mixture is the critical step.

In Table 24, percentage contributions of all factors for both AP3-B and AP1 are listed for comparison purpose. In AP3-B and AP1, hub radial thickness to hub inner diameter ratio is the largest contribution factor (although in AP1, shrink-fitting method (Factor X) is the largest contribution factor, and AP3-B has only one shrink-fitting method).

**Table 24 Percentage contribution of factors to OMCCL in AP1 and AP3-B**

Parameter	OMCCL (%) comparison AP1 and AP3-B					
	17th Street Causeway Bascule Bridge		Christa McAuliffe Bascule Bridge		Hallandale Bascule Bridge	
	AP1	AP3-B	AP1	AP3-B	AP1	AP3-B
X	51.0	-	69.4	-	75.1	-
D	11.9	72	6.88	86	6.18	89.5
C	6.02	21	5.08	12	2.45	-
CD	0.927	7	0.0859	2	0.102	1.5
XD	22.1	-	13.8	-	14.6	-
XC	5.50	-	4.27	-	1.27	-

In Figure 45, OMCCL is plotted as a function of  $\alpha$  for assembly procedures AP1- single stage shrink-fitting method (dipping in liquid nitrogen), AP1-preferred multi stage shrink-fitting method (dipping in dry-ice/alcohol mixture and then dipping in liquid

nitrogen; shrink-fitting method-2), and AP3-B. From Figure 45, OMCCCL values in AP3-B are significantly larger than both AP1-single stage shrink-fitting and AP1-multi stage shrink-fitting. The percentage increase of OMCCCL values in AP3-B when compared to single stage shrink-fitting of AP1 increases with increase in  $\alpha$  value. The same trend is observed when the comparison is made between OMCCCL values of AP3-B and multi-stage shrink-fitting method of AP1.

The percentage increase of OMCCCL values in AP3-B when compared to AP1 single-stage shrink-fitting and multi-stage shrink-fitting for three Florida bridges for different  $\alpha$  values for low interference case are given in the Table 25. From the results given in Section 3.4.2.1, adopting AP1-multistage shrink-fitting method increases the OMCCCL values by as much as 466% when compared to AP1 single-stage shrink-fitting method. But, from Table 25, AP3-B increases the OMCCCL values by at least 265% for hubs with low radial thickness and by at least 1454% for hubs with high radial thickness. From these results, contractors implementing single-stage shrink-fitting method are recommended to implement multi-stage shrink-fitting methods like AP3-B to significantly decrease the possibility of failure by hub cracking during the assembly.

From Table 25, the increase in OMCCCL in AP3-B when compared to preferred multi-stage shrink-fitting method of AP1 is only 31% for hubs with low radial thickness, but for hubs with high radial thickness, the increase in OMCCCL is significant (as much as 253%). From these results, for contractors with multi-stage shrink-fitting methods, it is recommended to implement AP1 if the hub radial thickness is low and AP3-B if the radial thickness is high.

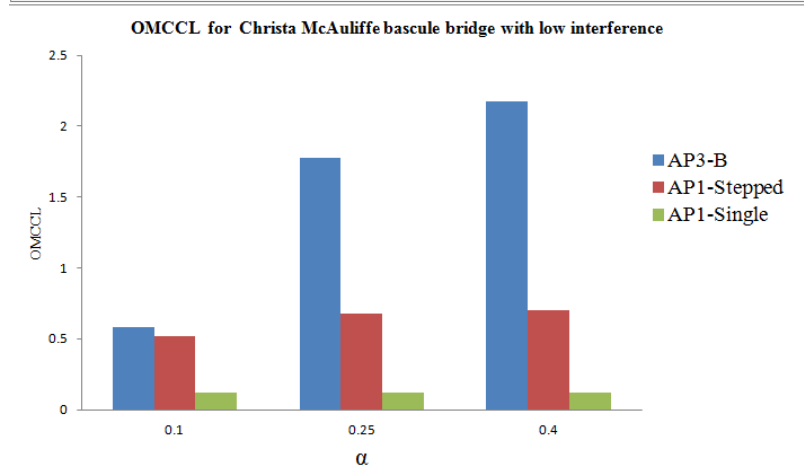
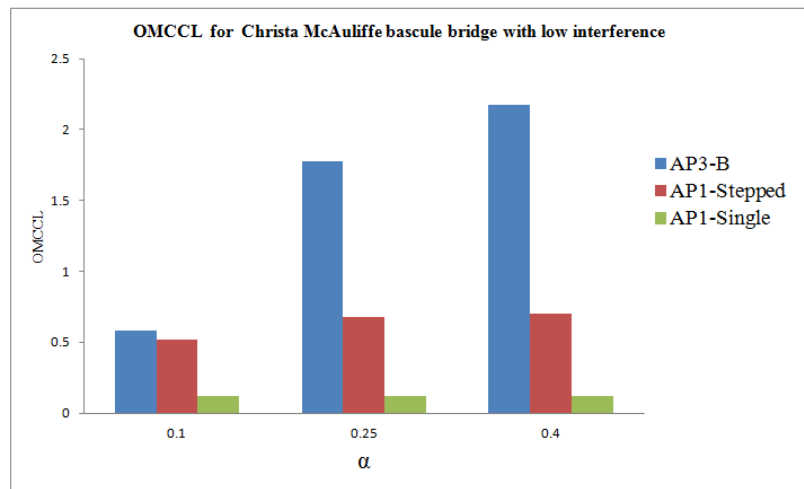
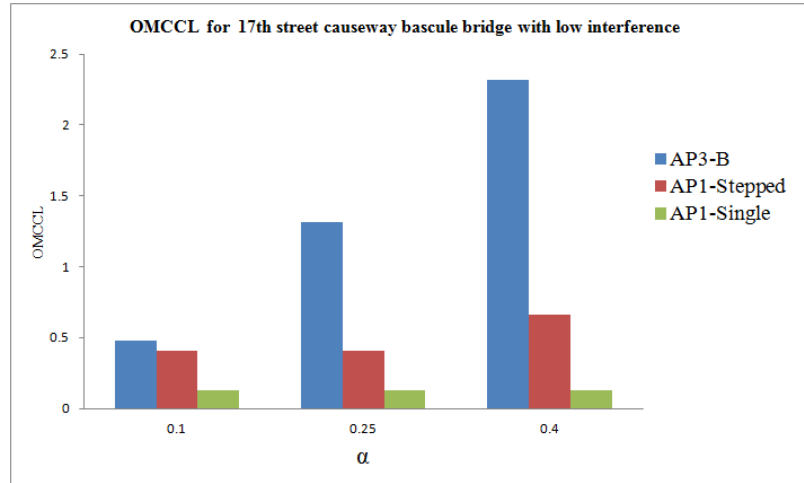


Figure 45 Comparison of OMCCL for three assembly procedures as a function of alpha for three bridges and for low TH radial interference

**Table 25 Percentage increase in OMCCL values in AP3-B compared to single-stage and multi-stage shrink-fitting methods of AP1 (for low interference case)**

Bridge Name	hub radial thickness to hub inner diameter ratio, $\alpha$	percentage increase of OMCCL compared to AP1-single-staged cooling	percentage increase of OMCCL compared to AP1-multi-staged cooling
17th Street Causeway Bascule Bridge	0.1	265	17
	0.25	913	222
	0.4	1702	253
Christa McAuliffe Bascule Bridge	0.1	384	13
	0.25	1380	160
	0.4	1663	211
Hallandale Bascule Bridge	0.1	642	31
	0.25	1915	185
	0.4	1454	133

## 5.7 Conclusions from Comparing AP3-B and AP1

From the results and discussions made in this chapter, the main conclusions and recommendations are given below.

1. To get clearance for TH assembly into the girder hole, it is recommended to combine heating of the girder and cooling of the TH assembly rather than trying to heat the girder alone in reasonable time.
2. Multi-stage shrink-fitting methods are recommended over the single-stage shrink-fitting methods. That is either conduct multi-stage shrink-fitting of the TH assembly by cooling in dry-ice/alcohol mixture and then in liquid nitrogen or combine the heating of the girder and cooling of the TH assembly in dry-ice/alcohol mixture.
3. Increasing the hub radial-thickness during the design stage decreases the possibility of failure due to cracking significantly.

4. For hubs with low radial thickness, AP1 multi-staged cooling is recommended and for hubs with large radial thickness, AP3-B is recommended.
5. If the contractor is adopting AP3-B assembly procedure, the amount of TH interference does not significantly affect the safety of the assembly. That is, the contractor does not need to worry about the amount of FN3 interference present at TH interface due to manufacturing logistics when he receives the assembly at the site of bridge construction.

## CHAPTER 6 RECOMMENDATIONS AND SUGGESTIONS

### 6.1 Conclusions and Recommendations to Assemblers and Bridge Designers

Assembling the THG assembly for bascule bridges can be accomplished by following several different procedures. This study thoroughly analyzed existing and newly suggested procedures for establishing guidelines and recommendations to THG assemblers and bridge contractors.

Recalling Chapter 3 and Chapter 4, shrink-fitting method-5 gives the same OMCCCL values as AP3-B (in both the assembly procedures, dipping the TH in dry-ice/alcohol mixture is the critical step). So, shrink-fitting method 5 is replaced with AP3-B for comparison purposes. Also, as shrink-fitting method 2 (dipping in dry-ice/alcohol mixture followed by dipping in liquid nitrogen) is the most efficient and convenient method of multi-staged shrink-fitting methods involving only cooling, shrink-fitting methods 3 and 4 are ignored. So, in the discussion below, multi-staged shrink fitting method refers to shrink-fitting method 2, and AP3-B refers to combination of heating the girder and cooling the TH assembly in dry-ice/alcohol mixture.

The following are the conclusions and recommendations for the fulcrum assembly procedures of bascule bridges.

1. For any assembly procedure (AP1, AP2, AP3-A, or AP3-B), shrink fitting method is the largest contributing factor to OMCCCL.

2. Either in AP1 or AP2, switching from single-staged shrink-fitting method to multi-staged shrink-fitting method decreases the likelihood of failure significantly.
3. If AP1 is implemented and if TH assembly is to be cooled in liquid nitrogen either in single-stage or multi-stage shrink-fitting method, increasing the radial thickness of the hub,  $\alpha$  during the design stage of the component by the bridge designer does not decrease the likelihood of hub fracture during the assembly; instead, it increases the cost of the component.
4. If AP2 is implemented, increasing the radial thickness of the hub actually increases the likelihood of fracture of the hub during the assembly. This forces bridge designers to design hub component with minimum radial thickness required to withstand the torque applied to lift the leaf of the bridge. But, in most design practices, designers provide additional radial thickness to the hub (they choose high factor of safety) thinking it would make the hub safer during its operation (lifting of the span of the bridge - torque loading). But, increasing the radial thickness of the hub actually increases the likelihood of failure of the hub during the assembly stage, and that is even before it becomes operational.
5. If the contractor wants to heat the girder in a reasonable time, then it is not recommended to heat just the girder. It is much better to heat the girder and cool the TH assembly in dry-ice/alcohol mixture.

6. If the contractor wants to heat the girder, then the designer could choose high factor of safety and increase the radial thickness of the hub to decrease the likelihood fracture during the assembly and also during the operation.
7. Amount of FN3 radial interference in the TH assembly does not affect either AP1 or AP3-B (TH interference is not present in AP2).

## **6.2 Broader Impact**

This research project not only provides better guidelines to bridge contractors in North America but to all bridge contractors around the world. The results from this dissertation could readily be applied to assembling of large movable steel structures involving a fulcrum-like mechanism.

The research conducted in this dissertation will also help part/component manufacturers in diverse fields where shrink-fitting procedures are commonly implemented. Examples include manufacturers of automobiles, aircrafts, turbines, impellers, medical devices, industrial washers, motors, pumps, rocker arm assemblies, large gun barrels used in war ships, gear-shaft assemblies, etc.

## **6.3 Suggestions for Future Research**

From my own experience of conducting research in this dissertation and feedback from the supervisory committee, the following could be state-of-art follow-up research studies.

1. One could study the impact of coil geometry, placement and heat generation rates on the thermal expansion of the girder hole, and hence lead to optimized coil configurations.
2. In many cases, shrink-fit components are required to be disassembled without damage for reuse. Although such problems are inverse of what was studied in this dissertation, the methodology and observations of the current FEM study can be used to direct possible solutions.
3. In AP1, the TH assembly (Step-3) is dipped in the cold medium only after it has reached the room temperature. However, one could put the TH assembly in the cold medium before it reaching the steady state temperature but after it has gained enough interference to be lifted together. This is suggested as the less steep temperature gradients and not fully developed interference stresses at the intermediate stage may result in higher OMCCs.

## REFERENCES

1. Berlin, M.W., *Innovative procedure to install a trunnion-hub assembly in a bascule bridge girder*, 2004 : University of South Florida.
2. Besterfield, G., Kaw, A., Nichani, S., Ratnam, B., Cherukara, T.A. and Denninger, M., *Assembly procedures of trunnion-hub-girder for bascule bridges*. Theoretical and Applied Fracture Mechanics, 2003. **40**(2): p. 123-134.
3. Besterfield, G., Kaw, A.K. and Crane, R., Parametric finite element modeling and full-scale testing of trunnion-hub-girder assemblies for bascule bridges, in Mechanical Engineering, University of South Florida 2001, Florida Department of Transportation (FDOT).
4. Besterfield, G., Nichani, S., Kaw, A.K. and Eason, T., *Full-scale testing of procedures for assembling trunnion-hub-girder in bascule bridges*. Journal of Bridge Engineering, 2003. **8**(4): p. 204-211.
5. Collier, N., Kaw, A., Besterfield, G. and Rahman, M., *Effects of staged cooling in shrink-fitting compounded cylinders*. The Journal of Strain Analysis for Engineering Design, 2006. **41**(5): p. 349-361.
6. Denninger, M.T., Design tools for trunnion-hub-girder assemblies of bascule bridges. 2000: University of South Florida.
7. Kaw, A.K. and Yalcin, A., *Problem-centered approach in a numerical methods course*. Journal of Professional Issues in Engineering Education and Practice, 2008. **134**(4): p. 359-364.
8. Nguyen, C., Kaw, A.K. and Paul, J., *Sensitivity analysis of cooling methods and geometric parameters in the assembly procedure of bascule bridge fulcrum*. The Journal of Strain Analysis for Engineering Design, 2007. **42**(5): p. 337-349.
9. Snyder, L.A., Sensitivity analysis of three assembly procedures for a bascule bridge fulcrum [electronic resource] / by Luke Allen Snyder. 2009: University of South Florida, 2009.
10. Wikipedia. *Bascule bridge*. [ accessed 2012 October 13]; Available from: [http://en.wikipedia.org/wiki/Bascule\\_bridge](http://en.wikipedia.org/wiki/Bascule_bridge).

11. Wikipedia. *Shrink-fitting*. [accessed 2012 December 5]; Available from: <http://en.wikipedia.org/wiki/Shrink-fitting>.
12. Wikipedia. *Induction shrink-fitting*. [accessed 2012 December 4]; Available from: [http://en.wikipedia.org/wiki/Induction\\_shrink\\_fitting](http://en.wikipedia.org/wiki/Induction_shrink_fitting).
13. Ambrell. *Ambrell: An ameritherm company*. [accessed 2012 December 4]; Available from: [http://www.ameritherm.com/apps\\_able.php?utm\\_medium=shrink%20fitting&doc\\_id=shrinkfitting\\_16](http://www.ameritherm.com/apps_able.php?utm_medium=shrink%20fitting&doc_id=shrinkfitting_16).
14. Greenberg, H.D. and Clark, W.G., A fracture mechanics approach to development of realistic acceptance standards for heavy walled steel castings. *Metals Engineering Quarterly*, 1969. **9**(3): p. 30-&.
15. Nied, H.F. and Erdogan, F., *Transient thermal-stress problem for a circumferentially cracked hollow cylinder*. *Journal of Thermal Stresses*, 1983. **6**(1): p. 1-14.
16. Delale, F. and Kolluri, S.P., *Fracture of thick-walled cylinders subjected to transient thermal-stresses*. *Journal of Thermal Stresses*, 1985. **8**(2): p. 235-248.
17. Noda, N. and Sumi, N., Stress intensity factor for transient thermal-stress of a thin plate with a Griffith crack. *Journal of Thermal Stresses*, 1985. **8**(2): p. 173-182.
18. Noda, N., Ashida, F. and Matsunaga, Y., Stress intensity factors for external and penny-shaped cracks in transversely isotropic cylinders subjected to thermal-shock. *Archive of Applied Mechanics*, 1994. **64**(6): p. 383-394.
19. Noda, N. and Matsunaga, Y., Transient thermoelastic problem in an infinite body containing a penny-shaped crack due to time and position dependent temperature condition. *Zeitschrift Fur Angewandte Mathematik Und Mechanik*, 1986. **66**(6): p. 233-239.
20. Noda, N., Matsunaga, Y. and Nyuko, H., Stress intensity factor for transient thermal-stresses in an infinite elastic body with an external crack. *Journal of Thermal Stresses*, 1986. **9**(2): p. 119-131.
21. Noda, N., Matsunaga, Y. and Nyuko, H., Stress intensity factor for transient thermal-stresses in an infinite elastic solid containing an annular crack. *Ingenieur Archiv*, 1988. **58**(1): p. 1-8.
22. Noda, N., Matsunaga, Y. and Nyuko, H., *Coupled thermoelastic problem of an infinite solid containing a penny-shaped crack*. *International Journal of Engineering Science*, 1990. **28**(4): p. 347-353.

23. Noda, N., Matsunaga, Y. and Nyuko, H., *Thermal-shock problem of a hollow circular-cylinder with a crack*. International Journal of Pressure Vessels and Piping, 1990. **42**(2): p. 247-257.
24. Noda, N., Matsunaga, Y., Tsuji, T. and Nyuko, H., *Thermal-shock problems of elastic bodies with a crack*. Journal of Thermal Stresses, 1989. **12**(3): p. 369-383.
25. Oliveira, R. and Wu, X.R., Stress intensity factors for axial cracks in hollow cylinders subjected to thermal-shock. Engineering Fracture Mechanics, 1987. **27**(2): p. 185-197.
26. Araki, W., Adachi, T. and Yamaji, A., Thermal stress analysis of thermoviscoelastic hollow cylinder with temperature-dependent thermal properties. Journal of Thermal Stresses, 2005. **28**(1): p. 29-46.
27. Argeso, H. and Eraslan, A.N., On the use of temperature-dependent physical properties in thermomechanical calculations for solid and hollow cylinders. International Journal of Thermal Sciences, 2008. **47**(2): p. 136-146.
28. Awaji, H. and Sivakumar, R., Temperature and stress distributions in a hollow cylinder of functionally graded material: The case of temperature-independent material properties. Journal of the American Ceramic Society, 2001. **84**(5): p. 1059-1065.
29. Ganguly, B.K., McKinney, K.R. and Hasselman, D.P.H., *Thermal-stress analysis of flat plate with temperature-dependent thermal conductivity*. Journal of the American Ceramic Society, 1975. **58**(9-10): p. 455-456.
30. Goharkhah, M., Amiri, S. and Shokouhmand, H., *Effect of spatial variation of thermal conductivity on non-Fourier heat conduction in a finite slab*. Journal of Mechanical Science and Technology, 2009. **23**(12): p. 3393-3398.
31. Huang, C.H. and Ozisik, M.N., Direct integration approach for simultaneously estimating temperature-dependent thermal-conductivity and heat-capacity. Numerical Heat Transfer Part a-Applications, 1991. **20**(1): p. 95-110.
32. Pardo, E., Sarmiento, G.S., Laura, P. and Gutierrez, R., *Analytical solution for unsteady thermal stresses in an infinite cylinder composed of two materials*. Journal of Thermal Stresses, 1987. **10**(1): p. 29-43.
33. Peery, L. and Todd, F. Linear heat conduction with temperature dependent physical properties in Proceedings of the Oklahoma Academy of Science. 1965. Oklahoma Academy of Science.

34. Stasyuk, S.T., Gromovyk, V.I. and Bichuya, A.L., *Thermal-stress analysis of hollow cylinder with temperature-dependent thermal conductivity*. Strength of Materials, 1979. **11**(1): p. 50-52.
35. Thomas, J.R., Singh, J.P., Tawil, H., Powers, L. and Hasselman, D.P.H., *Thermal-stresses in a long circular-cylinder subjected to sudden cooling during transient convection heating*. Journal of Thermal Stresses, 1985. **8**(2): p. 249-260.
36. Wells, W.R., Re-entry heat conduction of a finite slab with a nonconstant thermal conductivity. AIAA Journal, 1964. **2**(2): p. 379-381.
37. Atefi, G., Abdous, M.A., Ganjehkaviri, A. and Moalemi, N., An analytical solution of a two-dimensional temperature field in a hollow cylinder under a time periodic boundary condition using fourier series. Proceedings of the Institution of Mechanical Engineers Part C-Journal of Mechanical Engineering Science, 2009. **223**(8): p. 1889-1901.
38. Sano, Y., A solution method of inverse heat conduction problem by a integral form of non-steady heat conduction equation for a slab and its application to the calculation of surface temperature-dependent heat transfer coefficient. Kagaku Kogaku Ronbunshu, 2002. **28**(3): p. 330-338.
39. Ehteram, M.A., Sadighi, M. and Tabrizi, H.B., Analytical solution for thermal stresses of laminated hollow cylinders under transient nonuniform thermal loading. Mechanika, 2011(1): p. 30-37.
40. Jabbari, M., Sohrabpour, S. and Eslami, M.R., *Mechanical and thermal stresses in a functionally graded hollow cylinder due to radially symmetric loads*. International Journal of Pressure Vessels and Piping, 2002. **79**(7): p. 493-497.
41. Ootao, Y., Akai, T. and Tanigawa, Y., 3-dimensional transient thermal-stress analysis of a nonhomogeneous hollow circular-cylinder due to a moving heat-source in the axial direction. Journal of Thermal Stresses, 1995. **18**(5): p. 497-512.
42. Radu, V., Paffumi, E., Taylor, N. and Nilsson, K.F., *A study on fatigue crack growth in the high cycle domain assuming sinusoidal thermal loading*. International Journal of Pressure Vessels and Piping, 2009. **86**(12): p. 818-829.
43. Radu, V., Taylor, N. and Paffumi, E., Development of new analytical solutions for elastic thermal stress components in a hollow cylinder under sinusoidal transient thermal loading. International Journal of Pressure Vessels and Piping, 2008. **85**(12): p. 885-893.

44. Sen, S. and Aksakal, B., Stress analysis of interference fitted shaft-hub system under transient heat transfer conditions. *Materials & Design*, 2004. **25**(5): p. 407-417.
45. Conroy, P.J., Derivation of two-dimensional (2-d) conduction equation in generalized coordinates with constant and anisotropic physical properties, 1995, DTIC Document.
46. Darabseh, T., Yilmaz, N. and Bataineh, M., *Transient thermoelasticity analysis of functionally graded thick hollow cylinder based on green-lindsay model*. *International Journal of Mechanics and Materials in Design*, 2012. **8**(3): p. 247-255.
47. Lee, Z.Y., Chen, C.K. and Hung, C.I., *Transient thermal stress analysis of multilayered hollow cylinder*. *Acta Mechanica*, 2001. **151**(1): p. 75-88.
48. Ootao, Y., Transient thermoelastic and piezothermoelastic problems of functionally graded materials. *Journal of Thermal Stresses*, 2009. **32**(6-7): p. 656-697.
49. Shao, Z., Mechanical and thermal stresses of a functionally graded circular hollow cylinder with finite length. *International Journal of Pressure Vessels and Piping*, 2005. **82**(3): p. 155-163.
50. Singh, T. and Gupta, V., Steady-state creep analysis of a functionally graded thick cylinder subjected to internal pressure and thermal gradient. *International Journal of Materials Research*, 2012. **103**(8): p. 1042-1051.
51. Takeuti, Y. and Tanigawa, Y., *Asymmetrical transient thermoelastic problems in a composite hollow circular-cylinder*. *Nuclear Engineering and Design*, 1978. **45**(1): p. 159-172.
52. Tarn, J.Q., Exact solutions for functionally graded anisotropic cylinders subjected to thermal and mechanical loads. *International Journal of Solids and Structures*, 2001. **38**(46): p. 8189-8206.
53. Chen, C.K. and Kuo, B.L., *Coupled transient thermoelastic contact problems for axial cracks in hollow cylinders*. *International Journal for Numerical Methods in Engineering*, 1994. **37**(12): p. 2109-2123.
54. Kovacs, A., Thermal stresses in a shrink fit due to an inhomogeneous temperature distribution. *Acta mechanica*, 1994. **105**(1): p. 173-187.
55. Mack, W. and Bengeri, M., *Thermal assembly of an elastic-plastic shrink fit with solid inclusion*. *International journal of mechanical sciences*, 1994. **36**(8): p. 699-705.

56. Samant, R.N., Phelan, P.E. and Ullah, A.R., *Finite element analysis of residual-stress-induced flatness deviation in banded carbon seals*. Finite Elements in Analysis and Design, 2002. **38**(9): p. 785-801.
57. ANSYS, *Ansys 13*, 2012: ANSYS Inc. Southpointe, 275 Technology Drive, Canonsburg, PA 15317, USA.
58. HeavyMovableStructuresInc. *Assembly and erection of Pamunkey river bascule bridge*. [accessed 2012 10/19/2012]; Available from: [http://www.heavymovablestructures.org/assets/technical\\_papers/Elleven18.pdf](http://www.heavymovablestructures.org/assets/technical_papers/Elleven18.pdf).
59. Montgomery, D.C., *Design and analysis of experiments*. 2008: John Wiley & Sons.
60. Kanninen, M.F. and Popelar, C.H., *Advanced fracture mechanics*. 1985: Oxford University Press, USA.
61. Gross, D. and Seelig, T., *Fracture mechanics: With an introduction to micromechanics*. 2011: Springer.
62. Kaw, A.K., *Mechanics of composite materials*, second edition. 2005: Taylor & Francis.
63. Singer, F.L., *Strength of materials*. 1962: Harper.
64. Ragab, A.R.A. and Bayoumi, S.E.A., *Engineering solid mechanics: Fundamentals and applications*. 1998: Taylor & Francis.
65. AASHTO, *Standard specifications for movable highway bridges*. 1988: American Association of State Highway and Transportation Officials.
66. AASHTO, *Aashto lrfd movable highway bridge design specifications*, 6 th edition. 2012: The Association.
67. Shigley, J.E. and Mischke, C.R., *Standard handbook of machine design*. 1986: McGraw-Hill.
68. Griffin, J.G., *Transient heat conduction in the cylindrical coordinate system by an improved integral technique*. 1962: University of Notre Dame, January.
69. Jiji, L.M., *Heat conduction*. 2003: Begell House.
70. Davis, J.R., *Metals handbook desk edition 2nd edition*. 1998: Taylor & Francis.
71. MATLAB, *Matlab, the language of technical computing*, 2012, <http://www.mathworks.com/products/matlab/>.

72. Chebfun. *Chebfun opensource math numerical solutions group*. 2012; Available from: <http://www2.maths.ox.ac.uk/chebfun/>.
73. Gupta, P.N., *Comprehensive differential equations: Paper ii*. 2005: Laxmi Publications.
74. Bansal, R.K., *A textbook of strength of materials*. 2010: Laxmi Publications Pvt Limited.
75. Richards, K.L., *Design engineer's handbook*. 2012: CRC Press.
76. Ugural, A.C. and Fenster, S.K., *Advanced strength and applied elasticity*. 2003: Prentice Hall PTR.
77. Negi, *Strength of materials*. 2008: McGraw-Hill Education (India) Pvt Limited.
78. ANSYS. *Element reference -ansys*. 2012; Available from: [http://www1.ansys.com/customer/content/documentation/121/ans\\_elem.pdf](http://www1.ansys.com/customer/content/documentation/121/ans_elem.pdf).
79. Computing, R. *Research computing: University of south florida*. 2012; Available from: <http://www.rc.usf.edu/>.
80. ANSYS, *Ansys parametric design language guide*, ANSYS, Editor 2012: ANSYS Inc. Southpointe, 275 Technology Drive, Canonsburg, PA 15317, USA.
81. Minitab, Software: Minitab statistical analysis, 2012, Minitab.
82. Matweb. *Online materials information resource : E glass*. [accessed 2012 October 23]; Available from: <http://www.matweb.com/search/datasheet.aspx?MatGUID=d9c18047c49147a2a7c0b0bb1743e812&ckck=1>.
83. Matweb. *Online materials information resource : GE advanced ceramics hbn hot-pressed boron nitride* [accessed 2012 October 23]; Available from: <http://www.matweb.com/search/DataSheet.aspx?MatGUID=8fbbb7d47809493e9afbb7778657d5bb>.
84. Kreith, F., Manglik, R.M. and Bohn, M.S., *Principles of heat transfer, sixth edition*. 2010: Cengage Learning.
85. EngineeringToolBox. *Properties of air*. [accessed 2012 October 23]; Available from: [http://www.engineeringtoolbox.com/air-properties-d\\_156.html](http://www.engineeringtoolbox.com/air-properties-d_156.html).
86. Varberg, D.E., Purcell, E.J. and Rigdon, S.E., *Calculus*. 2006: Pearson Prentice Hall.

87. Jain, P.K., *A textbook of analytical geometry of three dimensions*. 2005: New Age International (P) Limited.

## APPENDICES

## Appendix A: Hypothesis Testing for Thermal Diffusivity of Steel

Table A.1 Thermal diffusivity as a function of temperature

Temperature, $T$ $^{\circ}F$	Thermal Diffusivity, $\alpha$ $in^2 / sec$
-120	0.0334
-100	0.0334
-80	0.0334
-60	0.0334
-40	0.0334
-20	0.0334
0	0.0334
20	0.0334
40	0.0334
60	0.0334
80	0.0335

For simple regression, let's assume a simple regression equation,

$$\alpha = \beta_1 T + \beta_0$$

The null hypothesis is that thermal diffusivity,  $\alpha$  is independent on  $T$ , and is written as

$$H_0 : \beta_1 = 0$$

The alternate hypothesis is  $\alpha$  is dependent on  $T$ , and is written as

$$H_a : \beta_1 \neq 0$$

We are choosing the value of  $\alpha_{confidence} = 0.05$  (95% confidence).

Using Excel regression test, the following tables are obtained.

**Appendix A (Continued)**

**Table A.2 Regression statistics**

Regression Statistics	
Multiple R	0.500000
R Square	0.250000
Adjusted R Square	0.166667
Standard Error	2.75E-05
Observations	11

**Table A.3 ANOVA Table**

ANOVA					
	df	SS	MS	F	Significance F
Regression	1	2.27E-07	2.27E-07	3	0.117307
Residual	9	6.82E-09	7.58E-10		
Total	10	9.09E-09			

**Table A.4 Intercept and slope value**

	Coefficients	Standard Error	t Stat	P-value	Lower 95%	Upper 95%
Intercept	0.033414	8.7E-06	3838.935	2.81E-29	0.033394	0.033433
X Variable	2.27E-07	1.31E-07	1.732051	0.117307	-7E-08	5.24E-07

As the p-value, 0.117307 is greater than the  $\alpha_{confidence} = 0.05$ , null hypothesis is accepted.

## Appendix B: Convergence Study

Numerical methods approximate the solution by choosing a step or mesh size. Examples include forward divided difference, trapezoidal rule of integration, implicit method of solving an ordinary differential equation, etc. The step or mesh size determines the accuracy of the approximations. The smaller the step or mesh size, the more accurate the approximate solution will be. If the step size or mesh size tends to zero, the solution will asymptotically be the exact solution.

The value of the step size to be chosen for a particular problem is not constant. It changes with the amount of allowable error the user is looking into. How does one determine if the step or mesh size he chose for a particular problem is good enough? The answer to the question is by conducting a convergence study by choosing three different mesh sizes (usually by halving the step size or element edge length each time). The highest density mesh is assumed to be the mesh with infinite number of nodes (step size tends zero). The convergence of a mesh density could be found by using the relation

$$R_N = A + \frac{B}{N^\alpha}$$

**Equation B.1 Convergence equation**

$R_N$  represents the value (solution) for which convergence study is being performed (temperature, stress, displacement),  $A$  represents the theoretical value assuming infinite number of nodes,  $N$  represents the number of nodes or elements,  $B$  and  $\alpha$  are the unknown constants. Three different mesh densities are to be taken (usually by doubling the number of elements/nodes). Then the value of stress or

## Appendix B (Continued)

temperature on which the convergence study is being performed is substituted for  $R_N$ .

The three mesh densities gives three equations and solving the three equations gives the values of  $A, B$  and  $\alpha$ . If  $\alpha$  is greater than 1, the mesh converges quickly.

### B.1 Convergence Study on Analytical Solution

Table B.1, Table B.2, and Table B.3 show temperature and hoop stress values obtained for different mesh densities of analytical solution at three different nodes (radial locations).

**Table B.1 Convergence data at node-1 for analytical solution**

Number of radial divisions $N$	Temperature, $^{\circ}F$	Hoop Stress $\times 10^4 \text{ psi}$
25	-24.5781	-0.592013012
50	-24.5623	-0.593172627
100	-24.5951	-0.593101463
200	-24.5949	-0.593097622
400	-24.5948	-0.593097620
800	-24.5948	-0.593097619
1600	-24.5948	-0.593092619

**Table B.2 Convergence data at node-2 for analytical solution**

Number of radial divisions $N$	Temperature $^{\circ}F$	Hoop Stress $\times 10^4 \text{ psi}$
25	35.7661	0.389213606
50	35.7426	0.388124746
100	35.7226	0.388036606
200	35.7224	0.388023606
400	35.7224	0.388023604
800	35.7224	0.388023603
1600	35.7224	0.388023603

## Appendix B (Continued)

Table B.3 Convergence data at node-3 for analytical solution

Number of radial divisions $N$	Temperature $^{\circ}F$	Hoop Stress $\times 10^4 \text{ psi}$
25	46.8641	0.106068923
50	46.7837	0.105458864
100	46.7634	0.105336721
200	46.7633	0.105348927
400	46.7633	0.105348924
800	46.7633	0.105348923
1600	46.7633	0.105348923

Taking the temperature data from node-1 for 100, 200 and 400 divisions and applying Equation B.1 for the data we have the following equations,

$$-24.5951 = A + \frac{B}{100^{\alpha}}$$

$$-24.5949 = A + \frac{B}{200^{\alpha}}$$

$$-24.5948 = A + \frac{B}{400^{\alpha}}$$

Solving for  $A$ ,  $B$  and  $\alpha$  gives the following values

$$A = -24.59493333$$

$$B = 2.65911863 \times 10^{113}$$

$$\alpha = 5.86836 \times 10^{110}$$

The value of the temperature for 200 divisions for node-1 is -24.5949. The percentage difference of the temperature value obtained for 200 divisions and the value of  $A$  (for infinite nodes) is

## Appendix B (Continued)

$$\begin{aligned} epsa &= \left| \frac{-24.59493333 + 24.5949}{-24.59493333} \right| \times 100 \\ &= 0.0001\% \end{aligned}$$

Taking the hoop stress data from node-1 for 100, 200 and 400 divisions and applying Equation B.1 for the data we have the following equations,

$$-0.593101463 = A + \frac{B}{100^\alpha}$$

$$-0.593097622 = A + \frac{B}{200^\alpha}$$

$$-0.593097620 = A + \frac{B}{400^\alpha}$$

Solving for  $A$ ,  $B$  and  $\alpha$  gives the following values

$$A = -0.59309890166$$

$$B = 2.7229375581 \times 10^{111}$$

$$\alpha = 6.009207022 \times 10^{108}$$

The percentage difference of the temperature value obtained for 200 divisions and the value of  $A$  (for infinite nodes) is

$$\begin{aligned} epsa &= \left| \frac{(-0.5930989016) - (-0.593097622)}{-0.5930989016} \right| \times 100 \\ &= 0.0002\% \end{aligned}$$

Similar observations were made for data at the other nodes.

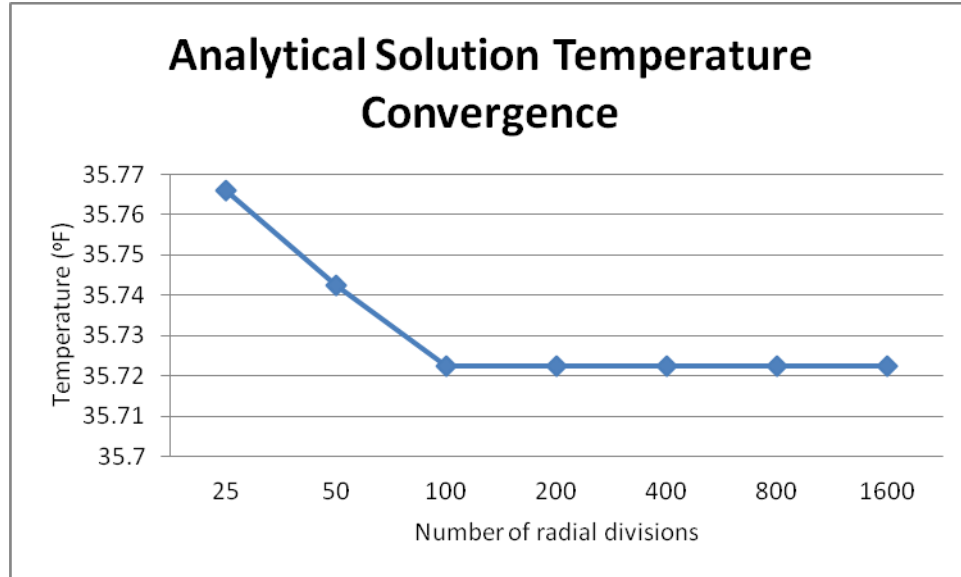


Figure B.1 Convergence of temperature for analytical solution (data from Table B.2)

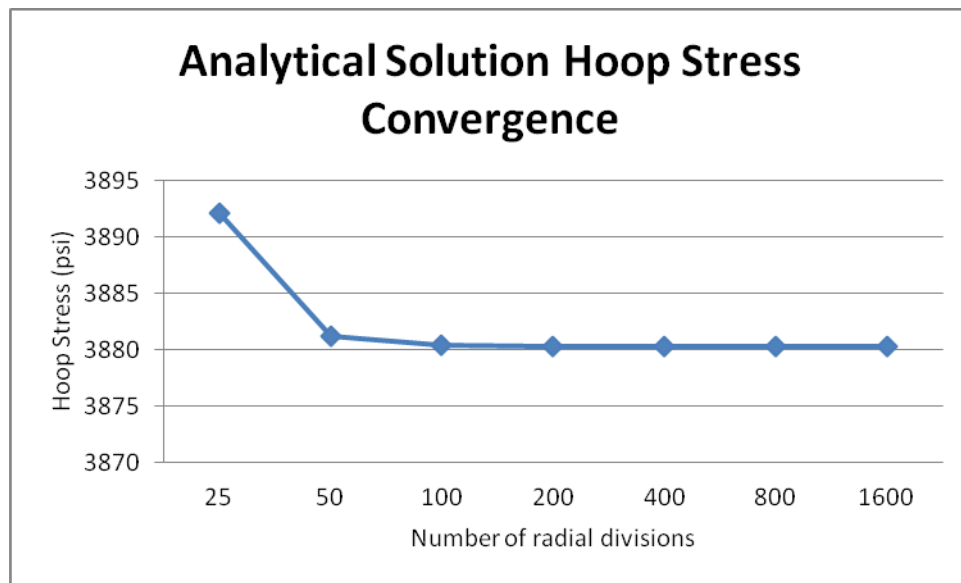


Figure B.2 Hoop stress convergence for analytical solution (data from Table B.2)

## B.2 Convergence Study on Finite Element Model

The Table B.4 shows the temperature and hoop stress data at a radial location in the finite element model.

## Appendix B (Continued)

**Table B.4 Temperature and hoop stress data for finite element model**

Number of nodes $N$	Temperature $^{\circ}F$	Hoop Stress $psi$
50,000	33.6789	3894.24746
99,978	35.6428	3892.36675
199,364	35.8627	3891.14834
399,253	35.8924	3891.12604
794,276	35.8929	3891.12567

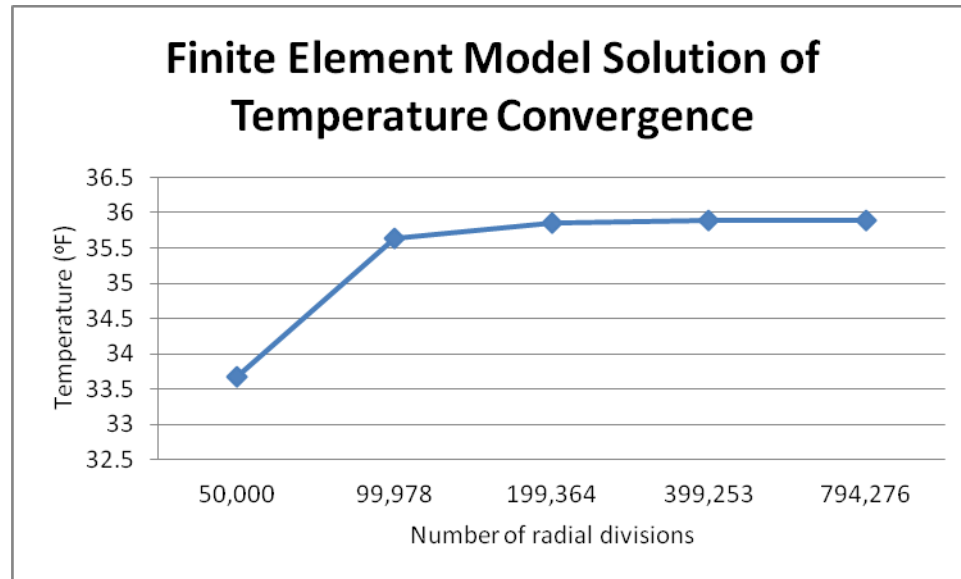


**Figure B.3 Convergence of temperature for finite element solution (data from Table B.4)**

Similar to convergence study of analytical model shown in Appendix B (B.1), using Equation B.1, convergence study is performed on both temperature and hoop stress for 199364, 399253 and 794276 nodes, respectively.

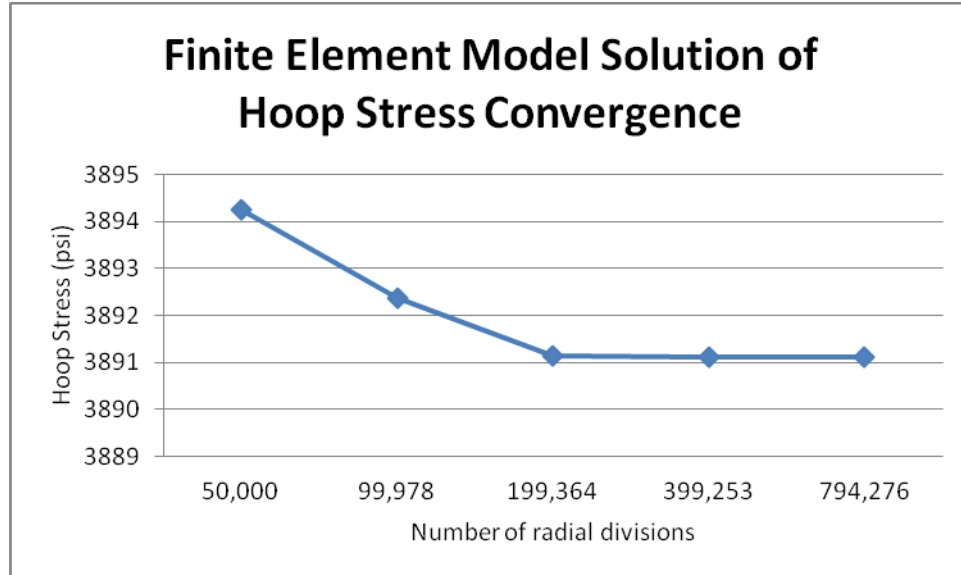


**Figure B.4 Hoop stress convergence for finite element solution (data from Table B.4)**

The values obtained for temperature study are

$$A = 35.88266$$

$$B = 1.0723657 \times 10^{319}$$

$$\alpha = 8.93111 \times 10^{315}$$

Comparing with temperature from mesh density of 399253 nodes,

$$\begin{aligned} epsa &= \left| \frac{35.88266 - 35.8924}{35.88266} \right| \times 100 \\ &= 0.027\% \end{aligned}$$

The values obtained for hoop stress convergence study are

$$A = 3891.13335$$

$$B = -6.97757665 \times 10^{30}$$

$$\alpha = 3.5078641463 \times 10^{27}$$

Comparing with temperature from mesh density of 399253 nodes,

$$\begin{aligned} epsa &= \left| \frac{3891.1335 - 3891.12604}{3891.1335} \right| \times 100 \\ &= 0.00018\% \end{aligned}$$

A mesh density with 399,253 nodes is chosen for this study.

## Appendix C: Radial Interference Calculations

The interference fits have a certain upper and lower limit. The limit  $L$  in thousands of an inch is given by

$$L = CD^{\frac{1}{3}}$$

Equation C.1 Interference limit formula [67]

$C$  is the coefficient based on fit and  $D$  is the nominal diameter.

### C.1 Interference Calculations for TH

For FN3 fit between the TH assemblies, the following  $C$  values are taken.

Table C.1 TH coefficient value  $C$  for FN3 [67] fit

	Trunnion	Hub
Low	3.739	0
High	4.31	0.907

Table C.2 TH interference calculations for all the three bridges in this study

	17th St.		Christa McAuliffe		Hallandale	
	Inner	Outer	Inner	Outer	Inner	Outer
Trunnion	1.19	12.944 <sup>+0.0101196</sup> <sub>+0.008778</sub>	1	18 <sup>+0.01129539</sup> <sub>+0.00979895</sub>	1.5	26 <sup>+0.012768358</sup> <sub>+0.011076773</sub>
Hub	12.944 <sup>+0.00212959</sup> <sub>+0.00000000</sub>	15.5328	18 <sup>+0.002377012</sup> <sub>+0.000000000</sub>	21.6	26 <sup>+0.002686984</sup> <sub>+0.000000000</sub>	31.2
Radial	0.003324702		0.00371097		0.004194894	
Interference	0.00505984		0.005647698		0.006384179	

### C.2 Interference Calculations for HG

For FN3 fit between the TH assemblies, the following  $C$  values are taken.

Table C.3 HG coefficient value  $C$  for FN3 [67] fit

	Hub	Girder
Low	3.739	0
High	4.31	0.907

**Appendix C (Continued)**

**Table C.4 Table HG interference calculations for all the three bridges in this study**

Diameter	17th St.		Christa McAuliffe		Hallandale	
	Inner	Outer	Inner	Outer	Inner	Outer
Hub	12.944	15.5328 <sup>+0.01075376</sup> <sub>+0.00932907</sub>	18	21.6 <sup>+0.012003149</sup> <sub>+0.010412940</sub>	26	31.2 <sup>+0.01356840</sup> <sub>+0.01177082</sub>
Girder	15.5328 <sup>+0.00226</sup> <sub>+0.00000</sub>	NA	21.6 <sup>+0.002525953</sup> <sub>+0.000000000</sub>	INA	31.2 <sup>+0.00285534</sup> <sub>+0.000000000</sub>	NA
Radial Interference	0.003533023		0.003943494		0.004457741	
	0.005376882		0.006001574		0.006784203	